SANDIA REPORT
SAND2008-6316

Creating a Discovery Platform for Confined-Space Chemistry and Materials:

Metal-Organic Frameworks

Final LDRD Project Report

Mark D. Allendorf, Principal Investigator

Microfluidics Department

Jeffery A. Greathouse

Geochemistry Department

Blake A. Simmons

Energy Systems Department

Prepared by
Sandia National Laboratories
Albuquerque, New Mexico 87185 and Livermore, California 94550

Sandia is a multiprogram laboratory operated by Sandia Corporation,
a Lockheed Martin Company, for the United States Department of Energy's
National Nuclear Security Administration under Contract DE-AC04-94AL85000.

Issued by Sandia National Laboratories, operated for the United States Department of Energy by Sandia Corporation.

Printed in the United States of America. This report has been reproduced directly from the best available copy.

Available to DOE and DOE contractors from
U.S. Department of Energy
Office of Scientific and Technical Information
P.O. Box 62
Oak Ridge, TN 37831

Telephone: (865) 576-8401
Facsimile: (865) 576-5728
E-Mail: reports@adonis.osti.gov
Online ordering: http://www.osti.gov/bridge

Available to the public from
U.S. Department of Commerce
National Technical Information Service
5285 Port Royal Rd.
Springfield, VA 22161

Telephone: (800) 553-6847
Facsimile: (703) 605-6900
E-Mail: orders@ntis.fedworld.gov
Online order: http://www.ntis.gov/help/ordermethods.asp?loc=7-4-0#online

Creating a Discovery Platform for Confined-Space Chemistry and Materials:
Metal Organic Frameworks

Final LDRD Project Report

Mark D. Allendorf, Principal Investigator
Microfluidics Department

Jeffery A. Greathouse
Geochemistry Department

Blake A. Simmons
Energy Systems Department

ABSTRACT

Metal organic frameworks (MOF) are a recently discovered class of nanoporous, defect-free crystalline materials that enable rational design and exploration of porous materials at the molecular level. MOFs have tunable monolithic pore sizes and cavity environments due to their crystalline nature, yielding properties exceeding those of most other porous materials. These include: the lowest known density (91% free space); highest surface area; tunable photoluminescence; selective molecular adsorption; and methane sorption rivaling gas cylinders. These properties are achieved by coupling inorganic metal complexes such as ZnO4 with tunable organic ligands that serve as struts, allowing facile manipulation of pore size and surface area through reactant selection. MOFs thus provide a discovery platform for generating both new understanding of chemistry in confined spaces and novel sensors and devices based on their unique properties.

At the outset of this project in FY06, virtually nothing was known about how to couple MOFs to substrates and the science of MOF properties and how to tune them was in its infancy. An integrated approach was needed to establish the required knowledge base for nanoscale design and develop methodologies integrate MOFs with other materials.

This report summarizes the key accomplishments of this project, which include creation of a new class of radiation detection materials based on MOFs, luminescent MOFs for chemical detection, use of MOFs as templates to create nanoparticles of hydrogen storage materials, MOF coatings for stress-based chemical detection using microcantilevers, and “flexible” force fields that account for structural changes in MOFs that occur upon molecular adsorption/desorption. Eight journal articles, twenty presentations at scientific conferences, and two patent applications resulted from the work. The project created a basis for continuing development of MOFs for many Sandia applications and succeeded in securing $2.75 M in funding from outside agencies to continue the research.

Contents

Introduction

Chemistry in confined environments such as pores, protein active sites, and at interfaces is a critical aspect of many technical problems of importance to Sandia, including water purity, transport of materials through rock formations, chemical and biological separations, membranes for fuel cells, and gas storage. Nanoporous materials also hold great promise for the development of next-generation electro-optical-chemical sensors and other devices with exceptional capabilities. Probing porous environments and controlling their properties represents a major challenge, since tailoring the geometrical and chemical environment of a pore in a controlled manner is very difficult.

Metal organic frameworks (MOF), a recently discovered class of nanoporous, defect-free crystalline materials, offer a solution to these problems. MOFs have tunable, monolithic pore sizes and cavity properties due to their structure and crystalline nature, enabling rational synthetic design of porous materials at the molecular level. MOFs have properties exceeding those of most other porous materials, including the lowest known density, highest surface area, tunable photoluminescence, highly selective molecular adsorption, and methane sorption rivaling gas cylinders. These unusual properties are achieved by coupling inorganic metal complexes such as ZnO_4 with tunable organic ligands that serve as struts, allowing facile manipulation of pore size and surface area through reactant selection (for example, see Fig. 1.1). However, virtually nothing is known about the factors controlling pore chemistry or how to use MOFs to create useful devices. The objectives of this project were thus to 1) establish MOFs as a discovery platform for exploring and understanding confined-space chemistry and 2) to enable the exploitation of their unique properties by creating for the first time MOF thin films on a range of useful substrates. These goals are synergistic: understanding the pore chemistry is the foundation for rational device design, while coupling MOFs with other materials facilitates and expands their use as an experimental tool for understanding confined-space phenomena.

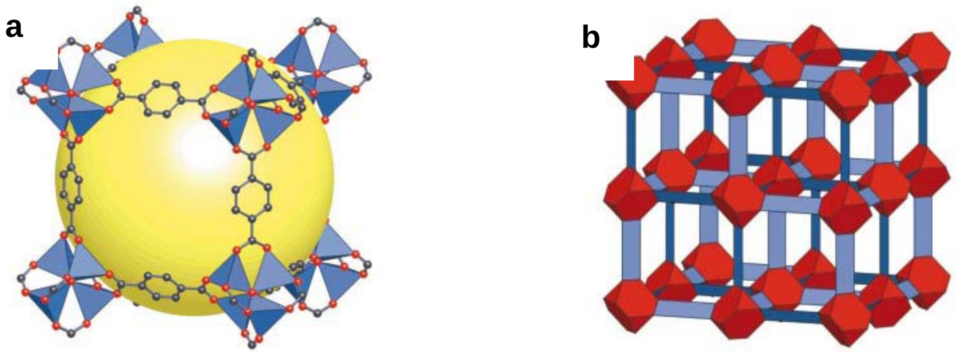

Fig. 1.1 The MOF-5 structure and its topology. a), The MOF-5 structure shown as ZnO_4 tetrahedra (blue polyhedra) joined by benzene dicarboxylate linkers (O, red and C, black) to give an extended 3D cubic framework with interconnected pores of 8 Å aperture width and 12 Å pore (yellow sphere) diameter. (Yellow sphere represents the largest sphere that can occupy the pores without coming within the van der Waals size of the framework). b) The structure shown as the envelopes of the $(OZn_4)O_{12}$ cluster (red truncated tetrahedron) and benzene dicarboxylate (BDC) ion (blue slat). (adapted from Yaghi et al. *Nature* **423** (2003), 705).

Technical Approach

To achieve the two objectives listed above we applied and expanded Sandia's expertise in interfacial chemistry, multiscale modeling, and material systems integration. The project comprised three tasks described in detail below. In Task 1 we synthesized MOFs with tunable pore size and chemistry, thoroughly characterize their properties, and identified suites of MOFs to address key SNL missions. In Task 2, validated and robust models were developed that reveal the links between pore electronic structure and macroscopic observables such as molecular adsorption. In Task 3 we developed methods to create MOF films on a range of materials, a key advance that enables these materials to be incorporated into device structures.

To accelerate this effort, we formed several important collaborations:

- Prof. Roland Fischer (Institute of Inorganic Chemistry, Ruhr Universität Bochum, Germany); expertise in the synthesis of MOF compounds.
- Prof. Tatiana Timofeva (New Mexico Highlands University); single-crystal x-ray crystallography
- Prof. David Bahr (Materials Science and Engineering, Washington State University); nanoindentation and mechanical properties of materials.
- Prof. Jeffery Long (Dept. of Chemistry, University of California, Berkeley); synthetic inorganic chemistry; provided access to the Advanced Light Source at Lawrence Berkeley National Laboratory to perform x-ray diffraction measurements on very small crystals.
- Dr. Jeffery Grossman (Berkeley Nanoscience and Nanotechnology Institute, University of California, Berkeley); computational nanoscience

In **Task 1** we synthesized a variety of MOF materials and characterized their properties. This work generated data for validating models of confined-space phenomena developed in Task 2 and established a general capability for synthesizing MOFs with potential for particular applications. We synthesized specific crystalline MOFs already known to possess useful properties, including two new zinc oxide MOFs having unique luminescent properties (see Sect. 2, a – c) that can be used as scintillators to detect ionizing radiation (Sect.. 3) Composition and crystalline phase, specific surface area, gas sorption isotherms, and spectroscopy properties were determined. Mechanical properties were determined for the first time using nanoindentation (Sect. 4). These results, combined with guidance from the theory/modeling task, allowed us to identify suites of MOFs for development to address key SNL missions. Finally, we made use of the nanoporosity of MOFs to create hybrid materials by infiltrating with either luminous lanthoid ions (Sect. 2d) or metal precursors to create nanoclusters of metal hydrides for hydrogen storage (Sect.. 7).

In **Task 2** developed predictive tools, validated by experimental data from Task 1 and the literature, which simulate the electronic environment within a MOF pore. This work provides the essential link between nanoscale structure and macroscopic properties that will enable MOFs to be used as a discovery platform for probing confined-space chemistry. Although a large number of MOF compounds have been synthesized, it is by no means clear what structural or chemical features lead to unique properties such as high gas sorption, molecular selectivity, etc. Identifying these will vastly simplify synthetic efforts to develop new MOFs with tailored properties and create the theoretical underpinning needed to test theories of such important confined-space phenomena as gas sorption, molecular transport, and separations. Our approach was comprised of two components: 1) ab initio calculations on MOFs or molecular analogs to determine molecular structure, atomic charges, and short-range (van der Waals) interactions, and 2) large-scale force-field (FF) and molecular dynamics (MD) calculations to predict macroscopic phenomena such as adsorption isotherms so that models can be tested and validated. In Year 1 we will used ab initio electronic structure codes to calculate structures and atomic charges on representative MOFs and used these to establish force fields required for large-scale atomistic simulations. Predicted structures, vibrational data, and gas sorption data were compared with experimental measurements 1 to validate method/basis set selection. The results of this work are discussed in Sect.. 5.

The **Task 3** objective was to create MOF thin films on a variety of substrates, thus bringing them out of the lab flask and into the world of applications. At the outset of this project, MOFs were available only as crystals, inhibiting their use in electronic devices and sensors. Coupling them to other materials enables both device fabrication and provides a robust platform for conducting experiments to probe the effects of pore size/electronic structure on confined-space phenomena. Metals, semiconductors, optical materials, plastics, and ceramics are all attractive. To do this, however, requires an ability to nucleate MOF growth on these materials. The results of this work are discussed in Sect. 6

Key products of this research

By any standard this LDRD project has been extraordinarily successful. Many results were obtained that could not have been envisioned at the outset of the project, consistent with the “discover” nature of the work. The body of new science developed here provides the basis for expanded work on MOFs in areas of key importance to Sandia. Some of this work has already been funded by outside agencies. The key concepts that were spawned as a result of this research include:

- Scintillating MOFs, the first new class of radiation detection materials since the advent of plastic scintillators in 1950
- Doped MOFs for that enable detection of organic compounds via luminescence
- MOF templates that enable synthesis of nanoparticle hydrogen storage materials of defined size and composition
- MOF coatings that enable stress-based chemical detection
- “Flexible” force fields that account for structural flexibility in MOFs that is key to many of their unique properties

From a quantitative point of view, the project produced the following:

- Nine articles published, accepted, or submitted to peer-reviewed journals
- Twenty-two presentations at international conferences or universities (3 invited)
    - Two patent applications: “A hybrid metal organic scintillator materials system and particle detector,” filed May 4, 2007

    - “Chemical detection using lanthanoid-infiltrated metal organic frameworks,” provisional application filed August 2008.
- New project funded by the Defense Threat Reduction Agency (DTRA): “Structural Origins of Scintillation: Metal Organic Frameworks as a Nanolaboratory,” $250 K/year for three years
- New project funded by Dept. of Energy Office of Hydrogen, Fuel Cells, and Infrastructure Technologies: “Tunable Thermodynamics and Kinetics for Hydrogen Storage: Nanoparticle Synthesis using Ordered Polymer Templates,” ($650 K/year for three years).

The remainder of this report describes in detail many of the most important results. Sections 2a, 2b, 3, 4, and 5 are taken from published or submitted journal articles. The remaining sections summarize work that as of the date of this report is at a preliminary stage, with follow-on funding expected.

2. Fluorescent Metal-organic Frameworks

2a. Influence of Connectivity and Porosity on Ligand-Based Luminescence in Zinc Metal-Organic Frameworks[1]

Introduction

Understanding and predicting the photophysical properties of chromophores in the solid state is important for an increasing number of organic materials applications, where control over the spatial interactions of chromophores represents a significant challenge.[1-3] The geometry of a molecular assembly is often difficult to predict due to the large number of intermolecular forces that can influence the packing of molecules in a crystal. Metal-organic frameworks (MOFs) are a class of crystalline coordination polymers with the potential to control these interactions through appropriate choice of the constituent metal and ligand units. MOFs consist of metal ions or clusters connected by organic linker groups, which can lead to structural rigidity, high porosity, and well-defined architectures.[4-6] These properties are desirable for a variety of applications, and the use of MOFs for gas storage,[7,8] drug delivery,[9] separations,[10-12] and catalysis[13,14] is currently being explored. The structural stability of MOFs results from strong metal-ligand coordination, which can afford some degree of predictability to the framework geometry and leads towards rational methods of crystal engineering. This has been utilized as a strategy to engineer non-centrosymmetric crystals for nonlinear optics (NLO) applications[15] and asymmetric catalysis,[14] for example. This led us to postulate that MOFs could offer predictable, well-defined environments for chromophores in solid-state materials.

Despite the large number of MOF materials described in the literature, however, reports of luminescent MOFs are scarce, especially those that display ligand-based emission.[5,16,17] The majority of materials in this class exhibit metal ion-centered luminescence due to the incorporation of lanthanide elements into their framework.[18-20] One potential advantage for the use of ligand-based emission in MOFs is that it should readily be tunable through variation of the nature of the linker and/or the structure of the framework. Additionally, calculations regarding the electronic structure of prototypical porous 3-D MOFs have suggested that the bandgaps of these materials can be altered by changing the degree of conjugation in the ligand.[21] Such factors may prove important for the practical application of these materials.

In this paper, we describe a ligand-based approach to the synthesis of new luminescent MOF compounds. Zinc-based MOF motifs are used to prepare two new extended structures that differ in dimensionality, but feature rigid metal-ligand coordination geometries that provide support for a luminescent linker with an inherent degree of flexibility, *trans*-4,4'-stilbene dicarboxylic acid (LH_2; linker unit L). Stilbene has a range of technologically-important uses. For example, it is an important component in solid-state scintillating materials, as its luminescence can be used to discriminate neutron and gamma-ray radiation.[22] Additionally, stilbenes are commonly employed as a backbone motif in organic NLO materials,[23-25] and may be considered the fundamental unit of the electro- and photoluminescent conjugated polymer, poly(*para*-phenylenevinylene) (PPV).[26-28]

---

[1] This section is taken from C. Bauer, T. Settersten, B. Patterson, T. Timofeeva, V. Liu, B. Simmons, M. D. Allendorf "Influence of connectivity and porosity on ligand-based luminescense in zinc MOFs," *J. Amer. Chem. Soc.* 129 (2007), 7136.

Our interest in stilbene-based MOFs is two-fold: first, stilbenes can undergo a light-induced *trans-cis* isomerization, a nonradiative decay pathway that significantly decreases the photoluminescence quantum yield (QY).[29] However, the QY can theoretically approach 100% when this mechanism is suppressed. Various efforts have been made to rigidify stilbenes, such as increasing media viscosity,[30] incorporation into zeolite pores,[31] binding to antibodies,[32] or synthetically locking the ethylene unit into the *trans* configuration by ring closure.[33,34] Incorporation of stilbene as the linker into a MOF lattice could potentially suppress this isomerization by fixing the ligand configuration through rigid coordination, affording a material with increased QY and brightness. Second, the low density and regularity of MOFs allows for well-defined interactions between linkers within the framework and with their environment, which may be investigated spectroscopically by suitable choice of ligand chromophore. Stilbene excimer luminescence has been used for sensitive detection of DNA[35] and antibody binding events.[32] We are, therefore, interested in probing structural- and guest-dependent luminescence of stilbene-based MOF materials as model systems and for their potential sensing capabilities.

It is well-established that different crystal structures can result from the same starting materials under different synthetic conditions.[36,37] For example, the use of $Zn(NO_3)_2$•xH_2O and 1,4-benzene dicarboxylic acid can yield a variety of MOF structures by varying reaction conditions. These can differ in connectivity and porosity depending on the nature of the secondary building unit (SBU), often forming networks with di- and trinuclear cluster SBUs, and 3-D cubic frameworks with tetranuclear SBUs.[37] With this in mind, we sought to form two different zinc-stilbene MOFs, allowing for the study of their luminescence in both 2-D and 3-D extended structures. We report here the synthesis, structure, and luminescent properties of these MOFs, along with their optical response to the exchange of solvent guest molecules. These results show that coordination to the metal clusters in the frameworks imposes structural rigidity on the stilbene moieties, leading to longer luminescence lifetimes and presumably increased QY; this is similar for both structures although a variation in porosity and inter-chromophore coupling is observed between the 2-D and 3-D structures. In addition, reversible, guest-dependent luminescence suggests that our approach may allow for the design of high-efficiency chromophore assemblies with optical properties suitable for sensing applications.

Results and Discussion

Structure and Characterization. Yellow, needle-like crystals resulted from solvothermal reaction of $Zn(NO_3)_2 \cdot 6H_2O$ and LH_2 in *N,N*-dimethylformamide (DMF) at 70 ºC for 16 hrs, then 85 ºC for 4 hrs. Their formula and structure were determined *via* single-crystal X-ray diffraction and elemental analysis to be $Zn_3L_3(DMF)_2$, **1**; these were obtained phase-pure, as indicated by powder X-ray diffraction (PXRD). **1** is two-periodic, consisting of hexagonal networks composed of trinuclear $Zn_3(RCO_2)_6$ SBUs connected by the organic *trans*-4,4'-stilbene links (Figure 1.1a). Figure 1.1b shows that the SBU contains a linear array of three zinc atoms lying on a 3-fold axis; the central zinc atom rests on a crystallographic inversion center. The overall symmetry of the SBU is S_6, so that the carboxylate groups bridge the zinc atoms in a non-planar *syn*-skew fashion (*cis*-O-Zn-O angles deviate only slightly from 90^o), allowing the stilbene linker to remain planar (torsion angles between phenyl rings <2°). The central zinc atom has octahedral coordination, while the terminal zincs are tetrahedral; their apical sites are occupied by O atoms of DMF molecules, which themselves exhibit disorder over three possible orientations. The terminal monodentate DMF ligands are disordered relative to the 3-fold axis. The Zn-O bonds of the central hexa-coordinated zinc atom are evidently longer than those of the tetra-coordinated zinc atoms; moreover, the Zn-O(DMF) bond length lies between the Zn-O bond lengths for tetra- and hexa-coordinated zinc atoms. The Zn**…**Zn separation of 3.515 Å does not indicate any significant direct interaction between the metal atoms; this distance is constrained by the bridging geometry.

The SBUs are connected by linker units in a hexagonal pinwheel geometry, affording a 2-D, layered arrangement (Figure 2.1c and 2.1d) with disordered DMF filling space above and below the layer units (Figure 1e). Individual layers stack together with a cubic *ABCABC* motif, resulting in a dense structure ($d = 1.52$ g/cm^3), without significant overall porosity (*i.e.* triangular pores visible in Figure 1d are, in fact, partially occupied by the packing of additional layers). **1** is isostructural with a recently reported Co-stilbene MOF, also prepared in DMF.[38]

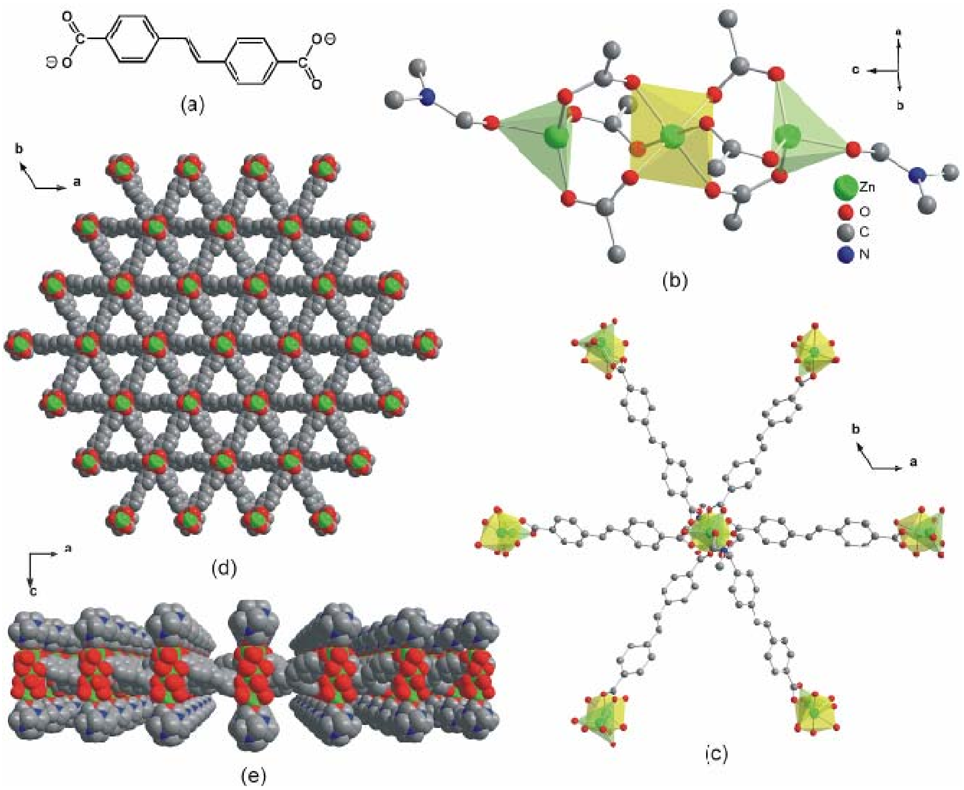

Figure 2.1. (a) *trans*-4,4'-Stilbene dicarboxylate linker, L. (b) View of X-ray crystal structure of **1** parallel to the *c*-axis, showing $Zn_3(RCO_2)_6(DMF)_2$ SBU along with C(4) atoms of stilbene rings. Only one orientation of disordered DMF is shown; O_h Zn coordination polyhedron is yellow, T_d polyhedra are green. (c) View of **1** looking down onto this SBU, showing the hexagonal pinwheel connections between adjacent SBUs made by the linker units. (d) Space-filling model of **1** looking down *c*, showing the 2-D network formed. (e) Space-filling model of a single layer of **1** looking down *b*, showing terminal T_d Zn atoms capped by disordered DMF molecules above and below the layer, with the Zn-L network extending in the *ab*-plane.

Variation of the solvothermal synthesis of **1** substituting *N,N*-diethylformamide (DEF) as the solvent at 105 °C for 16 hrs afforded colorless, prism-like crystals. Single-crystal XRD reveals these to have a porous 3-D framework structure, **2**, consisting of two interpenetrated networks with formula unit Zn_4OL_3 which exhibit a distorted primitive cubic topology with elementary cage size $a \approx b \approx c \approx 19.4$ Å and $\alpha \approx \beta \approx 90$, $\gamma \approx 77$ ^{o} (Figure 2.2). Growth of these crystals requires temperatures above 100 °C to yield phase-pure materials, otherwise traces of other unidentified phases (possibly including **1**) are observed in the PXRD patterns. However, **2** was never observed by PXRD as a by-product of the **1** syntheses described above.

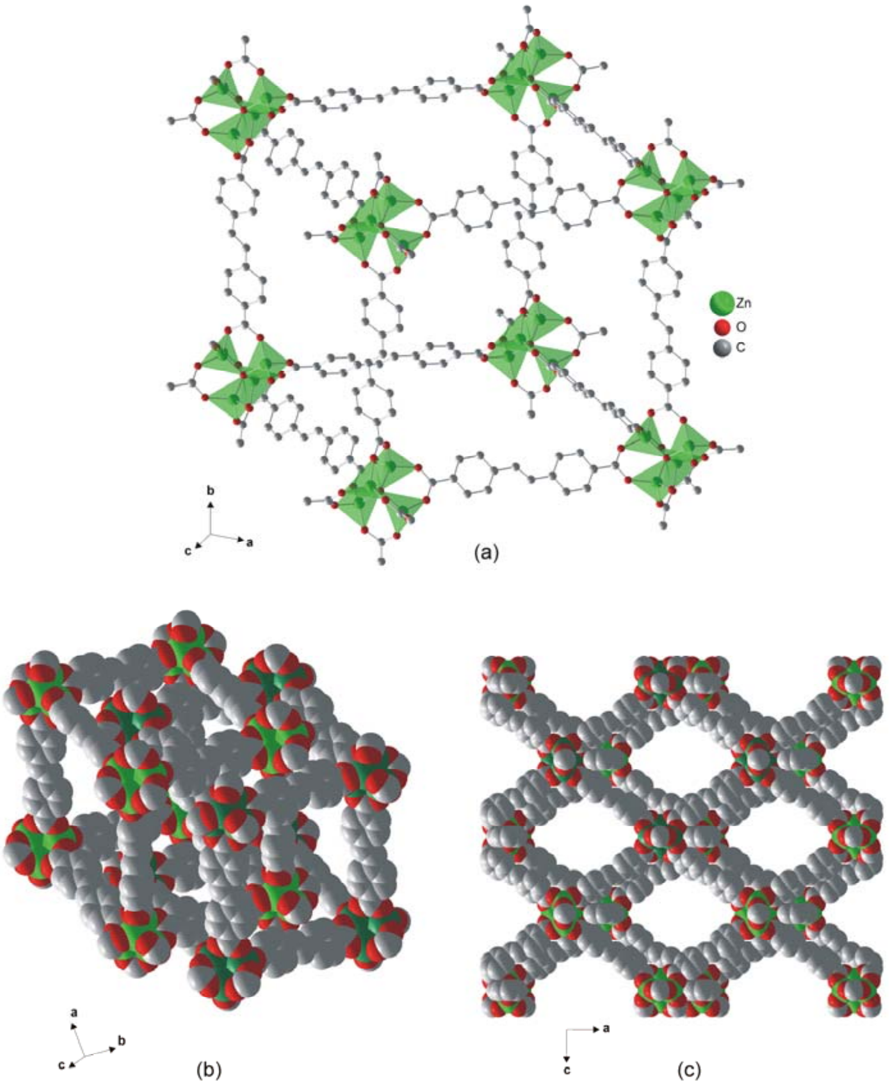

Figure 2.2. X-ray crystal structure of **2**, showing cubic framework of $Zn_4O(RCO_2)_6$ SBUs connected by *trans*-stilbene linkers and green T_d Zn coordination polyhedra (a), and (b) a space-filling model showing interpenetrated, porous lattice of two distinct cubic nets (light and dark green Zn atoms respectively). The pores extend through the crystal, as shown for the [010] projection in (c).

Each of the frameworks in the structure of **2** is constructed from basic zinc carboxylate units $Zn_4O(RCO_2)_6$ as the SBUs which are bridged by the organic *trans*-4,4'-stilbene links. Figure 2a shows this SBU is a cluster with tetrahedral local coordination about each zinc atom; the carboxylate C atoms of each cluster serve as points-of-extension that define the vertices of an octahedron. The stilbene units are essentially planar, if slightly more distorted than in **1** (torsion angles between phenyl rings <5°). Although the positions of the framework atoms were determined accurately, the free guest chloroform and DMF molecules filling the pores were not located due to the highly porous nature of **2** and the disorder problems usually encountered in this type of structure. Despite being interpenetrated, the structure of **2** contains large cavities; in particular, there are 17.1 × 17.1 Å channels in the [010] projection, as shown in Figure 2.2c.

Moreover, in the overall crystal structure of **2,** there exist no specific interactions between the two interpenetrated frameworks, so the maximum internal pore size can be represented as a sphere with diameter 16.5 Å, where the diameter of this sphere is equal to the distance of separation between the van der Waals surfaces of the frameworks.

This framework structure is analogous to the so-called IRMOF series, all of which are three-periodic, cubic-type structures with $Zn_4O(RCO_2)_6$ SBUs. Interestingly, the synthesis of **2** required conditions similar to those reported by Yaghi and co-workers to favor construction of this particular SBU, a compelling illustration that chemical control may be used to give materials with tunable properties, but similar topologies.[7,39]

Crystals of **1** are air-stable and maintain their structure after evacuation at 100 °C, as determined by PXRD (see Supporting Information) and elemental analysis. Thermogravimetric analysis (TGA) indicates loss of 2 equivalents of DMF (13 wt%) above 250 ºC, followed by full decomposition at higher temperature, as shown in Figure 2.3. Unfortunately, attempted removal of coordinated DMF from crystals of **1** by evacuation at 250 °C in an effort to generate a structure with unsaturated zinc centers gave substantial decomposition.

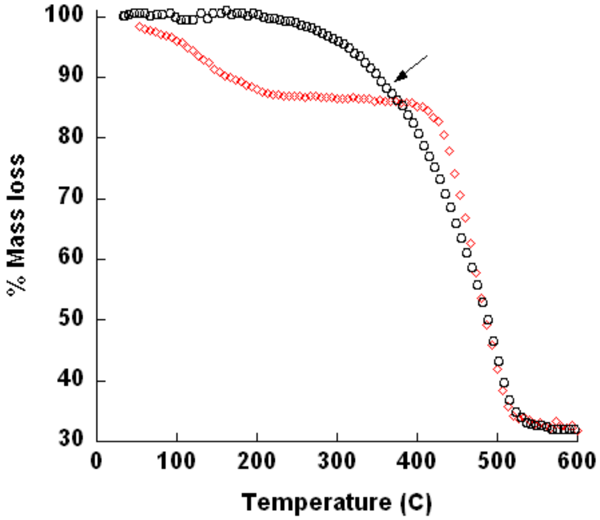

Figure 2.3. Thermogravimetric analysis (TGA) data for **1** (red circles) and **2** (blue diamonds). For the 2-D MOFs (**1**), mass loss of strongly coordinated DMF occurs (13%, see arrow), followed by steady decomposition which continues until 520 °C. For the 3-D MOFs (**2**), initial mass loss from solvent incorporated into the pores is evident until approximately 200 °C (15%, approximately 1 eq. DMF and 1 eq. $CHCl_3$), followed by a plateau after which a relatively sharp decomposition occurs at 400 °C.

Crystals of **2** contain incorporated guest solvent molecules that can be exchanged, although extended evacuation results in an irreversible structural change and significant loss of crystallinity (determined by PXRD, see Supporting Information). Similar behavior has been found previously for a zinc MOF with a comparable, interpenetrated structure (IRMOF-9, linker = 4,4'-biphenyl dicarboxylate); this has been attributed to a weakening of the interactions between interpenetrated units when the ligand is relatively long and flexible, and the misalignment of these units upon solvent removal.[7] Luminescence studies for **2** (see below) suggest that, in the solvated structure, no significant interaction occurs between the stilbene units of the interpenetrated frameworks and, thus, the lack of substantial cohesive forces between these units results in a similar structural collapse after evacuation. Although interpenetration decreases the pore size compared to a fully-open structure, the calculated solvent accessible portion accounts for 76.2% of the crystal volume, with a pore diameter of 16.5 Å and density 0.50 g/cm^3 (respective values for IRMOF-9 are 74.7%, 14.5 Å and 0.66 g/cm^3).[39] TGA data shown in Figure 2.3 reveal that, after mass loss from incorporated solvent in the pores (~15 wt%), **2** is thermally stable up to 410 ºC before the onset of further mass loss.

Crystals of **1** display no significant surface area through gas sorption measurements, as expected due to their high density and the pore occlusion evident in their crystal structure. In contrast, surface area measurements for **2** exhibit a Type I sorption isotherm (indicative of homogeneous micropores) with a Langmuir surface area of 580 m^2/g. This value is lower than typical for comparable MOF structures (commonly 1000-4300 m^2/g)[7,39] presumably due to the structural change upon evacuation resulting in a partial collapse of the framework; however, this indicates that the evacuated structure still retains some porosity. The adsorption/desorption profile displays significant hysteresis (see Figure 2.4), indicating that there may also be a structural alteration during measurement, possibly due to a change in interaction between the catenated units and/or the linker exhibiting flexibility (e.g. about the double bond) under these conditions. Recently, MOFs containing a similar linker (*trans*-4,4'-bis(4-pyridyl)ethene) have been shown to display anomalous sorption behavior due to dynamic shape changes, which can also be induced by variation of incorporated guest molecules.[40] Dynamic structural changes in the framework may be desirable for advanced applications, such as combined sensing and separation. For example, MOFs with similar interpenetrated structures have been reported to undergo structural changes that allow for size- and shape-matching of guests and their use in GC separations of alkanes.[12]

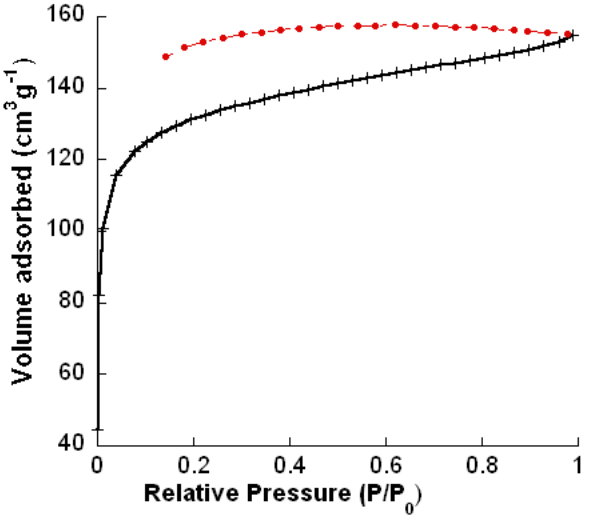

Figure 2.4. Nitrogen sorption isotherm for **2** measured at 77 K. Adsorption is shown in black hatches, desorption in red circles. Langmuir surface area is estimated to be 580 ± 6 m^2/g.

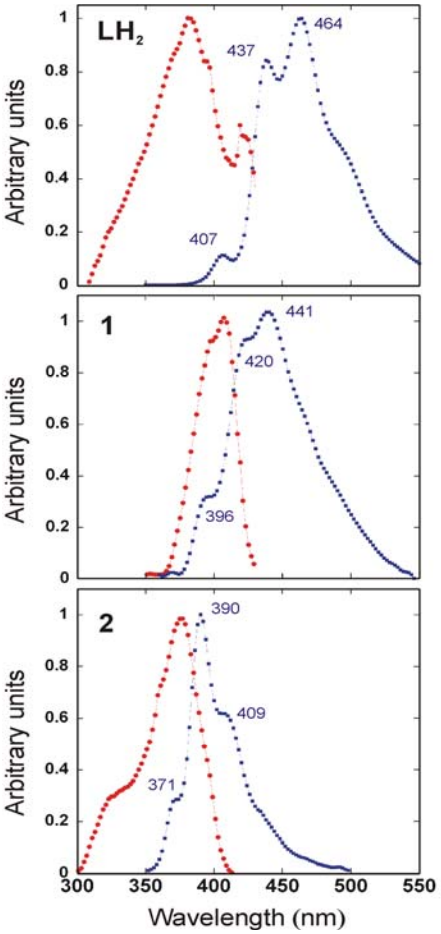

Figure 2.5. Normalized excitation (red circles) and emission (blue squares) spectra for LH_2 (as a powder sample, top), **1** (middle), and **2** (bottom). Spectra of **1** and **2** were obtained for individual crystals soaked in $CHCl_3$. λ_{ex} = 350 nm for LH_2 and **1**, 325 nm for **2**. Emission maxima for the first three vibronic bands are indicated. Excitation spectra were detected at 450 nm.

Photoluminescence studies

Crystals of **1** and **2** contain the same linker in two different, well-defined geometries, allowing for a comparative study of their photoluminescence and its interpretation with regard to the local linker environment within each structure. Both appear very bright to the eye upon illumination with UV light, but differ in color. Crystals of **1** are yellow in color and produce blue emission, while crystals of **2** are colorless, with purple/blue emission, consistent with their structural differences as outlined below. Figure 2.5 shows combined excitation/emission spectra of crystalline **1** and **2** soaked in chloroform, compared to a powder sample of *trans*-4,4'-stilbene dicarboxylic acid (LH_2) precursor. The emission spectrum of **2** in the solid is nearly identical in position to dilute solutions of LH_2 in DMSO/H_2O (100:1 v/v) (see Supporting Information), suggesting little contribution from the Zn_4O clusters to the emission; the red-shift observed for these species compared to *trans*-stilbene itself[30] is consistent with the small increase in conjugation due to the carboxylate units.

The differences observed in the electronic spectra for **1** and **2** likely have their origins in a number of factors, including the local coordination environment of the ligand and the steric proximity of ligands to each other and to other species present in the unit cell. The zinc cluster types in **1** and **2** may potentially exert disparate influences on the local electronic structure of the linker unit (for example, the clusters may differ significantly in Lewis acidity). However, studies of related MOFs suggest that the electronic influence of this cluster type is likely to be small. The excitation spectrum of IRMOF-1 is reported to be very similar to that of powdered 1,4-benzene dicarboxylic acid disodium salt; that is, the Zn_4O clusters in the framework do not perturb the electronic structure of the linker significantly.[41] Theoretical studies of this MOF indicate that the highest occupied valence levels are dominated by *p*-orbitals of the aromatic carbon atoms with a small contribution from the carboxylate atoms;[21] additionally, related studies suggest that the band gap in IRMOF-1 remains unchanged when the Zn atom is replaced by Be, Mg, Ca, or Cd.[42] Very recently, 2-D cadmium MOFs containing the fluorophore 5-sulfosalicylic acid (SSA) were found to display intense ligand-based emission with a small red-shift observed between solid samples of the free ligand and the complex (388 nm *vs*. 394 nm); DFT MO calculations suggest that this bathochromic shift is due to deprotonation of H_3SSA and not coordination to Cd^{2+}.[43] We have found that the differences observed between dilute solutions of LH_2 and its disodium salt (8 nm red-shift in emission for Na_2L, see Supporting Information) are small in comparison to the differences observed between the electronic spectra of **1** and **2** (≥30 nm difference in emission).

Furthermore, two 2-D zinc MOFs based on norfloxacin are reported to exhibit ligand-based emission; they have similar coordination environments (both octahedral Zn^{2+} bound to two carboxylate ligands), but their emission properties differ. A significant blue-shift (420 nm *vs*. 440 nm) is observed for the lower-density structure compared to both the higher-density material and the powdered ligand (which display very similar emission). These differences are attributed to a decrease in inter-ligand $\pi-\pi$ interactions in the lower density structure.[44] Therefore, we believe the differences between spectra of **1** and **2** are likely a result of crystal density, as the evidence indicates that the influence of the different types of zinc cluster on the electronic spectra observed is small compared to that of the differences in inter-chromophore interaction within each structure. This is supported by time-resolved studies described in detail below.

Crystals of **1** and **2** both show structured emission bands similar to that for LH_2 in the solid state (Figure 2.5) and in solution, with several vibronic bands evident. This supports our interpretation that emission is essentially ligand-based, with little contribution from the metal cluster units in the framework. The behavior observed for **2** differs from that described in the literature for IRMOF-1, for which green luminescence is attributed to energy transfer from the relatively non-fluorescent linker (1,4-benzene dicarboxylate) to the Zn_4O units.[41] The emission spectrum of **2** is similar in structure to *trans*-stilbene in dilute solution[1] and in the crystalline state[45] (which has a herringbone packing structure),[46] although for both **1** and **2** the vibronic structure is more pronounced at room temperature. This indicates that the stilbene units are rigidified in **1** and **2**; indeed, this structure resembles that for synthetically-locked stilbene derivatives,[33] as discussed in more detail below. The local site symmetry of the ligand in each structure is likely to have a significant influence on the relative intensities of the vibronic bands evident;[47] however a detailed interpretation of the differences observed between **1** and **2** in this context is beyond the scope of the current study. We note, however, that the relative ratios of the vibronic peaks were found to vary between samples of **1**, yet remained nearly identical amongst many different crystals of **2**.

The fine structure displayed in solid-state electronic spectra of conjugated organic molecules has received a great deal of attention, as analysis can reveal information about the interactions between chromophore units and chromophore rigidity, along with variations in the environmental geometry.[33,48] The intensity of the lowest energy emission peak (0-0) is sensitive to the degree of inter-chromophore coupling, decreasing significantly upon chromophore aggregation. Cofacial arrangements ≤ 4 Å apart typically show strong intermolecular coupling *via* $\pi-\pi$ overlap,[26] resulting in substantial loss of electronic fine structure. Non-cofacial chromophore assemblies and/or those further apart in space (*ca.* 4 Å to 8 Å) can show an intermediate degree of coupling, the details of which depend significantly on the geometry of the arrangement. Trap emission in solid PPV films has been attributed to the creation of stilbenoid dimers, which form excimers that give a red-shifted, structureless emission band with a radiative lifetime significantly longer than for the individual chromophore.[1] The vibronic structure in the emission spectra of both **1** and **2** is well resolved, so a large contribution of excimer emission to the spectra of both crystals can be ruled out. Neither **1** nor **2** show short cofacial chromophore distances in their crystal structures. The nearest-neighbor distances between aromatic ring centroids and the angles between ring planes are 5.6 Å, 79° (**1**, in an individual layer), 6.0 Å, 0° (**1**, between adjacent layers) and 5.6 Å, 49° (**2**, between interpenetrated cubes along the edge defined by the *b*-axis).

Crystals of **1** show a small red-shift and broadening in emission compared to **2**, indicating a greater degree of inter-chromophore coupling in the 2-D MOF structure, likely due to the 6.0 Å distance between chromophores in the displaced face-to-face stacking of successive layers. However, the extent of this chromophore interaction in **1** is small compared to LH_2, which displays a significantly red-shifted and broadened emission spectrum. Here, presumably, hydrogen bonding between terminal carboxylic acid groups introduces short inter-chromophore stacking distances, as observed for *trans*-4,4'-stilbene diamides[49] which show emission spectra characteristic of edge-to-face dimers[50] (5.0 Å between phenyl ring centroids, 28° between ring planes). As described above, the emission spectrum of **2** is very similar to that of LH_2 in dilute solution, indicating these units interact only weakly with one another in this low density 3-D MOF environment.

The differences between excitation and emission maxima apparent for both **1** and **2** are significantly smaller than for dilute solutions of *trans*-stilbene (~ 3400 cm^{-1} in dioxane)[1] and LH_2 (4088 cm^{-1} in DMSO/H_2O (100:1 v/v)), and this difference is smallest for **2** (815 cm^{-1} (**2**) versus 1215 cm^{-1} (**1**)). These data indicate the degree of reorganization between the ground and first excited states of **1** and **2** is reduced compared to *trans*-stilbene and LH_2 in solution, likely due to increased rigidity of the stilbenoid unit afforded through strong coordination by the metal ions in the framework, which results in a larger barrier for torsion about the central ethylene bond.

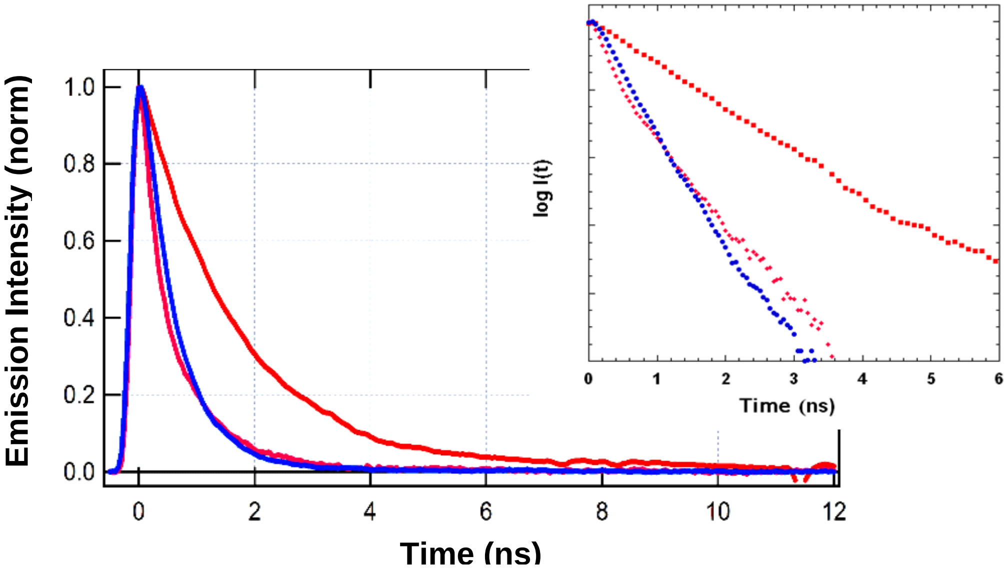

Figure 2.6. Emission decays (left) of **1** (pink), **2** (blue), and LH_2 (red), and semi-logarithmic emission decay plots (right). All three were detected at their respective third vibronic peak (see Figure 5). Emission lifetimes (τ) were determined by fitting the decays to a single or double exponential function: $I(t) = \alpha_1 e^{-t/\tau 1} + \alpha_2 e^{-t/\tau 2}$, where α is the pre-exponential factor, and t is the time. Both **1** and LH_2 were best fit to bi-exponentials, as supported by the semi-logarithmic plots (inset) where the presence of more than one decay process with characteristic lifetime results in curvature of these spectra; $\tau_1 = 0.20$ ns, $\tau_2 = 0.95$ ns, $\alpha_1/\alpha_2 = 5.0$ for **1** and $\tau_1 = 0.73$ ns, $\tau_2 = 2.49$ ns, $\alpha_1/\alpha_2 = 1.8$ for LH_2 In comparison, **2** was best fit to a monoexponential decay $\tau_1 = 0.50$ ns, resulting in a linear semi-logarithmic plot.

Time-resolved emission measurements were used to probe further the local environment of stilbenoid units in crystals of **1** and **2**, and emission decay curves are shown in Figure 2.6. The radiative lifetime of *trans*-stilbene (τ) is estimated to be 1.7 ns,[51] which typically becomes shortened to $\tau < 100$ ps in solution at room temperature. The major factor contributing to the reduced lifetime is the *trans-cis* isomerization.[30] These isomers are nearly isoenergetic in the ground state, but a large barrier to rotation exists and the *trans* state acts as a quantum well. Excitation to the first excited-singlet state is followed by barrierless rotation about the central double bond, leading to the essentially non-fluorescent *cis* isomer,[29,32] which can give additional photoproducts, including cyclization to dihydrophenanthrene. This photoisomerization QY is significantly larger than the fluorescence quantum yield at room temperature ($\theta_{PI} = 45$ *vs*. $\theta_{EM} = 0.02$ in acetonitrile).[5]

Emission decays for **1** were fit best by a bi-exponential function. The faster component has $\tau \sim 0.20$ ns, likely due to emission from monomeric stilbenoid units. The relative contribution of the longer-lived species, with a lifetime of 0.95 ns, was found to increase upon increasing the detection wavelength, along with a concomitant delay observed in the decay curve (see Supporting Information for excitation-wavelength dependent spectra). Growth of a decay component with longer lifetime at lower emission energy, along with a delay in emission, is indicative of an excited state process (i.e. population of the long-lived emissive state occurs after initial excitation), likely facilitated by interactions between individual chromophores in **1**.[53] Consistent with this, LH_2 powder samples show significantly more pronounced behavior in this regard due to much stronger inter-chromophore coupling. The steady-state emission spectra of **1** remain unchanged upon variation of the excitation wavelength across the full excitation spectrum, indicating there is likely to be only one species contributing to the emission,[54] supporting the assignment of these differences in the time-resolved spectra to an excited-state activated process. In addition, the time-resolved data were found to be reproducible between different crystal samples. These considerations allow us to discount significant influence of sample heterogeneity upon the experiments. The behavior exhibited by **1** is consistent with that found by Bazan and coworkers for paracyclophane-based stilbenoid dimers, which exhibit biexponential emission decays in solution, presumably from different electronic states localized on the monomer and dimer.[2] The longer emission lifetime of **1** is of the order of those found for stilbenoid dimers in the intermediate coupling regime.[50] No changes in the time-resolved spectra for **1** are found between samples immersed in chloroform and those dried *in vacuo*.

In contrast, emission decays for **2** (in a chloroform environment) were best fit by a mono-exponential function with $\tau = 0.50$ ns, attributed to emission from stilbenoid monomers. The measured lifetime is approximately five times greater than for *trans*-stilbene in solution, consistent with an increased rigidity of coordinated stilbenoid chromophores in **2**. Typically, increased lifetimes accompany an increase in emission QYs, provided that the radiative decay rate does not change,[55] and, therefore, the QY of both **1** and **2** may be expected to be larger than for *trans*-stilbene in solution. However, values were not determined in this study as variations in crystal size and shape can introduce significant uncertainties into the measurements.

An increase in the luminescence lifetime for **2** may be expected when considering the strong coordination to the Zn_4O units in the crystals. However, this lifetime is shorter than that of "chemically"-frozen stilbenes and those highly-rigidified in solid matrices shown previously,[56] indicating that the structure is not completely rigid, and thus, non-radiative decay pathways are not fully suppressed. We and others have recently addressed the flexibility of MOF-type structures by theoretical means. Molecular dynamics simulations using a newly developed non-rigid force-field indicate that there is considerable motion of the linker groups in IRMOF-1 (Zn_4O(1,4-benzene dicarboxylate)$_3$) at room temperature.[57] In addition, Mattesini et al. have used plane-wave density function theory to predict the elastic properties of IRMOF-1 and concluded that, contrary to what was originally thought for this archetypal isoreticular structure, IRMOF-1 is actually *not* an exceptionally rigid material. Instead, the calculations predict it to be a soft and ductile material, with a Young's modulus of 14.8 GPa.[58] Most recently, it was shown that lattice motions need be included to accurately simulate molecular transport in IRMOF-1.[59] By analogy with these results, the porous stilbene-containing structure of **2** (with a longer and less-rigid ligand than IRMOF-1) is expected to provide an environment with increased rigidity and isolation of ligands, yet flexibility for active interaction with guests incorporated into the open framework.

To investigate the effects of guest molecule incorporation, the emission spectra of **1** and **2** were recorded after exposure to different solvents. Crystals of **1** exhibit no change in emission upon changing solvent environment, and likewise show no significant difference after drying for extended periods under vacuum. This is likely a function of the dense, rigid structure of **1**, wherein the majority of chromophores are not exposed to the solvent. In contrast, the luminescence from crystals of **2** is sensitive to solvent exchange. Shifts in emission were observed upon changing the solvent, with peak maxima decreasing in energy in the order hexane > chloroform > toluene, alongside a concurrent broadening of the vibronic structure, (Figure 2.7). This response was found to be fully reversible through multiple cycles of exchanges between the different solvents. However, upon complete removal of incorporated solvent *in vacuo*, crystals of **2** display a significant, irreversible red-shift in emission, indicating increased inter-ligand coupling, as shown in the inset of Figure 7. This behavior is likely ascribable to a permanent structural change which brings the stilbenoid linker units in closer proximity to one another, and provides evidence for the structural collapse of interpenetrated units upon evacuation as hypothesised above, resulting in the lower-than-expected surface areas discussed previously. These results also indicate that the dynamic nature of the lattice of **2** could allow for specific guest-host interactions with this linker, which may have potential application in combined separation and detection experiments.

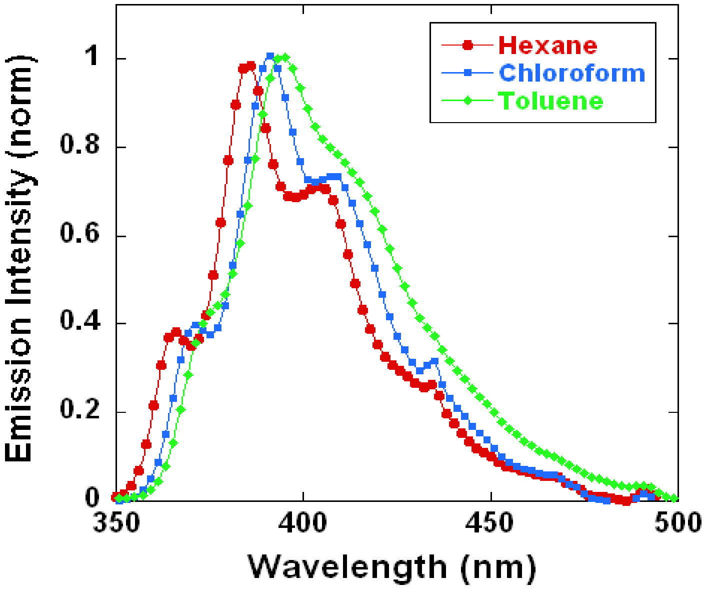

Figure 2.7. Solvent-dependent, normalized emission spectra from a crystal of **2** soaked in toluene (green diamonds), chloroform (blue squares), and hexane (red circles). These are fully reversible upon solvent exchange. The inset shows crystals of **2** in chloroform (blue closed circles) and crystals after extended evacuation, under nitrogen (orange open circles). The original spectrum can not be fully regenerated upon rewetting in chloroform, due to a partial structural collapse in the crystal upon evacuation.

Summary

We have prepared two luminescent stilbene-based MOFs in which the organic linker serves as the chromophore. The structure of the materials obtained is a function of the synthetic conditions employed. Single-crystal XRD and electronic spectroscopy were used to investigate the local environments of the stibenoid units in the frameworks. In both cases, the ligand becomes rigidified in the *trans* geometry upon coordination to the metal. In the dense, 2-D layered structure, **1**, the chromophore environment allows for a limited degree of ligand-ligand interaction. The porous 3-D cubic framework, **2**, exhibits less significant inter-chromophore interaction, and the stilbenoid units maintain a degree of flexibility for dynamic interactions with guests. Initial studies reveal that crystals of **2** show reversible, guest solvent-dependent emission. Sensing with an inherently luminescent MOF with the potential to undergo dynamic shape changes with specific guests is an exciting possibility that we hope to explore in future separations-based experiments.

Experimental

Synthesis. *trans*-4,4'-Stilbene dicarboxylic acid (LH_2) and *N,N*-dimethylformamide (DMF) were purchased from Alfa Aesar. $Zn(NO_3)_2\cdot 6H_2O$ and chloroform ($CHCl_3$) were purchased from Fluka. *N,N*-Diethylformamide (DEF) was purchased from TCI America.

<u>1</u>: 71.3 mg LH_2 was added to 20 mL of DMF in a Pyrex glass jar and agitated until almost fully dissolved. To this was added 209.2 mg $Zn(NO_3)_2\cdot 6H_2O$ (3:1 mole ratio of metal to linker). This was sealed and placed in an oven at 75 °C for 16 hours, followed by 85 °C for 4 hours, yielding transparent yellow crystals of **1**. These were collected and washed three times with fresh DMF, three times with chloroform, dried at 65 ^{o}C in vacuo for 6 hours and then stored under ambient conditions. Yield: 75.2 mg (74% based on LH_2). Analysis calcd. (%) for $Zn_3L_3(DMF)_2$: C 56.83, H 3.89, N 2.45; found: C 56.61, H 4.39, N 2.88. IR (KBr, cm^{-1}): 3424 (br, w), 3060 (w), 2998 (w), 2927 (w), 1660 (s), 1607 (s), 1544 (s), 1394 (br), 1182 (m), 1109 (m), 1056 (w), 1014 (m), 979 (m), 906 (m), 867 (m), 856 (m), 805 (m), 793 (s), 714 (s), 684 (m), 644 (s), 569 (m), 524 (m), 473 (w). Solid state UV/vis (KBr, λ_{max}): 366 nm, 336 nm. TGA indicates loss of coordinated solvent beginning at 250 °C, followed by full decomposition.

<u>2</u>: 30.7 mg of LH_2 was added to 20 mL DEF in a Pyrex glass jar and sonicated upon light heating to enable its suspension. 209.2 mg $Zn(NO_3)_2\cdot 6H_2O$ was added and the jar sealed (6:1 mole ratio of metal to linker). This was placed in an oven at 105 °C for 16 hours yielding transparent colorless crystals of **2**. DEF was decanted while still hot and replaced by DMF. Crystals of **2** were washed with chloroform three times and stored in chloroform until ready for use. Yield 33.8 mg (70% based on LH_2). Analysis calcd. (%) for $Zn_4OL_3(DMF)(CHCl_3)$: C 49.20, H 3.03, N 1.10; found: C 49.70, H 3.24, N 1.08. IR (KBr, cm^{-1}): 3455 (br), 3024 (w), 3008 (w), 1606 (s), 1540 (s), 1395 (br), 1180 (s), 1102 (m), 1014 (m), 953 (w), 858 (m), 784 (s), 751 (m), 708 (s), 671 (w), 646 (m), 569 (w). Solid state UV/vis (KBr, λ_{max}): 378 nm, 334 nm. TGA indicates continuous loss of adsorbed solvent until 200 °C and sharp decomposition at 410 °C.

Physical characterization. TGA was performed on a Pyrus II Perkin Elmer under He. Surface areas were measured on a Micromiretics ASAP 2000 Porosimeter with N_2 as the sorption gas. Powder XRD was performed on a Scintag X'Pert with CuKα radiation. Steady-state emission spectra were collected with a SPEX Fluoromax with a fiber optic extension for solids.

Single crystal diffraction. Data were collected on a Bruker three-circle diffractometer equipped with a SMART APEX-II CCD area detector with graphite-monochromated Mo$K\alpha$ radiation ($\lambda = 0.71073$ Å, $2\theta = 52^{o}$). $Zn_3L_3(DMF)_2$, **1**, $C_{54}H_{44}N_2O_{14}Zn_3$, Mr = 1141.02, rhombohedral, space group $R\,\bar{3}$, at $T = 100.0(2)$ K: $a = 16.1661(4)$, $c = 16.4796(9)$ Å, $V = 3729.82(19)$ Å^3, $Z = 3$, $d_{calc} = 1.524$ g/cm^3, $F(000) = 1752$, $\mu = 1.506$ mm^{-1}. The structure was solved by direct methods and refined by full-matrix least-squares refinement with anisotropic displacement parameters for all non-hydrogen atoms. Two coordinated monodentate DMF ligands are disordered over three sites relative to the 3-fold axis. The hydrogen atoms were generated geometrically and included in the refinement with fixed position and thermal parameters. Final R-factors were $R_1 = 0.0242$ for 1239 reflections with $I \geq 2\sigma(I)$ and wR_2 = 0.0586 for all 1480 ($R_{int} = 0.035$) independent reflections. The maximum and minimum peaks on the final difference Fourier map corresponded to 0.258 and -0.307 e/Å^3, respectively. All calculations were carried out using the SHELXTL (PC Version 6.12) program.

Zn_4OL_3, **2**, $C_{48}H_{30}O_{13}Zn_4$, Mr = 1076.2, orthorhombic, space group Pnnm, at T = 100.0(2) K: a = 30.317(12), b = 19.411(8), c = 24.161(9) Å, V = 14218(10) Å^3, Z = 4, d_{calc} = 0.503 g/cm^3, F(000) = 2168, μ = 0.687 mm^{-1}. Refinement of 151 parameters on 5100 independent reflections out of 62286 measured reflections (R_{int} = 0.1229) led to R_1 = 0.0656 ($I > 2\sigma(I)$), wR_2 = 0.1662 (all data), S = 1.001. The maximum and minimum peaks on the final difference Fourier map corresponded to 0.564 and -0.447 e/Å^3, respectively. All calculations were carried out using the SHELXTL (PC Version 6.12) program. Contribution from disordered guest molecules was accounted for using the SQUEEZE subroutine within the PLATON software package. Statistics prior to treatment of data with SQUEEZE were R_1 = 0.1325 ($I > 2\sigma(I)$), wR_2 = 0.3866 (all data) and S = 1.459. Calculation of the total solvent-accessible volume was performed using the CALC SOLV routine within the PLATON software package.

Emission lifetimes. A mode-locked Nd:YAG laser was regeneratively amplified and frequency tripled to produce nearly transform-limited 355 nm pulses. The repetition rate was 20 Hz. The pulse width of the frequency-tripled output of the regeneration is estimated to be approximately 60 ps (FWHM). The 355 nm pulses were focused onto the sample. Emission was collected with an f/4 visible achromat and imaged 1:1 with a second achromat onto the 200 mm wide entrance slit of a 1/8 m monochromator. A 600 lines mm^{-1} grating (blazed for 300 nm) dispersed the emission. The 1200 μm wide exit slit width produced a nearly rectangular bandpass of 7.5 nm. The grating was tuned to collect emission from individual vibronic bands (based on fluorimeter measurements). The filtered emission was detected with a microchannel plate photomultiplier tube (MCP-PMT), and the resulting signal was digitized with a real-time digital oscilloscope and with an analog bandwidth of 6 GHz. The rise time of the detection system is ~150 ps, the fall time is ~300 ps, and the FWHM is ~300 ps. A convolve-and-compare algorithm was used to fit the data with a two-component exponential decay including convolution with the instrument response function, which was recorded by measuring the elastically scattered 355-nm light from the sample substrate. The slight impedance mismatch between the detector, cabling, and oscilloscope produces minor post-pulse ringing (<0.5%), which necessitates convolution in the fitting procedure for accurate determination of decay rates.

References

(1) Gierschner, J.; Mack, H. G.; Oelkrug, D.; Waldner, I.; Rau, H. *J. Phys. Chem. A* **2004**, *108*, 257-263.

(2) Bazan, G. C.; Oldham, W. J.; Lachicotte, R. J.; Tretiak, S.; Chernyak, V.; Mukamel, S. *J. Am. Chem. Soc.* **1998**, *120*, 9188-9204.

(3) Shukla, A. D.; Strawser, D.; Lucassen, A. C. B.; Freeman, D.; Cohen, H.; Jose, D. A.; Das, A.; Evmenenko, G.; Dutta, P.; van der Boom, M. E. *J. Phys. Chem. B* **2004**, *108*, 17505-17511.

(4) Rowsell, J. L. C.; Yaghi, O. M. *Micropor. Mesopor. Mater.* **2004**, *73*, 3-14.

(5) Janiak, C. *J. Chem. Soc., Dalton Trans.* **2003**, 2781-2804.

(6) Kitagawa, S.; Kitaura, R.; Noro, S. *Angew. Chem. Int. Ed.* **2004**, *43*, 2334-2375.

(7) Rowsell, J. L. C.; Yaghi, O. M. *J. Am. Chem. Soc.* **2006**, *128*, 1304-1315.

(8) Millward, A. R.; Yaghi, O. M. *J. Am. Chem. Soc.* **2005**, *127*, 17998-17999.

(9) Horcajada, P.; Serre, C.; Vallet-Regi, M.; Seban, M.; Taulelle, F.; Ferey, G. *Angew. Chem. Int. Ed.* **2006**, *45*, 5974-5978.

(10) Lee, E. Y.; Suh, M. P. *Angew. Chem. Int. Ed.* **2004**, *43*, 2798-2801.

(11) Kitaura, R.; Fujimoto, K.; Noro, S.-I.; Kondo, M.; Kitagawa, S. *Angew. Chem. Int. Ed.* **2002**, *41*, 133-135.

(12) Chen, B. L.; Liang, C. D.; Yang, J.; Contreras, D. S.; Clancy, Y. L.; Lobkovsky, E. B.; Yaghi, O. M.; Dai, S. *Angew. Chem. Int. Ed.* **2006**, *45*, 1390-1393.

(13) Seo, J. S.; Whang, D.; Lee, H.; Jun, S. I.; Oh, J.; Jeon, Y. J.; Kim, K. *Nature* **2000**, *404*, 982-986.

(14) Wu, C. D.; Hu, A.; Zhang, L.; Lin, W. B. *J. Am. Chem. Soc.* **2005**, *127*, 8940-8941.

(15) Evans, O. R.; Lin, W. B. *Acc. Chem. Res.* **2002**, *35*, 511-522.

(16) Lee, E. Y.; Jang, S. Y.; Suh, M. P. *J. Am. Chem. Soc.* **2005**, *127*, 6374-6381.

(17) Wang, X. L.; Chao, Q.; Wang, E. B.; Lin, X.; Su, Z. M.; Hu, C. W. *Angew. Chem. Int. Ed.* **2004**, *43*, 5036-5040.

(18) Chandler, B. D.; Cramb, D. T.; Shimizu, G. K. H. *J. Am. Chem. Soc.* **2006**, *32*, 10403-10412.

(19) de Lill, D. T.; Gunning, N. S.; Cahill, C. L. *Inorg. Chem.* **2005**, *44*, 258-266.

(20) Wang, Z.; Jin, C. M.; Shao, T.; Li, Y. Z.; Zhang, K. L.; Zhang, H. T.; You, X. Z. *Inorg. Chem. Comm.* **2002**, *5*, 642-648.

(21) Civalleri, B.; Napoli, F.; Noel, Y.; Roetti, C.; Dovesi, R. *CrystEngComm* **2006**, *8*, 364-371.

(22) Kaschuck, Y.; Esposito, B. *Nuc. Inst. Meth. Phys. Res.* **2005**, *551*, 420-428.

(23) Zojer, E.; Beljonne, D.; Kogej, T.; Vogel, H.; Marder, S. R.; Perry, J. W.; Bredas, J. L. *J. Chem. Phys.* **2002**, *116*, 3646-3658.

(24) Zhu, L. Y.; Yi, Y. P.; Shuai, Z. G.; Bredas, J. L.; Beljonne, D.; Zojer, E. *J. Chem. Phys.* **2006**, *125*, 044101.

(25) Albota, M. et al. *Science* **1998**, *281*, 1653-1656.

(26) Cornil, J.; dos Santos, D. A.; Crispin, X.; Silbey, R.; Bredas, J. L. *J. Am. Chem. Soc.* **1998**, *120*, 1289-1299.

(27) Cacialli, F.; Chuah, B. S.; Kim, J. S.; dos Santos, D. A.; Friend, R. H.; Moratti, S. C.; Holmes, A. B.; Bredas, J. L. *Synth. Met.* **1999**, *102*, 924-925.

(28) Meier, H. *Angew. Chem. Int. Ed.* **1992**, *31*, 1399-1420.

(29) Saltiel, J. *J. Am. Chem. Soc.* **1967**, *89*, 1036-1037.

(30) Waldeck, D. H. *Chem. Rev.* **1991**, *91*, 415-436.

(31) Ramamurthy, V.; Caspar, J. V.; Corbin, D. R.; Eaton, D. F. *J. Photochem. Photobiol. A* **1990**, *51*, 259-263.

(32) Simeonov, A.; Matsushita, M.; Juban, E. A.; Thompson, E. H. Z.; Hoffman, T. Z.; Beuscher, A. E.; Taylor, M. J.; Wirsching, P.; Rettig, W.; McCusker, J. K.; Stevens, R. C.; Millar, D. P.; Schultz, P. G.; Lerner, R. A.; Janda, K. D. *Science* **2000**, *290*, 307-313.

(33) Oelgemoller, M.; Brem, B.; Frank, R.; Schneider, S.; Lenoir, D.; Hertkorn, N.; Origane, Y.; Lemmen, P.; Lex, J.; Inoue, Y. *J. Chem. Soc., Perkin Trans. 2* **2002**, 1760-1771.

(34) Saltiel, J.; Marinari, A.; Chang, D. W. L.; Mitchener, J. C.; Megarity, E. D. *J. Am. Chem. Soc.* **1979**, *101*, 2982-2996.

(35) Letsinger, R. L.; Wu, T. F. *J. Am. Chem. Soc.* **1995**, *117*, 7323-7328.

(36) Halper, S. R.; Do, L.; Stork, J. R.; Cohen, S. M. *J. Am. Chem. Soc.* **2006**, *128*, 15255-15268.

(37) Eddaoudi, M.; Li, H. L.; Yaghi, O. M. *J. Am. Chem. Soc.* **2000**, *122*, 1391-1397.

(38) Park, G.; Kim, H.; Lee, G. H.; Park, S.-K.; Kim, K. *Bull. Korean Chem. Soc.* **2006**, *27*, 443-446.

(39) Eddaoudi, M.; Kim, J.; Rosi, N.; Vodak, D.; Wachter, J.; O'Keeffe, M.; Yaghi, O. M. *Science* **2002**, *295*, 469-472.

(40) Chen, B.; Ma, S.; Zapata, F.; Lobkovsky, E. B.; Yang, J. *Inorg. Chem.* **2006**, *45*, 5718-5720.

(41) Bordiga, S.; Lamberti, C.; Ricchiardi, G.; Regli, L.; Bonino, F.; Damin, A.; Lillerud, K.-P.; Bjorgenb, M.; Zecchina, A. *Chem. Commun.* **2004**, 2300-2301.

(42) Fuentes-Cabrera, M.; Nicholson, D. M.; Sumpter, B. G.; Widom, M. *Journal of Chemical Physics* **2005**, *123*, 124713.

(43) Lu, Z.; Wen, L.; Ni, Z.; Li, Y.; Zhu, H.; Meng, Q. *Cryst. Growth Des.* **2007**, *7*, 268-274.

(44) Chen, Z.-F.; Xiong, R.-G.; Zhang, J.; Chen, X.-T.; Xue, Z.-L.; You, X.-Z. *Inorg. Chem.* **2001**, *40*, 4075-4077.

(45) Gudipati, M. S. *J. Phys. Chem.* **1993**, *97*, 8602-8607.

(46) Hoekstra, A.; Meertens, P.; Vos, A. *Acta Cryst. B* **1975**, *31*, 2813-2817.

(47) Pope, M.; Swenberg, C. E. *Electronic Processes in Organic Crystals and Polymers*; 2nd ed.; Oxford Science Publications: New York, 1999.

(48) Spano, F. C. *Ann. Rev. Phys. Chem.* **2006**, *57*, 217-243.

(49) Lewis, F. D.; Yang, J. S.; Stern, C. L. *J. Am. Chem. Soc.* **1996**, *118*, 12029-12037.

(50) Lewis, F. D.; Yang, J. S.; Stern, C. L. *J. Am. Chem. Soc.* **1996**, *118*, 2772-2773.

(51) Syage, J. A.; Lambert, W. R.; Felker, P. M.; Zewail, A. H.; Hochstrasser, R. M. *Chem. Phys. Lett.* **1982**, *88*, 266-270.

(52) Mazzucato, U. *Pure Appl. Chem.* **1982**, *54*, 1705-1721.

(53) Song, Q.; Bohn, P. W.; Blanchard, G. J. *J. Phys. Chem. B* **1997,** *101*, 8865-8873.

(54) Haas, E.; Fischer, G.; Fischer, E. *J. Phys. Chem.* **1978**, *82*, 1638-1643.

(55) Lakowicz, J. R. *Principles of Fluorescence Spectroscopy*; 2 ed.; Plenum US: New York, NY, 1999.

(56) Pyun, C.-H.; Lyle, T. A.; Daub, G. H.; Park, M. *Chem. Phys. Lett.* **1986**, *124*, 48-52.

(57) Greathouse, J. A.; Allendorf, M. D. *J. Am. Chem. Soc.* **2006**, *128*, 10678-10679.

(58) Mattesini, M.; Soler, J. M.; Yndurain, F. *Phys. Rev. B* **2006**, *73*, 094111.

(59) Amirjalayer, S.; Tafipolsky, M.; Schmid, R. *Angew. Chem. Int. Ed.* **2007**, *46*, 463-466.

2b. Effect of the Coordinated Metal on Luminescence in Stilbene Metal-Organic

Introduction

Metal organic frameworks are a recent addition to the class of metal coordination polymers. The interest in MOFs is diverse, ranging from fundamental studies and characterization of physical properties to advanced applications including magnetism, sensing, drug delivery, catalysis, and gas storage. An important feature of these materials is that they rely on strong coordination of metal ions or metal clusters by organic linkers to result in extended structures with a variety of geometries, which can be exploited to generate structures with 1D, 2D, or 3D architectures. Conditions have recently been identified that favor specific geometries of the inorganic clusters, termed secondary building units (SBUs), allowing for a degree of predictability in the well-defined extended structures, a desirable trait for many complex applications. The structures and properties can be tailored by changing both the linker and metal, owing to the diversity of metal-organic bonding geometries and variation in linkers. For instance, it was reported that the band gap can be changed with variations in the metal center and the ligand while maintaining the same overall cubic structure.

The linkers that are typically used in MOFs are rigid, and often based on conjugated structures which are held in defined geometries due to strong covalent bonding throughout the crystals. Many of these linkers are fluorescent in their natural state and MOFs provide a framework for them, yet the fluorescence of many of these remains unexplored. Emission properties of MOFs can be metal-based, ligand-based, or a result of charge transfer, including metal-to-ligand charge transfer (MLCT) or ligand-to-metal charge transfer (LMCT). The former is common in lanthanide MOFs, where the emission can be sensitized by the organic ligand. There are a few examples of ligand-based emission in the literature, including that from Cd^{II}, Cu^{I}, and Zn^{II} containing MOFs. LMCT has been identified in some cases of Cd and Zn MOFs as well, mostly in cases where the ligand is a benzene derivative. Increased conjugation results in ligand-based luminescence.

As the organic linkers are held in defined positions throughout the crystals, the properties can be correlated to their environment, which we demonstrated in studying the emission properties of MOFs. We recently reported the use of differing synthetic conditions to prepare two zinc-based MOFs containing a stilbene linker, and found that the emission is characteristic of the ligand with little influence from the metal centers. An interpenetrated 3D cubic structure, consisting of basic zinc acetate units linked by trans-stilbene dicarboxylates exhibited fluorescence similar to a dilute solution of non-interacting stilbenes with increased rigidity. A 2D network was also prepared, with a higher density of stilbene units and exhibits increased, yet limited, linker-linker interactions, as demonstrated by time-resolved and steady state fluorescence studies. However, the differing lewis acidities of the metal clusters in the 2D and 3D MOFs left the question open as to how much this affects the fluorescence properties. In order to further probe the role of the metal in the fluorescence, we sought to synthesize four different, isostructural MOFs based on stilbene dicarboxylic acid. We successfully prepared three additional 2D MOFs with similar procedures, containing Cd, Mn and Co. The synthesis, characterization, and fluorescence properties will be discussed here.

Experimental Section

Synthesis.4,4′-Stilbenedicarboxylic acid (LH_2) and *N,N*-dimethylformamide (DMF) were purchased from Alfa Aesar. $Zn(NO_3)_2{\cdot}6H_2O$ and chloroform were purchased from Fluka. *N,N*-Diethylformamide (DEF) was purchased from TCI America. $Cd(NO_3)_2{\cdot}4H_2O$, $Mn(NO_3)_2{\cdot}4H_2O$ and $Co(NO_3)_2{\cdot}6H_2O$ were purchased from Aldrich.

$Zn_3(SDA)_3DMF_2$ (1) was synthesized as described in the literature.

$Cd_3(SDA)_3DMF_2$, (2): LH_2 (62 mg) was added to DMF (20 mL) in a Pyrex glass jar and agitated until almost fully dissolved. To this was added $Cd(NO_3)_2{\cdot}4H_2O$ (214 mg, 3:1 mole ratio of metal to linker) and the mixture was sealed and placed in an oven at 80 °C for 24 h, yielding transparent, very pale yellow needle-like crystals of **2**. These were collected and washed three times with fresh DMF and three times with chloroform, dried at 65° C *in vacuo* for 6 h, and then stored in ambient conditions. Yield 32 mg (32% based on LH_2, 1st crop of crystals). Analysis calcd (%) for $Cd_3L_3(DMF)_2{\cdot}H_2O$: C 49.88, H 3.57, N 2.15; found C 49.19, H 3.45, N 2.54. IR (crystal sample, cm^{-1}): 3424 (br, w), 3060 (w), 2998 (w), 2927 (w), 1660 (s), 1607 (s), 1544 (s), 1394 (br), 1182 (m), 1109 (m), 1056 (w), 1014 (m), 979 (m), 906 (m), 867 (m), 856 (m), 805 (m), 793 (s), 714 (s), 684 (m), 644 (s), 569 (m), 524 (m), 473 (w).

$Mn_3(SDA)_3DMF_2$, (3): LH_2 (60 mg) was added to DMF (20 mL) in a Pyrex glass jar and agitated until almost fully dissolved. To this was added $Mn(NO_3)_2{\cdot}4H_2O$ (168 mg, 3:1 mole ratio of metal to linker) and the mixture was sealed and placed in an oven at 80 °C for 16 h, followed by 85 °C for 96 h, yielding transparent, colorless needle-like crystals of **3**. These were collected and washed three times with fresh DMF and three times with chloroform, dried at 65 °C *in vacuo* for 6 h, and then stored in ambient conditions. Yield 25 mg (30% based on LH_2, 1st crop of crystals). Analysis calcd (%) for $Mn_3L_3(DMF)_2{\cdot}H_2O$: C 57.51, H 4.11, N 2.48; found C 57.74, H 4.07, N 2.92. IR (crystal sample, cm^{-1}): 3424 (br, w), 3060 (w), 2998 (w), 2927 (w), 1660 (s), 1607 (s), 1544 (s), 1394 (br), 1182 (m), 1109 (m), 1056 (w), 1014 (m), 979 (m), 906 (m), 867 (m), 856 (m), 805 (m), 793 (s), 714 (s), 684 (m), 644 (s), 569 (m), 524 (m), 473 (w).

$Co_3(SDA)_3DMF_2$, (4): LH_2 (42 mg) was added to DMF (10 mL) in a Pyrex glass jar and agitated until almost fully dissolved. To this was added $Co(NO_3)_2{\cdot}6H_2O$ (137 mg, 3:1 mole ratio of metal to linker) and the mixture was sealed and placed in an oven at 85 °C. Initially, a green/brown powder formed which re-dissolved, yielding purple crystals of **4** after 5 days. These were collected and washed three times with fresh DMF and three times with chloroform, dried at 65° C *in vacuo* for 6 h, and then stored in ambient conditions. Yield 20 mg (34% based on LH_2, 1st crop of crystals). X-ray powder diffraction indicated the product obtained was phase-pure and corresponded to that previously described.

Physical Characterization. Infra-red spectra were acquired on a Varian FTS-7000 spectrometer in reflection-absorption geometry using a gold-coated glass slide as sample holder. Thermogravimetric analysis (TGA) was performed on a Netzsch 449C Simultaneous Thermal Analyzer (Selb, Germany) at a heating rate of 10 °C/min under Ar. Powder X-ray diffraction (XRD) was performed on a Scintag X'Pert with Cu Kα radiation. Steady-state emission spectra of solid samples were collected with a SPEX Fluoromax in front-face geometry with emission wavelength $\lambda_{em} = 350$ nm. Solid-state magnetic susceptibility data were obtained using a Quantum Design MPMS-5 SQUID magnetometer. A powdered sample of **3** (13 mg) was placed in a gelatine capsule which was then inserted into a non-magnetic plastic straw. A field-sweep scan between -60000 G and 60000 G at 350 K indicated that susceptibility was a linear function of field with no hysteresis observed. Data were then measured employing fields of 100 G and 1000 G between 5-350 K, and the measured susceptibilities were corrected for the inherent diamagnetism of the sample itself by use of Pascal's constants but did not require correction for the intrinsic weak diamagnetism of the sample holder arrangement.

Single-Crystal XRD. Data were collected on a Bruker three-circle diffractometer equipped with a SMART APEX-II CCD area detector with graphite-monochromated Mo KR radiation ($\lambda = 0.71073$ Å, $2\theta = 58^{o}$). $Cd_3L_3(DMF)_2$, **2**, $C_{54}H_{44}N_2O_{14}Cd_3$, $M_r = 1282.11$, rhombohedral, space group $R\bar{3}$, at $T = 100.0(2)$ K: $a = 16.488(3)$, $c = 16.704(7)$ Å, $V = 3933(2)$ Å^3, $Z = 3$, $d_{calc} = 1.624$ g/cm^3, $F(000) = 1914$, $\mu = 1.273$ mm^{-1}. The structures were solved by direct methods and refined by full-matrix least-squares refinement with anisotropic displacement parameters for all non-hydrogen atoms. Two coordinated monodentate DMF ligands are disordered over three sites relative to the 3-fold axis. The hydrogen atoms were generated geometrically and included in the refinement with fixed position and thermal parameters. Final R-factors were $R_1 = 0.0397$ for 1582 reflections with $I \geq 2\sigma(I)$ and $wR_2 = 0.1069$ for all 2440 ($R_{int} = 0.043$) independent reflections. The maximum and minimum peaks on the final difference Fourier map corresponded to 1.138 and -1.084 e/Å^3, respectively. $Mn_3L_3(DMF)_2$, **2**, $C_{54}H_{44}N_2O_{14}Mn_3$, $M_r = 1109.73$, rhombohedral, space group $R\bar{3}$, at $T = 100.0(2)$ K: $a = 16.3456(19)$, $c = 16.590(4)$ Å, $V = 3838.7(11)$ Å^3, $Z = 3$, $d_{calc} = 1.440$ g/cm^3, $F(000) = 1707$, $\mu = 0.797$ mm^{-1}. The structures were solved by direct methods and refined by full-matrix least-squares refinement with anisotropic displacement parameters for all non-hydrogen atoms. Two coordinated monodentate DMF ligands are disordered over three sites relative to the 3-fold axis. The hydrogen atoms were generated geometrically and included in the refinement with fixed position and thermal parameters. Final R-factors were gt $R_1 = 0.0618$ for 1858 reflections with $I \geq 2\sigma(I)$ and $wR_2 = 0.1826$ for all 2263 ($R_{int} = 0.042$) independent reflections. The maximum and minimum peaks on the final difference Fourier map corresponded to 1.162 and -0.592 e/Å^3, respectively. All calculations were carried out using the SHELXTL (PC Version 6.12) program.All calculations were carried out using the SHELXTL (PC Version 6.12) program.

Results and Discussion

Synthesis and Characterization. Solvothermal reaction of LH_2 and the appropriate metal nitrate in DMF afforded crystals of $M_3L_3(DMF)_2$ (M = Zn, **1**; Cd, **2**; Mn, **3**; Co, **4** respectively), identified by comparison of their powder X-ray diffraction patterns with those reported in the literature (**1** and **4**) or by elemental analysis and single crystal X-ray diffraction (**2** and **3**, see below). In all cases, continued heating of the mother liquor resulted in additional product crystal growth; yields quoted refer to the first crop only. Interestingly, the route described here to give **4** is somewhat different to that previously reported (substituting the nitrate for the perchlorate salt, reacting at 85 °C *vs*. 110 °C) but the crystalline material obtained is identical, illustrating that conditions employed for successful MOF syntheses have a degree of flexibility in certain cases. TGA for **1-3** (Figure 2.8) indicates these materials to have similar thermal stabilities, with loss of coordinated solvent (~13 wt % for **1** and **2**, ~15% for **3**) starting around 250 °C followed by full decomposition.

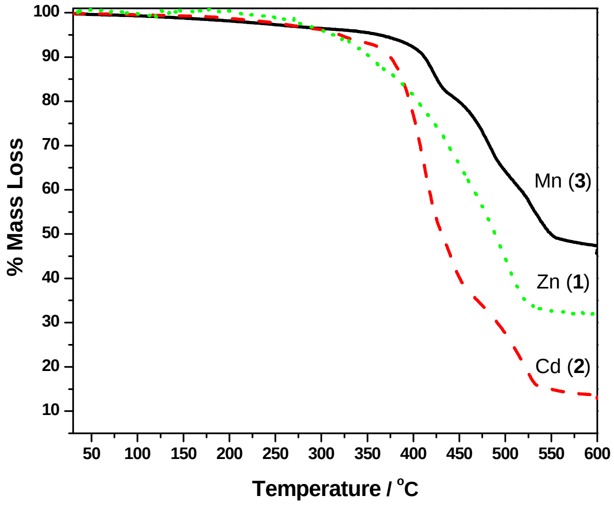

Figure 2.8: TGA analysis of Mn, Cd, Zn stilbene MOFs

Single Crystal X-ray Diffraction

The structures of **2** and **3** were determined by single-crystal XRD, and representations are shown in Figures 2.9 and 2.10. These materials are essentially isostructural with **1** and **4**, featuring trinuclear $M_3(RCO_2)_6$ secondary building units (SBUs) where the central octahedrally-coordinated M^{II} ion is linked to a pair of tetrahedrally-coordinated M^{II} ions *via* bridging carboxylate groups; this tetrahedral geometry is completed at the apices by oxygen atoms of DMF molecules. These SBUs are connected by planar *trans*-4,4'-stilbene units, forming a hexagonal pinwheel network that extends in the *a*,*b*-plane. The DMF molecules exhibit 3-fold disorder with respect to the C_3 axis, and occupy space above and below the layers defined by the *a*,*b*-planes; these layers pack in a cubic motif to give a dense structure without overall porosity. Important bond lengths are given in Table 1; of particular relevance to the discussion of luminescence in the next section are the distances and angles between nearest-neighbor stilbene units in the structure as through-space interchromophore coupling can have significant influence on the position and shape of the emission profile. Each stilbene unit in **1-4** has two nearest neighbors, one in the layer and one in an adjacent layer, and the distances between aromatic ring centroids and the angles between ring planes for each structure are given in Table 2.

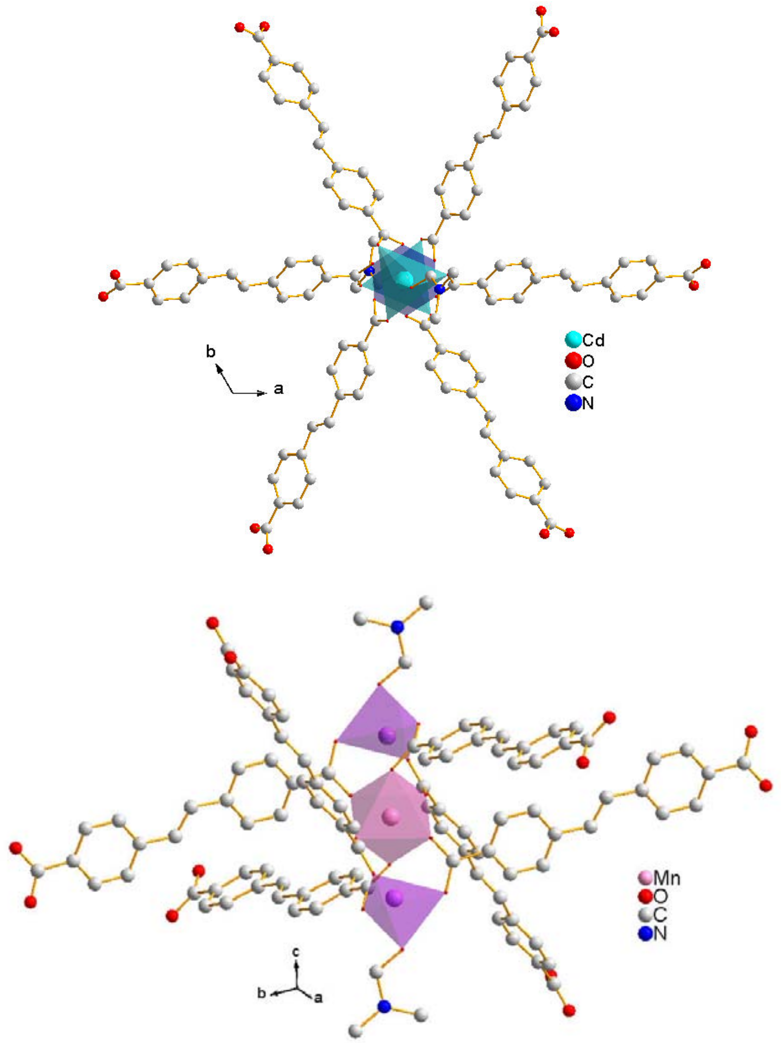

Figure 2.9 and 2.10: Structures of Mn and Cd MOFs as determined by single crystal XRD. The Co MOF was compared to a previously reported structure.

Luminescence

Emission spectra for **1-3** recorded for similar-sized crystal samples with the same experimental setup are shown in Figure 2.11. The emission profiles for **1-3** have significant fine-structure, with several vibronic bands apparent, and are similar to that observed for *trans*-stilbene in solution and the solid states. As discussed in detail in a previous study, these features indicate that the emission is predominantly ligand-based, and suggest the ligand has become significantly rigidified as a result of metal coordination in these framework structures. In that study, differences observed between the emission of a porous 3D Zn-stilbene framework material and that of the dense, 2D framework **1** were attributed primarily to dissimilar through-space ligand-ligand interactions (with a blue-shifted and narrower emission observed for the porous material). However, the degree of influence on the emission spectra for the Zn_4O cluster in the 3D structure *vs*. the trinuclear Zn cluster in the 2D network remained a question. In this work, the close similarity in both position and width for the emission spectra of **1-3**, when coupled with the essentially-identical ligand environments in the structures outlined in Table 2, strongly supports the earlier hypothesis that through-space ligand-ligand coupling is the dominant factor. The Lewis acidities of Zn^{II}, Cd^{II} and Mn^{II} ions are dissimilar and therefore each ion may be expected to perturb the ligand electronic structure to a different degree; however, this influence of Lewis acidity may be concluded to be small compared to the ligand-ligand interactions in the frameworks.

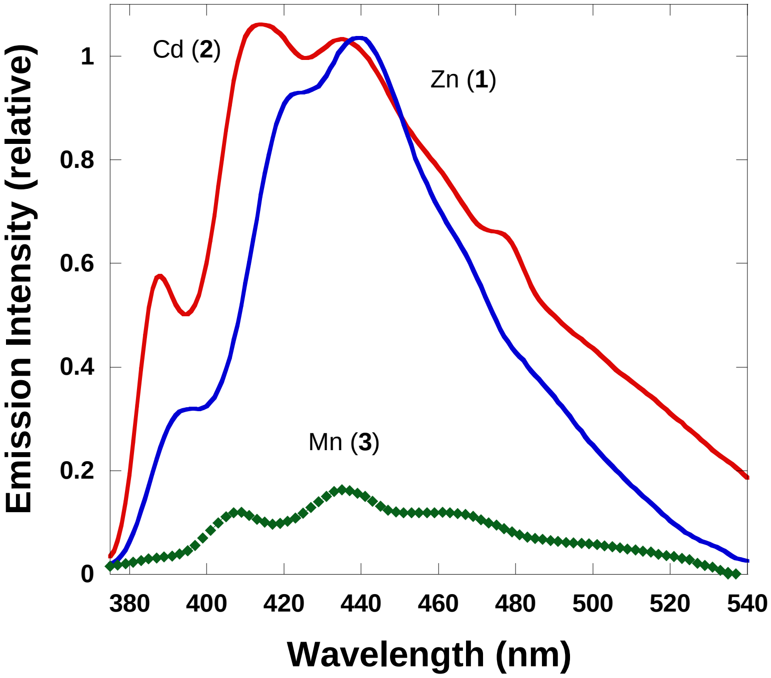

Figure 2.11: Comparative emissions of Mn, Cd, Zn stilbene MOFs. The intensities reflect approximately the difference in intensities from individual crystals of similar size.

Qualitatively, it was observed that emission from **1** and **2** was of comparable brightness, whereas this emission was significantly reduced for **3**. The difference is assigned to through-space dipolar quenching in **3** due to the proximity of the ligand to the high-spin $S = 5/2$ Mn^{II} ions (see section below), which does not occur with the d^{10} Zn^{II} or Cd^{II} ions in **1** and **2**. No emission was observed for **4** under the same conditions; $S = 3/2$ Co^{II} ions are expected to quench emission in a similar fashion and any resulting weak luminescence may be obscured through reabsorption effects (**4** is purple in contrast to the colorless-to-pale-yellow materials **1**-**3**).

Magnetism

The magnetic properties of **3** were investigated by SQUID magnetometry. Figure 2.12 shows a plot of both $1/\chi$ and μ_{eff} per Mn ion (defined as $\mu_{eff} = \sqrt{8\chi T}$) as a function of temperature between 5-350 K (recorded at 100 G). The magnetic moment determined for each Mn^{II} ion at 350 K is 5.76 Bohr Magnetons, which is very close to that calculated for $S = 5/2$ Mn^{II} in the gas-phase (5.92 BM) and indicates the Mn^{II} ions in **3** are high-spin and do not interact with each other to any significant degree, either through-space or *via* mixing with the bridging stilbene ligands. **3** exhibits Curie-Weiss behavior of a simple paramagnet above 10K; least-squares fitting to the Curie-Weiss law affords a Weiss constant of -4K, suggesting a weak degree of antiferromagnetic coupling between Mn^{II} ions at very low temperature.

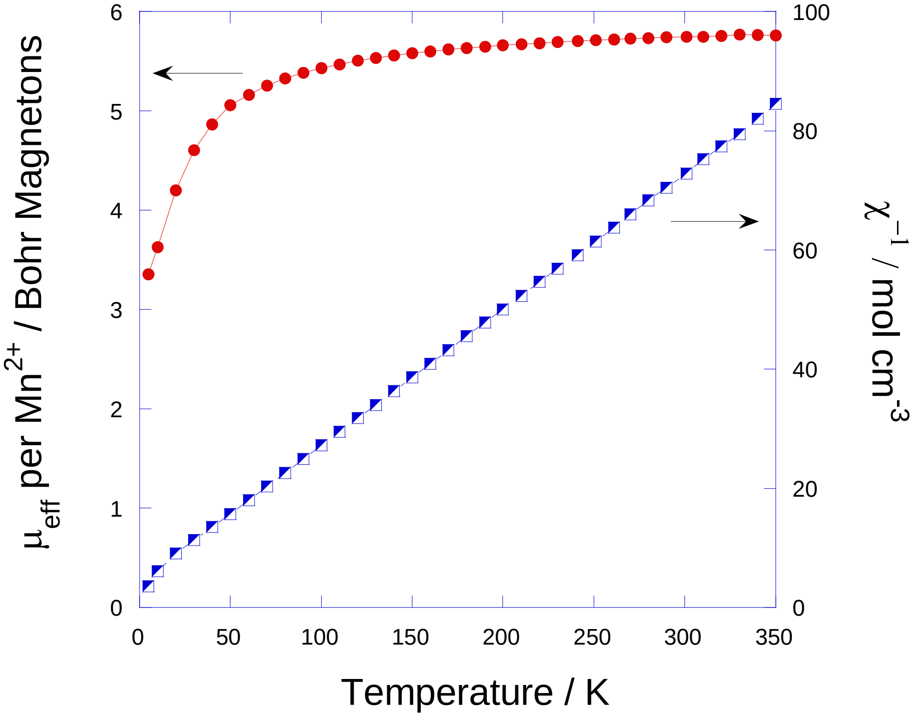

Figure 2.12: SQUID measurements of Mn MOFs

Conclusions

Four isostructural MOFs containing stilbene dicarboxylate linkers were synthesized with the formula M_3L3DMF_2, where M = Zn, Co, Cd, Mn. The orientation of the ligands was very similar in each case, allowing for comparison of the influence of the metal centers on the fluorescence properties of the ligand. Zn and Cd each allowed for highly fluorescent crystals with comparable intensities as there is likely to be little charge transfer between the stilbene and the coordinated d^{10} metals. Both Co and Mn exhibited weaker fluorescence due to quenching by the high spin metal centers. The Co crystals were dark purple, which further hampered measurement of the fluorescence. The fluorescence properties of the Mn crystals were observable yet weak. The fluorescence spectra from Zn, Mn, and Cd were all similar in position and vibrational structure, indicating the lack of influence due to the metal and revealing that the ligand-ligand interactions dominate the properties in these MOFs.

2c. Guest-driven Luminescent MOFs

For the past decade as MOFs evolve from their infancy as novelty materials, a new focus on application science has begun to emerge. While the vast majority of literature dealing with MOFs continues to involve reports on the synthesis and physical properties of new materials, select laboratories have decided to focus their work on tuning and manipulating MOFs into functional materials for applications such as sensing, catalysis, separations, gas storage, non-linear optics, etc. For sensing applications in particular, it is crucial that a signal transduction pathway be incorporated into the MOF material. One of the most widely exploited signaling phenomena in sensing systems is optical modulation. Both light absorption and photon emission are potentially viable transduction pathways, however, for solid-state applications, such as those incorporating MOFs, luminescence emission is by far more straightforward to achieve and measure. To that end, a large part of this project has been the synthesis and testing of new and modified luminescent MOFs. One route which has been pursued is to generate luminescence from a MOF, not through the framework itself, but rather through an adsorbed guest.

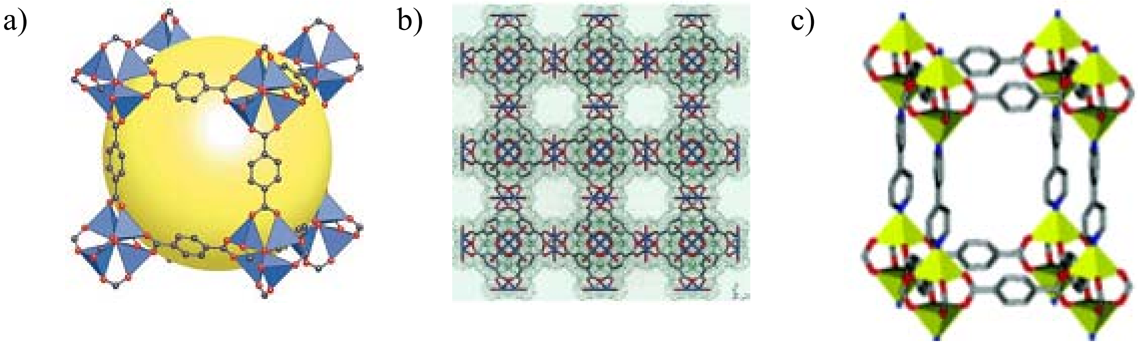

Figure 2.13: Representations of the crystal structures of a) IRMOF-1, b) HKUST-1, and c) MOF-508

The guests chosen for this purpose are the visible light emitting lanthanoid ions, Eu(III) and Tb(III). Eu(III) gives a distinct and characteristic red luminescence whereas Tb(III) emits a bright green light. Several different MOFs were chosen for these adsorption studies as shown in Figure **2.13**. Both IRMOF-1 and HKUST-1 were initially chosen due to their large internal free volumes and readily accessible pore spaces. MOF-508 is a relatively under utilized material, but highly attractive due to its stability, tunability, and especially its flexibility. Based on recent successes in vapor phase infiltration of MOF materials with volatile organometallic compounds,[1-4] initial trials for lanthanoid infusion were conducted using the evacuated permanently porous MOFs and various volatile lanthanoid precursors. This method proved ineffective with less than 1% w/w loading on average based on elemental microanalysis. Further trials were conducted using a solution phase introduction method in which a concentrated organic solution of the lanthanoid salt was added to an evacuated MOF sample. Results with the permanently porous materials IRMOF-1 and HKUST-1 were mixed, whereas infiltration of the flexible structure MOF-508 gave excellent and reproducible lanthanoid saturated material. Elemental microanalysis revealed a loading of >20% w/w for both Tb(III) and Eu(III).

MOF-508 was chosen as a scaffold template not only because of its flexibility and stability, but also because of its potential to sensitize the metal-based luminescence of the infiltrated lanthanoids. The rare earth metals general have weak intrinsic luminescence due to parity forbidden transitions required to achieve excitation to the emitting states. It has been observed, however, that with careful selection of a strongly absorbing organic ligand, an energy transfer can occur between the excited ligand and the lanthanoid ion to produce the appropriate metal excited state for photon emission.[5] This phenomenon has been dubbed the "antenna effect." In MOF-508 the bipyridine pillar ligands are able to act as effective antennas for both Eu(III) and Tb(III) sensitization. The spectra in Figure **2.14** show the effect of this sensitization in that the excitation spectra for both Eu@MOF-508 and Tb@MOF-508 are nearly superimposible, yet the emission spectra are quite different and give the characteristic line spectra of Eu(III) and Tb(III) respectively.

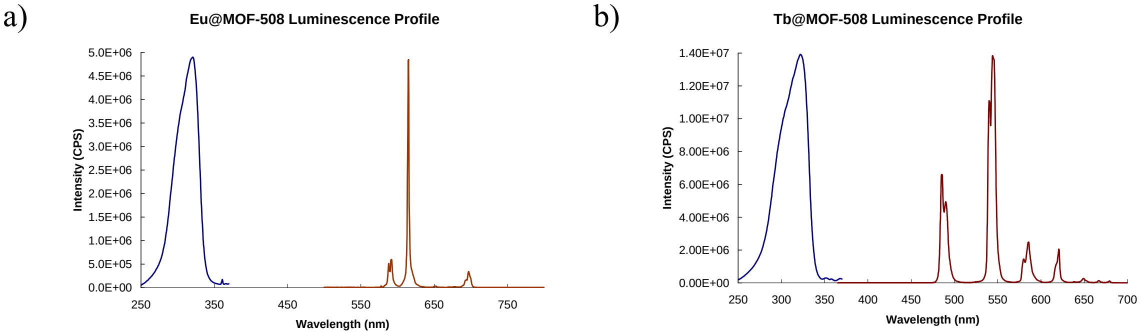

Figure 2.14: Solid-state luminescence spectra of a) Eu@MOF-508 and b) Tb@MOF-508. The excitation spectra show the greatest emission-producing absorption occurs by the organic framework of MOF-508, after which there is an energy transfer to the infiltrated lanthanoid to produce the red and green emissions of Eu and Tb respectively.

Attempts to generate a blue-emissive material in this fashion were also performed. However, trials with rare earth metals which have literature precedence for blue light emission such as Ce(III) and Dy(III) showed either low loading or ineffective sensitization of the metal luminescence. Thus in order to generate a blue light emitting material with similar framework properties as the Ln@MOF-508 series, an analog of MOF-508 in which the terephthalate linker is replaced by 2,6-naphthalene dicarboxylate was prepared dubbed MOF-508n.[6] Figure **2.15** shows an image of the three materials under UV irradiation showing strong blue, green, and red emission. We have investigated the materials' usefulness as sensors for gaseous analytes such as VOCs, and have achieved promising results.

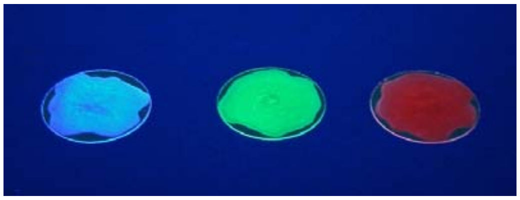

Figure 2.15: Image of MOF-508n (left), Tb@MOF-508 (center), and Eu@MOF-508 (right) drop cast in a PVA film on a glass slide. The materials are irradiated with a handheld UV lamp at 254 nm.

References:

1. M. Müller, S. Hermes, K. Kähler, M. W. E. van den Berg, M. Muhler and R. A. Fischer, *Chem. Mater*, 2008, **20**, 4576-4587.
2. F. Schröder, D. Esken, M. Cokoja, M. W. E. van den Berg, O. I. Lebedev, G. Van Tendeloo, B. Walaszek, G. Buntkowsky, H. H. Limbach, B. Chaudret and R. A. Fischer, *J. Am. Chem. Soc*, 2008, **130**, 6119-6130.
3. S. Hermes, M. Schroter, R. Schmid, L. Khodeir, M. Muhler, A. Tissler, R. W. Fischer and R. A. Fischer, *Angew. Chem. Int. Ed. Engl.*, 2005, **44**, 6237.
4. S. Hermes, F. Schröder, S. Amirjalayer, R. Schmid and R. A. Fischer, *J. Mater. Chem.*, 2006, **16**, 2464-2472.
5. N. Sabbatini, M. Guardigli and J.-M. Lehn, *Coord. Chem. Rev.*, 1993, **123**, 201-228.
6. B. Q. Ma, K. L. Mulfort and J. T. Hupp, *Angew. Chem., Int. Ed*, 2004, **43**, 2684.

3. Scintillating MOFs[2]

The detection and identification of subatomic particles is an important scientific problem with implications for medical devices, radiography, biochemical analysis, particle physics, and astrophysics. In addition, the development of efficient detectors of neutrons generated by fissile material is a pressing need for nuclear nonproliferation efforts. A critical objective in the field of radiation detection is to obtain the physical insight necessary for rational design of scintillation materials. Many factors affect the quantum efficiency and timing of scintillator light output, including chemical composition, electronic structure, inter-chromophore interactions, crystal symmetry, and atomic density. None of the material types currently used in radiation detection, which include crystalline inorganic compounds such as $LaBr_3$:Ce, organic compounds, and plastics, have the inherent synthetic versatility to exert systematic control over these factors. Therefore, it is likely that major advances in radiation detection will require the development of new materials outside the scope of traditional scintillators. Here, we propose that metal-organic frameworks (MOFs) could potentially offer the desired level of structural control, leading to an entirely new class of radiation detection materials.

MOFs are crystalline materials consisting of metal clusters linked by coordinating organic groups. Yaghi, O'Keefe, and coworkers have shown that structures resulting from the self assembly of specific metal ions and linkers can be predicted through an understanding of the geometric nets accessible to particular metal-linker combinations ("reticular chemistry")[1-3] which is difficult to accomplish in other extended crystalline materials such as zeolites and molecular solids. Furthermore, variation of the organic component of MOFs allows for additional structural modifications that can be used to tailor MOF properties. Conjugated organic molecules, which are usually fluorescent and are often scintillators as well, are used extensively as linkers in MOFs and reports of fluorescent MOFs are increasing[4-9] The relatively rigid structure of some MOFs can create permanent nanoporosity, a property being explored for gas storage,[10-15] separations,[13, 16] catalysis,[13, 17-20] and sensing.[21-23] This feature could also be advantageous in scintillation materials, enabling MOFs to serve as hosts for wavelength shifters or elements designed to improve the detection cross section (e.g., lithium or boron to improve sensitivity to thermal neutrons). Thus, compared with known scintillation materials, MOFs present an exceptional opportunity to perform "crystal engineering," creating the potential for rational design of new scintillation materials.

We recently reported the synthesis of two new MOFs containing fluorescent linkers that provide a starting point for the rational design of MOF-based scintillators.[5] Taking advantage of the crystalline nature of MOFs, we selected stilbene dicarboxylic acid ($SDCH_2$) as the precursor to the deprotonated dicarboxylate linker (SDC), anticipating that its constrained orientation within the MOF lattice would inhibit the non-radiative cis-trans isomerization pathway. The metal ion in both cases is Zn(II), as its d^{10} configuration results in the absence of optical transitions in the near UV-visible region of the spectrum, which reduces the fluorescence and emission spectra to transitions originating with the linker. One of these MOFs is a nanoporous structure consisting of interpenetrated $Zn_4O(SDC)_3$ subunits with the same three-dimensional topology as the isoreticular MOF (IRMOF) series, reported by Yaghi, et. al.[24, 25]

---

[2] This section is taken from F. P. Doty, C. A. Bauer, A. J. Skulan, P. G. Grant, M. D. Allendorf "Scintillating Metal Organic Frameworks: A New Class of Radiation Detection Materials," in press, *Adv. Mater.* August 2008.

(hereafter referred to as MOF-S1, in which “S” indicates “scintillator”). The second MOF is a nonporous material consisting of two-dimensional sheets of $Zn_3(SDC)_3(DMF)_2$ (DMF=N,N-dimethylformamide) (MOF-S2). In both cases, our strategy successfully led to increased fluorescence lifetimes that are indicative of higher fluorescence quantum efficiency from the rigidified stilbene linkers.

In this paper we describe spectroscopic measurements using single crystals of MOF-S1 and MOF-S2 demonstrating that they respond to ionizing radiation by emitting light, creating the first completely new class of scintillation materials since the advent of plastic scintillators in 1950.[26]This opens a new route to the development of high-performance scintillators with properties tailored to the detection of specific particle types and applications. These MOFs have scintillation quantum yields comparable to commercial organic scintillators and are also exceptionally resistant to radiation damage. Importantly, the spectroscopy shows that the differences in the radioluminescence of these two materials can be understood in terms of their crystal structure, which determines the extent of inter-chromophore coupling. In addition, unlike pure stilbene scintillators, the radioluminescence of MOF crystals differs from their standard steady-state fluorescence emission as a result of their framework structure. Since the synthetic flexibility of MOFs enables both the crystalline and electronic structure to be systematically varied, our investigations suggest that MOFs can serve as a controlled “nanolaboratory” for probing a broad range of photophysical phenomena.

To characterize the luminescence of these two MOFs in response to ionizing radiation, we exposed them to both high-energy (3 MeV) protons from an ion microprobe and a source of alpha particles. The proton beam simulates the production of recoil protons produced by elastic scattering of fast neutrons within an organic scintillator, leading to radioluminescence. To probe the interaction with protons, we used ion-beam-induced luminescence (IBIL) spectroscopy **(Figure 3.1)**,[27] a spectroscopic technique in which the luminescence is collected by an optical fiber, dispersed in a monochromator, and detected using a CCD. IBIL has been used to characterize defect structures in materials,[28] polymer-film degradation,[29] and radiation-induced damage.[30] For comparison purposes, we obtained the IBIL spectrum of anthracene crystals, the brightest known organic scintillator[31]] and used this as a standard to determine the relative light output of our materials. An advantage of Sandia’s microprobe is the ability to focus the beam, which allows the crystal to be imaged in scanning transmission ion microscopy (STIM) mode with 1 μm resolution. This method uses proton energy loss to obtain images of sample area and areal density, enabling the IBIL luminosity, and thus scintillation quantum yield, to be determined.

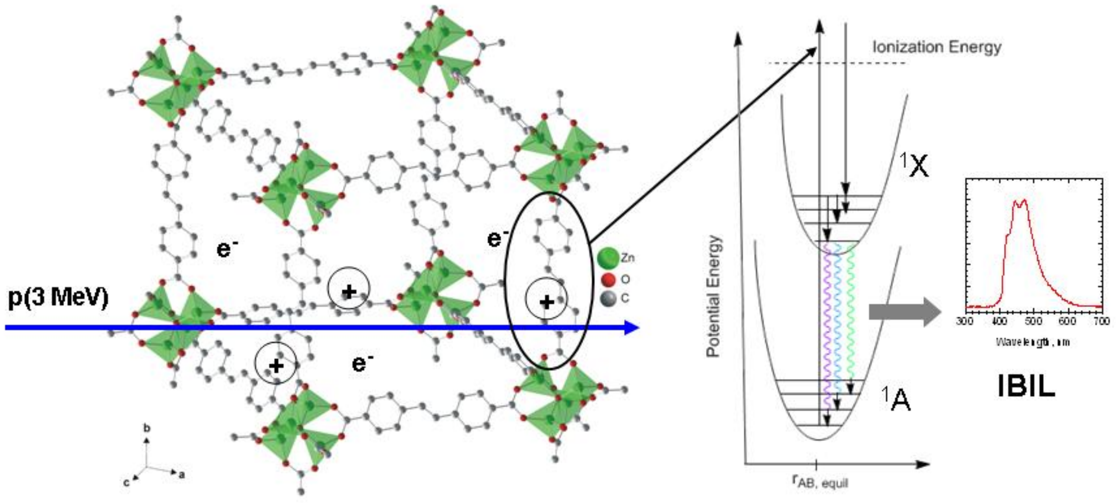

Figure 3.1. Schematic of the IBIL process (using a portion of the MOF-S1 structure for illustration), showing (left) the interaction of a high-energy proton that ionizes the material. The resulting excitation decays (right) through radiationless pathways (solid arrows) to the lowest-lying singlet excited state of the fluorescent SDC groups, which then decay by emission of photons (wavy arrows) to various ground-state vibrational levels, producing the IBIL luminescence displaying vibronic structure.

Single-crystal IBIL measurements demonstrate that the two stilbene-based MOFs exhibit proton-induced luminescence signatures that reflect the local environment of the organic fluorophore. IBIL spectra of $SDCH_2$ and both MOFs are shown in **Figure 3.2.** For comparison, this figure also shows the corresponding fluorescence excitation and emission spectra, which we previously reported.[5] The MOF fluorescence spectra are clearly different from that of the aggregated linker powder (Figure 3.2A). The IBIL spectra of the MOFs (Figures 3.2B and 3.2C) lie in approximately the same wavelength region (between 380 nm and 650 nm) as $SDCH_2$, which has maximum at 468 nm and is considerably narrower than the IBIL spectra of either MOF (full width at half maximum of 2601 cm^{-1} for $SDCH_2$ vs. 4680 cm^{-1} for MOF-S1 and 4400 cm^{-1} for MOF-S2, respectively). The intensities of the vibronic bands also vary considerably among the three materials. Pronounced structure is evident in the IBIL of MOF-S2, with distinct maxima visible at ~392 nm, 421 nm, 446 nm, and 472 nm. In contrast, the MOF-S1 IBIL spectrum is much less resolved (maximum at 472 nm with shoulders at 435 nm and 560 nm). These results show that the IBIL is a product of the MOF crystals only and not of any $SDCH_2$ impurities from synthesis (verified by elemental analysis) or a result of damage caused by the beam.

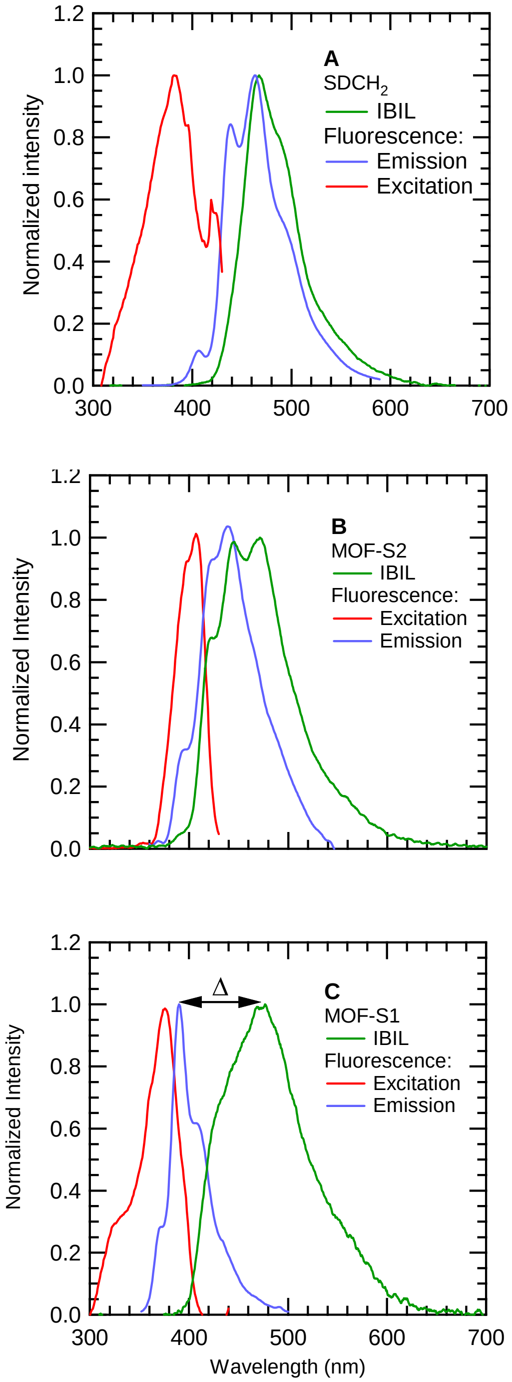

Figure 3.2. Comparison of IBIL spectra with fluorescence excitation and emission spectra (Ref. [24]) for the $SDCH_2$ linker, MOF-S1, and MOF-S2.

Table 3.1. Comparison of MOF light output with known organic scintillators, normalized for crystal volume and incident beam intensity.

Sample	Sample Mass	Dose rate[c]	Intensity[d]	% Anthracene
Anthracene[a]	0.4 μg	1.20×10^4	1.13×10^9	100
3D MOF[a] (crystal 1)	0.22 μg	1.00×10^4	9.62×10^7	9.0
2D MOF[a]	0.38 μg	9.33×10^3	2.49×10^8	22
Stilbene[b]				50
Commercial plastic and organic scintillators				11 – 80[b]

[a] IBIL data, this study. [b] Ref. [32]. [c] J kg^{-1} s^{-1}). [d] Counts J^{-1} at λ_{max} for the IBIL intensity.

The luminosity of both MOFs is comparable to commercial organic scintillators, whose light output is 10 – 80% of the anthracene standard (Table 3.1).[31] Luminosity was quantified by comparing the MOF IBIL intensity with that obtained from an anthracene crystal measured under identical conditions. Spectra were acquired after determining the crystal volume using STIM, which enables the dose rate to be computed from the beam current density. The relative luminosity was calculated from the counts in the peak channel normalized to the proton energy dissipated for each spectrum. The dense MOF-S2 emits with intensity 22% of anthracene, while the porous MOF-S1 is somewhat weaker (9.0% of anthracene). This result appears to correlate with the extent of π overlap in the structure, which increases in the order MOF-S1 < MOF-S2 < $SDCH_2$, as indicated by the estimated magnitude of the fluorescence Stokes shift.[5] Crystalline stilbene itself emits with an intensity 50% of anthracene and has displaced cofacial aromatic rings separated by as little as 3.5 Å[32] , indicating an even higher level of interchromophore interaction than in both the MOFs, neither of which have close cofacial interactions. The closest distances between SDC groups in MOF-S2 are 5.6 Å between ring centroids, with a 79° dihedral angle within an individual layer, and 6.0 Å with a 0° dihedral angle between layers. In MOF-S1, the shortest stilbene-stilbene distance is 5.6Å between ring centroids with a 49° dihedral angle between ring centroids.

From the perspective of practical scintillator use, the apparent Stokes shifts are quite large for both MOFs, as seen in Fig. 3.2. The IBIL of MOF-S2 and MOF-S1 are shifted 3415 cm^{-1} and 5620 cm^{-1}, respectively, relative to their respective fluorescence excitation maxima, which is sufficiently large that minimal overlap exists between the optical absorption and the IBIL emission (almost none in the case of MOF-S1). These large shifts favor their use in radiation detection, since self absorption should be minimal, allowing light to escape from a detector with a long optical path length. We note, however, that these apparent shifts may not reveal the full extent of self absorption, which may be greater for IBIL than fluorescence because typical measurements of the latter probe near-surface emitters, while IBIL probes emitters throughout the bulk of the material. Unfortunately, the small size of the MOF crystals does not permit us to measure single-crystal absorption spectra, which could be used to determine self absorption more accurately.

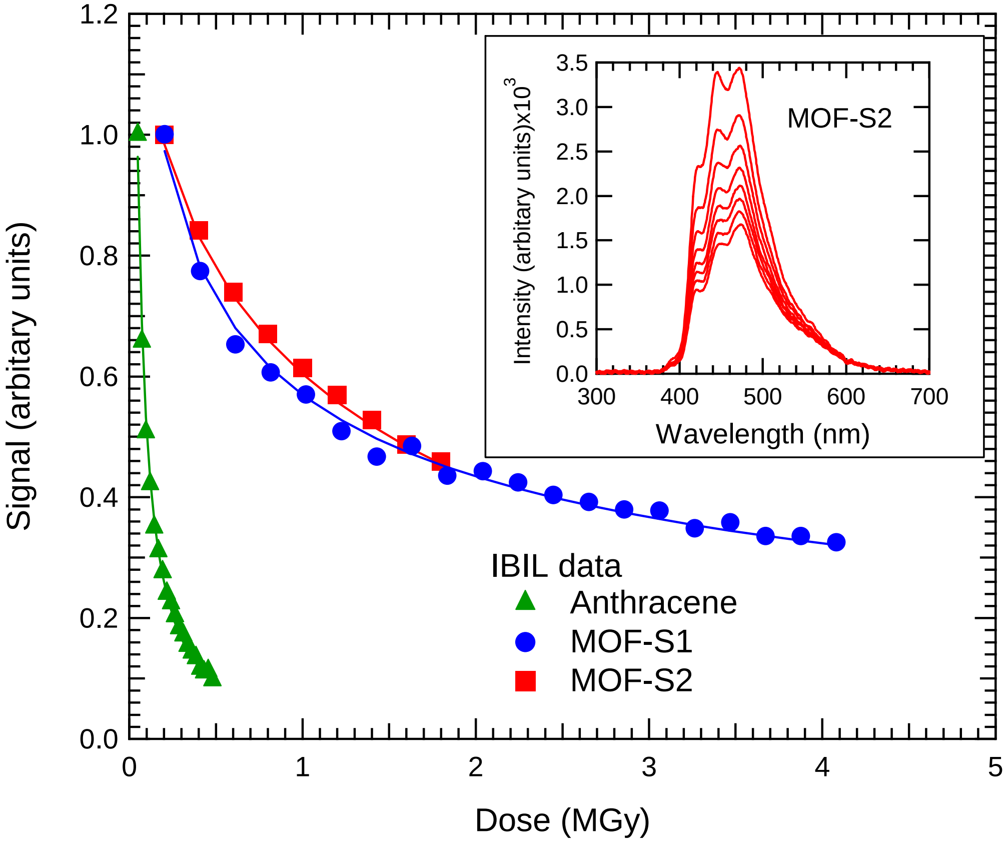

Figure 3.3. Decay of IBIL signal as a function of dose, comparing the stilbene MOF compounds with anthracene. Solid lines are fits of the maximum IBIL intensity (anthracene: 421 nm; MOF-S2: 473 nm; MOF-S1: 479 nm) to a stretched exponential function. Inset: Proton ion beam-induced luminescence spectra for MOF-S2, obtained using a continuous 3 MeV diffuse proton beam apertured to give 5 Mrad/s dose rate for thin samples. Spectra were taken at 2 s intervals, with the most intense spectrum obtained first.

Time-dependent IBIL data demonstrate that these MOFs are extremely resistant to radiation damage. The intensity of the IBIL emission of both MOFs decays uniformly with dose. This degradation is illustrated by in the inset of **Figure 3.3,** which shows a series of IBIL spectra taken from MOF-S2 at 2 s intervals and acquired during high current-density (100 nA cm-^{2}) experiments. No new bands appear, indicating that the damage mechanism does not produce new fluorescent species. This shows that the broad IBIL spectrum of MOF-S1 in Fig. 3.2 is not due to radiation damage, since the entire spectrum decreases uniformly with dose. In contrast, the appearance of a new IBIL band during proton irradiation of a plastic scintillator has been attributed to formation of radicals that are the precursors of crosslinking.[31] By pinning the ligands to the metal centers via strong carboxylate coordination, the formation of photoproducts (which often require isomerization of stilbene) and cycloadditions are avoided, both which are known to decrease the brightness and stability of stilbene. SEM, optical, and STIM images of both MOFs before and after exposure to the vacuum in the IBIL chamber and the proton beam reveal no evidence of physical damage. The decrease in the peak channel intensity is plotted in Figure 3.3 versus radiation dose for the MOFs and anthracene standard. It is noteworthy that the anthracene standard degrades significantly faster than either MOF. The decay rates of the two MOFs are similar and can be fit to a stretched exponential decay (Eqn. 1),[34] which is commonly used to describe the decay of scintillation light as a function of dose:

$$I = \exp(-d/D_0)^{\beta} \qquad (1)$$

The fits to the data are shown in Fig. 3.3; the decay constants are: D_0 = 2.303 MGy, β = 0.396 for MOF-S1; D_0 = 1.871 MGy, β = 0.434 for MOF-S2; and 2.044 x 10^{-5} MGy, β = 0.187 for anthracene. These novel materials can therefore withstand radiation doses far in excess of those expected in service and should be stable virtually indefinitely.

The fluorescence and IBIL spectra create a window into the local environment of the chromophore and the effects of ionizing radiation on these materials. Importantly, the spectra presented here do not conform to the commonly held mechanism for radiation-induced luminescence in organic scintillators. In this mechanism, the deposition of energy within the material creates singlet and triplet excitons. The singlets relax nonradiatively to the lowest excited singlet state, while the triplets may diffuse together and annihilate to produce additional singlets.[32] In both cases, the spectrum of the emitted light should be very similar to the fluorescence, since it occurs from the same excited state, although the time constants are quite different for the two paths to the ground state. The IBIL and fluorescence emission spectra of $SDCH_2$ are consistent with this mechanism, as is evident in Figure 3.2A.

In contrast, the IBIL and fluorescence of MOF-S1 hardly overlap at all (Figure 3.2C), with the IBIL shifted by an amount $\Delta = \sim 4450$ cm^{-1} (84 nm) to the red and into the wavelength region of the $SDCH_2$ IBIL and fluorescence emission. This large shift suggests that excitation of the material by the incident proton beam distorts the chromophore environment in MOF-S1 so that it becomes more like that of $SDCH_2$ in its crystalline state in terms of the amount of π overlap. The IBIL spectrum of MOF-S2 appears to be an intermediate case (Figure 3.2B); the IBIL spectrum is broader than the fluorescence, making Δ difficult to determine precisely, but is on the order of 410 cm^{-1}.

Although we can only speculate regarding the details of this distortion, two possibilities suggest themselves based on previous experiments and theory. First, the broad, unstructured shape of the MOF-S1 IBIL spectrum is similar to the fluorescence spectrum of cis-stilbene in solution [33], which is also red shifted relative to the fluorescence of trans-stilbene, [34] suggesting that partial rotation about the linker C=C bond may be occurring. A second possibility is that the dihedral angle between neighboring SDC linkers is decreasing, such that they more closely resemble a cofacial dimer pair. This may be possible because MOF-S1 has an interpentetrated structure. Through-space interactions in cofacial dimers can lead to both loss of vibronic structure (reminiscent of excimer formation) and a substantial red shift of the fluorescence emission. For example, the fluorescence of 4,16-distyryl[2.2]paracyclophane, in which two trans-stilbene molecules are joined by ethyl bridges that lock one benzene ring in each trans-stilbene into a cofacial orientation with the other, is red-shifted by ~ 5300 cm^{-1} from t-stilbene.[35] The magnitude of this shift is very similar to Δ for MOF-S1. Similarly, thia-bridged stilbenophane exhibits an unstructured and strongly red-shifted emission spectrum.[38] Based on the magnitude of Δ, the amount of distortion induced by the beam increases in the order $SDCH_2$ < MOF-S2 < MOF-S1. Analysis of the IBIL and fluorescence vibronic progressions, which reflect the ground-state vibrational structure, suggests that a change in the excited state is responsible for the differences between the fluorescence and IBIL spectra. We fitted the Franck-Condon structure of the fluorescence and IBIL spectra of both MOFs with a Gaussian line shape for each vibronic band, assuming a constant value for the vibrational frequency and allowing the line widths to vary. Using this approach we obtain a vibrational frequency of 1994 cm^{-1} for the MOF progressions and 1202 cm^{-1} for $SDCH_2$, a difference that is within the uncertainty of our fitting procedure. Although the $SDCH_2$ vibrational spectrum has not been assigned, both frequencies are similar to an intense band in the Raman spectrum of trans-stilbene that is assigned to the totally symmetric C(ethenyl)-C(phenyl) stretch. [36] We computed the normal modes of trans-stilbene and $SDCH_2$ using density functional theory (B3LYP exchange correlation functional) [37] and find that frequency differences between comparable modes in these two molecules are less than 10 cm^{-1} for most bands, supporting our assignment. This analysis indicates that the ground state of both MOFs is vibrationally similar to SDCH$_2$, leading us to conclude that a change in the MOF-S1 excited-state geometry and/or local chromophore environment is responsible for the apparent red shift in the IBIL of this MOF. This conclusion is consistent with ab initio calculations predicting that an excited-state distortion in thia-bridged silbenophane enables low-frequency interchromophore breathing modes to couple effectively with the electronic transition, leading to loss of vibronic structure in the emission spectrum. [38]

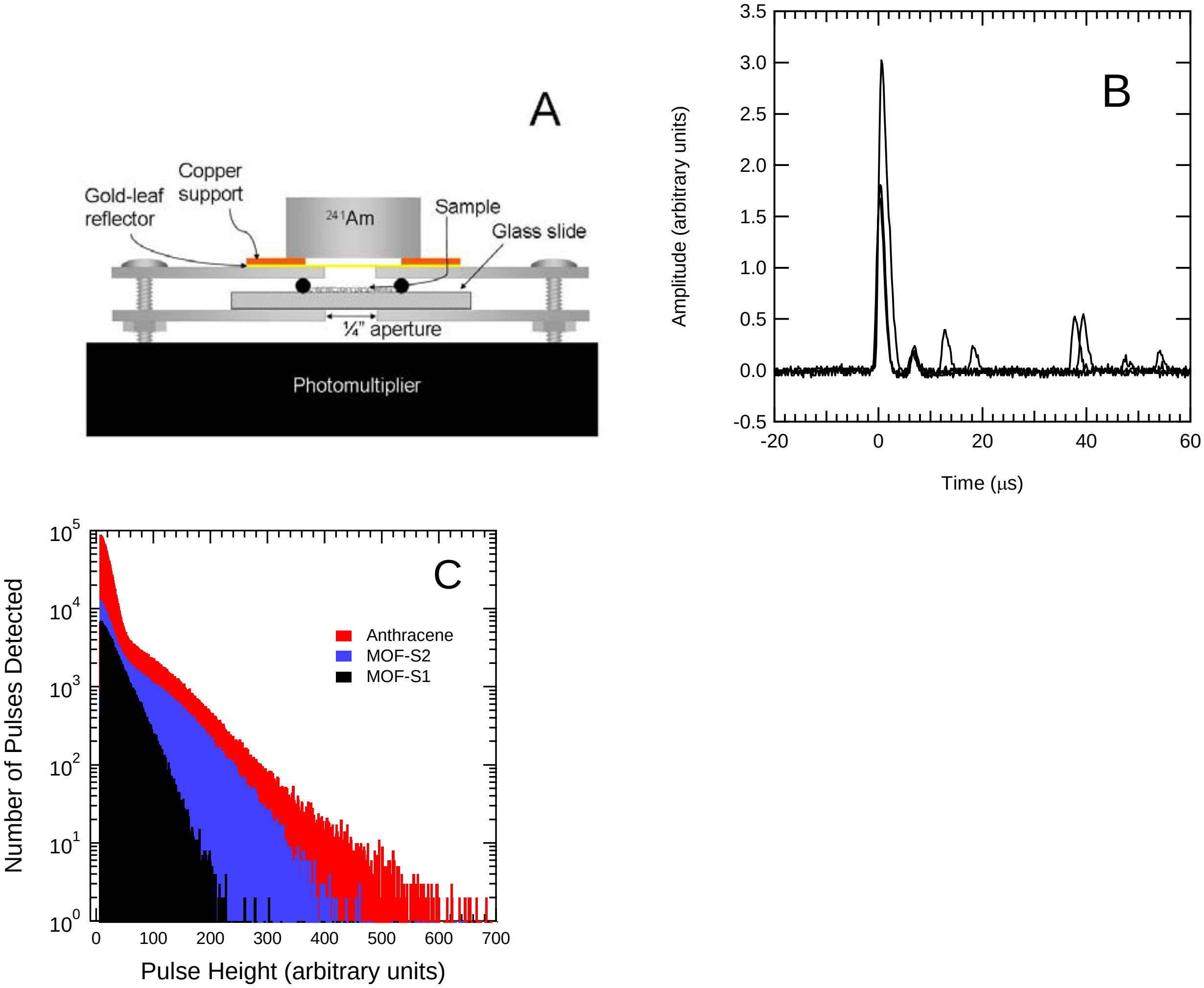

Figure 3.4. (A) Schematic of experiment used to measure scintillation light output. Pulses were detected with 2 μs shaping time (B), typical oscilloscope traces showing primary pulses at time zero and smaller delayed pulses at various times following the primary pulse, and (C) histogram of scintillation data for anthracene, MOF-S2, and MOF-S1.

The time dependence of scintillation pulses obtained in experiments with alpha particles **(Figure 3.4A)** provides additional evidence that both the linker electronic structure and its local environment within the crystal play key roles in determining the light output and its dynamics. The example in Figure 3.4B for MOF-S2 shows that light emission on two distinct time scales is produced by alpha radiation. Initially, an intense pulse is detected with a short (< 1 μs) excited-state lifetime, followed by many smaller delayed pulses at much longer times (>> 1 μs), as seen in the histogram in Figure 3.4C. An explanation for these long time-constant events is the recombination of triplet excitons, as proposed by Birks.[39] These data suggest that the time dependence of the luminescence can be varied by changing the chromophore environment via the MOF crystal structure.

The results described above demonstrate that control over both the electronic structure and local environment of a chromophore are possible in MOFs. This effectively creates a nanolaboratory for the systematic study of a broad range of photophysical phenomena, including scintillation, fluorescence, and energy transfer. Unlike either organic scintillators in solution or the pure materials themselves in their crystalline state, MOF synthetic flexibility allows both the crystal structure and the local electronic structure to be tuned. The two MOFs described here exemplify this concept and open the way to greatly enhanced understanding of photophysical phenomena and practical development of improved, more versatile scintillators.

Experimental

Sample preparation. Crystals of the 2D and 3D MOFs were synthesized using published procedures.[5] Single crystals of each material were mounted on Mylar or gold foils, or on graphite meshes, by placing a drop of a chloroform solution containing crystals and allowing the solvent to evaporate under N_2 atmosphere. In addition, crystals of the stilbenedicarboxylic acid linker (Alfa Aesar) and of anthracene (Aldrich, scintillation grade) were mounted in a similar fashion. Crystal integrity was verified before and after IBIL measurements (discussed below) by optical and/or scanning electron microscopy.

IBIL measurements. The Sandia National Laboratories nuclear microprobe employs a National Electrostatics Corporation Pelletron high voltage generator to produce 3 MeV protons used in the IBIL and STIM experiments. Nuclear microprobe analysis is well suited for characterizing small material samples due to its ability to quantify the sample and substrate areas and the areal density using STIM, and then excite the sample to produce optical emission that can be detected during sample-beam interactions.[40] STIM measures the areal density (mass within an area: ug/cm^2) of the sample and the substrate by measuring the energy lost from the focused incident beam as it traverses the sample.[41] STIM is essentially non-destructive, since the current densities required are very low. IBIL spectra were acquired with an Avantes thermoelectrically cooled detector with a spectral range of 180 to 1100 nm. The radioluminescence was collected with a 1 mm diameter fiber optic cable placed within 3 mm of the sample at 45° from the proton beam axis, and optically aligned to within ~ 150μm. Typical current densities in these measurements were 100 nA cm^{-2}.

Alpha particle measurements. The configuration used to detect the scintillation output of the MOFs in response to alpha-particle radiation is shown in Figure 4A. An ^{241}Am source (3389 Bq; Eckert & Ziegler Isotope Products, Valencia, CA) was located above a distribution of MOF particles on a glass slide. A gold-leaf foil was inserted between the source and the particles to reflect upwardly scattered light onto the photomultiplier (Acton Research photon counting module, model PD473), located below the sample. The sample and photomultiplier were enclosed within a housing purged with dry nitrogen to prevent degradation of the 3D MOF by atmospheric water. Individual pulse data were stored and analyzed using a digital oscilloscope (Lecroy Waverunner 6500, 500 MHz), and pulse height spectra were acquired with an Ortec multichannel analyzer and software. Scintillation light was collected for 65 minutes using an Ortec 142A charge-sensitive preamplifier and a shaping amplifier (Canbera 2020) with the shaping time set to 2 μs. Background spectra acquired for equal time with the source over an empty cell were subtracted from the spectra acquired from the MOF samples.

Computational Methods

Structures and vibrational spectra of $SDCH_2$ and trans-stilbene were predicted at the DFT-B3LYP level of theory, using the 6-31G(d) Gaussian basis set. All calculations were performed using the Gaussian 03 package [37].

References

[11] M. Dinca, A. Dailly, Y. Liu, C. M. Brown, D. A. Neumann, J. R. Long, *J. Am. Chem. Soc.* **2006**, *128*, 16876.
[12] T. Duren, l. Sarkisov, O. M. Yaghi, R. Q. Snurr, *Langmuir* **2004**, *20*, 2683.
[13] U. Mueller, M. Schubert, F. Teich, H. Puetter, K. Schierle-Arndt, J. Pastre, *J. Mater. Chem.* **2006**, *16*, 626.
[14] J. L. C. Rowsell, O. M. Yaghi, *Angew. Chem. Int. Ed.* **2005**, *44*, 4670.
[15] B. Xiao, P. S. Wheatley, X. B. Zhao, A. J. Fletcher, S. Fox, A. G. Rossi, I. L. Megson, S. Bordiga, L. Regli, K. M. Thomas, R. E. Morris, *J. Am. Chem. Soc.* **2007**, *129*, 1203.
[16] R. Q. Snurr, J. T. Hupp, S. T. Nguyen, *AIChE J.* **2004**, *50*, 1090.
[17] L. Alaerts, E. Seguin, H. Poelman, F. Thibault-Starzyk, P. A. Jacobs, D. E. De Vos, *Chem. Eur. J.* **2006**, *12*, 7353.
[18] S. H. Cho, B. Q. Ma, S. T. Nguyen, J. T. Hupp, T. E. Albrecht-Schmitt, *Chem. Comm.* **2006**, 2563.
[19] S. Hasegawa, S. Horike, R. Matsuda, S. Furukawa, K. Mochizuki, Y. Kinoshita, S. Kitagawa, *J. Am. Chem. Soc.* **2007**, *129*, 2607.
[20] K. C. Szeto, C. Prestipino, C. Lamberti, A. Zecchina, S. Bordiga, M. Bjorgen, M. Tilset, K. P. Lillerud, *Chem. Mater.* **2007**, *19*, 211.
[21] B. D. Chandler, D. T. Cramb, G. K. H. Shimizu, *J. Am. Chem. Soc.* **2006**, *128*, 10403.
[22] X. D. Guo, G. S. Zhu, Z. Y. Li, F. X. Sun, Z. H. Yang, S. L. Qiu, *Chem. Comm.* **2006**, 3172.
[23] S. Winter, E. Weber, L. Eriksson, I. Csoregh, *New J. Chem.* **2006**, *30*, 1808. [24] M. Eddaoudi, J. Kim, N. Rosi, D. Vodak, J. Wachter, M. O'Keefe, O. M. Yaghi, *Science* **2002**, *295*, 469.
[25] H. Li, M. Eddaoudi, M. O'Keeffe, O. M. Yaghi, *Nature* **1999**, *402*, 276.
[26] M. G. Schorr, F. L. Torney, *Phys. Rev.* **1950**, *80*, 474.
[27] J. R. Huddle, P. G. Grant, A. R. Ludington, R. L. Foster, *Nucl. Inst. Meth. Phys. Res. B* **2007**, *261*, 475.
[28] R. J. Brooks, D. E. Hole, P. D. Townsend, *Nucl. Instr. & Meth. Phys. Res. B* **2002**, *190*, 136.
[29] A. Quaranta, A. Vomiero, S. Carturan, G. Maggioni, G. Della Mea, *Nucl. Instr. & Meth. Phys. Res. B* **2002**, *191*, 680.
[30] A. Quaranta, *Nucl. Instr. & Meth. Phys. Res. B* **2005**, *240*, 117.
[31] G. F. Knoll, *Radiation Detection and Measurement*, Wiley, New York **2000**.
[32] C. J. Finder, M. G. Newton, N. L. Allinger, *Acta Cryst.* **1974**, *B30*, 411.
[33] J. Saltiel, A. S. Waller, J. Sears, D.F. , *J. Am. Chem. Soc.* **1993**, *115*, 2453.
[34] R. H. Dyck, D. S. McClure, *J. Chem. Phys.* **1962**, *36*, 2326.
[35] G. C. Bazan, J. Oldham, W.J., R. J. Lachicotte, S. Tretiak, V. Chernyak, S. Mukamel, *J. Am. Chem. Soc.* **1998**, *120*, 9188.
[36] Z. Meić, H. Güsten, *Spectrochim. Acta* **1978**, *34A*, 101.
[37] M. J. T. Frisch, G. W.; Schlegel, H. B.; Scuseria, G. E.;, M. A. C. Robb, J. R.; Montgomery, J. A., Jr.; Vreven, T.; Kudin,, J. C. M. K. N.; Burant, J. M.; Iyengar, S. S.; Tomasi, J.; Barone, V.;, B. C. Mennucci, M.; Scalmani, G.; Rega, N.; Petersson, G. A.;, H. H. Nakatsuji, M.; Ehara, M.; Toyota, K.; Fukuda, R.; Hasegawa, J.;, M. N. Ishida, T.; Honda, Y.; Kitao, O.; Nakai, H.; Klene, M.; Li,, J. E. H. X.; Knox, H. P.; Cross, J. B.; Bakken, V.; Adamo, C.;, J. G. Jaramillo, R.; Stratmann, R. E.; Yazyev, O.; Austin, A. J.;, R. P. Cammi, C.; Ochterski, J. W.; Ayala, P. Y.; Morokuma, K.;, G. A. S. Voth, P.;

Dannenberg, J. J.; Zakrzewski, V. G.; Dapprich,, A. D. S. S.; Daniels, M. C.; Farkas, O.; Malick, D. K.; Rabuck, A., K. F. D.; Raghavachari, J. B.; Ortiz, J. V.; Cui, Q.; Baboul, A., S. C. G.; Clifford, J.; Stefanov, B. B.; Liu, G.; Liashenko, A.;, P. K. Piskorz, I.; Martin, R. L.; Fox, D. J.; Keith, T.; Al-Laham,, C. Y. N. M. A.; Peng, A.; Challacombe, M.; Gill, P. M. W.;, B. C. Johnson, W.; Wong, M. W.; Gonzalez, C.; Pople, J. A. , Gaussian, Inc.: Wallingford, CT **2004**.

[38] J. Gierschner, H.-G. Mack, D. Oelkrug, I. Waldner, H. Rau‡, *J. Phys. Chem. A* **2004**, *108*, 257.

[39] J. B. Birks, *The Theory and Practice of Scintillation Counting*, Pergamon, Oxford **1964**.

[40] D. H. Morse, A. J. Antolak, G. S. Bench, D. W. Heikkinen, M. L. Roberts, E. Sideras-Haddad, *Nucl. Inst. Meth. Phys. Res. B* **1997**, *130*, 740.

[41] H. W. Lefevre, R. M. S. Schofield, J. C. Overley, J. C. McDonald, *Scan. Micro.* **1987**, *1*, 879.

4. Mechanical properties of IRMOF-1 metal-organic framework crystals[3]

Introduction

Metal organic frameworks (MOF), a novel subclass of crystalline coordination polymers, are hybrid inorganic-organic materials whose properties can be tuned by variation of both the metal and organic components.[1] A number of MOFs are nanoporous, exhibiting stable porosity that does not collapse when guest solvent molecules are removed. These materials, such as the isoreticular MOF series created by Yaghi et al.[2] and the MIL series of Férey et al.[3], include the highest surface-area crystalline compounds known. The combination of crystalline structure and tunable organic ligands enables the rational design of porosity at the nanoscale. As a result, there is growing interest in developing MOFs tailored for applications such as gas storage,[4] chemical separations,[5] catalysis,[6-8] drug delivery,[9] and sensors.[10, 11]

In many of these applications knowledge of the mechanical properties is important for designing MOFs with optimal properties. Specifically, the interface strength between a MOF layer and a substrate is a function of the elastic energy cost induced by a lattice or thermal expansion mismatch between MOF and substrate. Recently, several studies of the cubic zinc-carboxylate IRMOF-1 (formula unit Zn_4O(1,4-benzenedicarboxylate)$_3$; formerly designated MOF-5) appeared, in which density functional theory (DFT) was used to predict the single-crystal elastic constants (C_{11}, C_{12}, C_{44}; see Table 4.1). Mattesini et al. were the first to report these, employing the local density approximation (LDA) in a local orbital calculation (SIESTA).[12] Their results suggest that IRMOF-1 is a soft and ductile material, having a Young's modulus comparable to oak wood. Samanta et al.[13] used DFT-LDA with the more accurate projector augmented-wave (PAW) method in the VASP code, obtaining rather different results.[13] In particular, they find that the shear modulus C_{44} is small, indicating that this MOF is close to being structurally unstable. Finally, Zhou and Yildirim[14] report the calculated elastic and the calculated and measured vibrational properties of IRMOF-1. Again the calculations are performed within DFT-LDA with ultrasoft pseudopotentials.[14] They confirm the small C_{44} shear modulus of Samanta et al.[13] Their measured and calculated neutron inelastic scattering results largely agree, giving support to the reliability of the calculated elastic properties. The predicted lattice parameters are all close to, but slightly below, the experimental value obtained by neutron diffraction from deuterated IRMOF-1 at 3.5 K (25.91 Å).[15] This is typical for LDA calculations.

To provide data for comparison with theory we performed nanoindentation measurements on IRMOF-1 single crystals. Load versus displacement curves obtained from these measurements yield the stiffness, reduced modulus (which can be related to the Young's modulus), and hardness of the material. Two different nanoindentation techniques were used: a continuous stiffness measurement (CSM) technique and quasi-static indentation employing the Oliver-Pharr analysis method.[16] These techniques are found to yield consistent results in over 30 measurements on five different crystals. The measurements provide a mean value of the Young's modulus for comparison with DFT calculations.

---

[3] This section is taken from D. F. Bahr, J. A. Reid, W. M. Mook, C. A. Bauer, R. Stumpf, A. J. Skulan, N. R. Moody, B. A. Simmons, M. M. Shindel, M. D. Allendorf "Mechanical properties of IRMOF-1 metal-organic framework crystals," Phys. Rev. B, 76(2007), 184106.

Our DFT calculations are well-converged and we use both LDA and the generalized gradient approximation (GGA). To compare these two approximations makes sense because this provides a fundamental error margin for theory. Often the mean between LDA and GGA gives the most reliable results, exemplified by the fact that experimental lattice constants and bulk moduli are quite often bracketed by the LDA and GGA values. To eliminate further numerical issues we derive the bulk modulus (B_0) and elastic constants (C_{11}, C_{12}, and C_{44}) from the calculated stress tensor at a single, small strain. The combined theory and indentation results, coupled with the previously reported DFT calculations, enable for the first time a comparison of predicted mechanical properties with measurements. As will be seen, a substantial discrepancy is observed, the reasons for which are discussed below.

Experimental Methods

IRMOF1 single crystals were prepared using a method similar to that reported by Yaghi, et. al.[2] Briefly, 67 mg of 1,4-benzenedicarboxylic acid (99+%, ACROS Organics, Belgium) and 357 mg of $Zn(NO_3)_2{\cdot}6H_2O$ (Fluka; ≥ 99%) were dissolved in 10 mL of *N,N'*-diethylformamide (DEF; TCI America) in a pyrex bottle and sealed. This was heated for 16 hours at 105°C, after which the solvent was decanted. The crystals were washed twice with 10mL of fresh *N,N*'-dimethylformamide (DMF; Alfa Aesar). The solvents were exchanged with 10 mL of chloroform three times, allowing the crystals to soak for 24 hours with each exchange. The last solvent wash was decanted, leaving crystals slightly wet with chloroform. A portion of the crystals was stored in chloroform until testing, at which point they were mounted for nanoindentation and allowed to dry in ambient environment. Another portion was dried from chloroform under slowly decreasing pressure to a final pressure of 20 mTorr and periodically purged with dry nitrogen, as we noted sensitivity of the evacuated crystals to prolonged exposure to ambient air and rapid evacuation of the solvent. These crystals were dried for approximately 30 minutes and kept under dry nitrogen until ready for measurement.

Two different nanoindentation techniques[16] were used and found to yield consistent results. The first is the continuous stiffness measurement (CSM) technique preformed on an MTS Nano Indenter XP (MTS Corp., Eden Prairie, Minnesota). Here, the stiffness of the IRMOF-1 single crystal is measured throughout the displacement-controlled indentation process by the superposition of a 2-nm sinusoidal displacement on the tip at a frequency of 45 Hz. By evaluating stiffness in this manner, both hardness and reduced modulus can be determined continuously if the tip-sample contact area as a function of displacement is known. The area function of the Berkovich tip used here was determined by indenting a reference material, in this case fused quartz, with known elastic properties. All tests using the CSM technique were conducted on crystals at room temperature and at ambient relative humidity within one hour of the drying process described above. During indentation they were translucent, but then deteriorated within a few hours to an opaque appearance.

A second set of tests were performed on the crystals using quasi-static indentation employing the Oliver-Pharr analysis method.[16] These samples were stored in chloroform prior to testing. After removal from the chloroform, samples were adhered to a sample holder using cyanoacrylic adhesive. The habit planes of a given IRMOF crystal were oriented such that an external face would align perpendicular to the indenter direction. Using a Hysitron (Minneapolis, MN) Triboscope coupled with a Park Scientific (Santa Barbara, California) Autoprobe CP scanning probe microscope, IRMOF crystals were imaged using a constant force imagining technique with a diamond Berkovich indenter tip. After selecting a relatively flat region of the crystal, indentations were made using a quasi-static indentation at loading and unloading rates of approximately 10 μN/s. The stepped nature of the habit planes of these materials is shown in Fig. 4.1, as well as the resulting impression formed from a quasi-static indentation. There are large scale (tens of nm high) steps and pits on the surface. However, relatively flat regions, on the order of 1-5 μm across, can be identified using scanning probe microscopy and the indentations were carried out in these areas. Selecting these flat regions of the crystals for testing greatly enhanced the reproducibility of the nanoindentation experiments. An analysis of the unloading slope was used to determine the modulus and hardness of the samples. Five different crystals were selected for testing. Most tests were carried out within 30 minutes of mounting the samples and exposure to ambient environmental conditions. One set of samples was re-tested after four hours and six days of exposure to ambient atmospheric conditions.

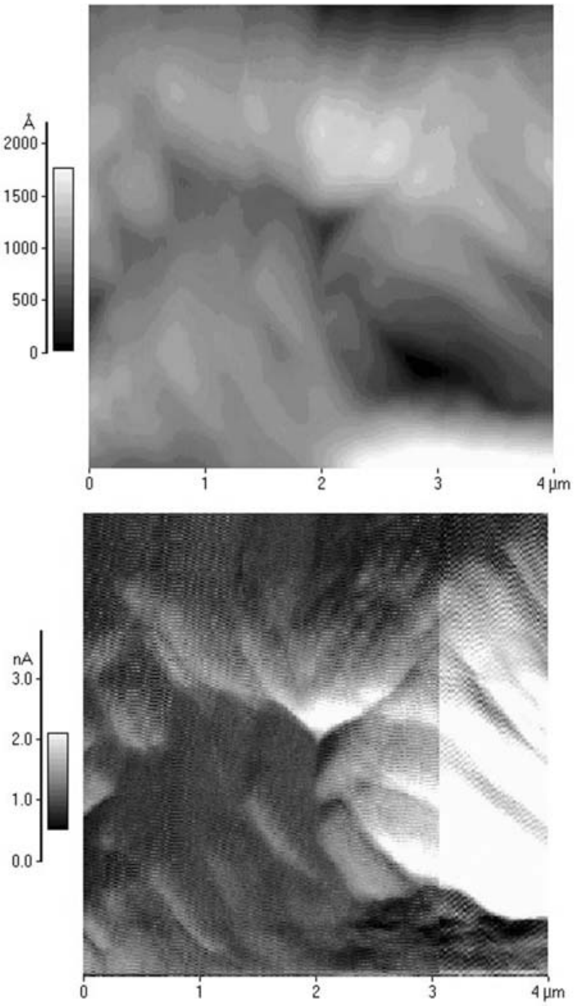

Fig. 4.1. Scanning probe microscopy height (top) and deflection (bottom) images of a residual impression on the habit planes of the IRMOF-1 crystals. Step heights of 10 – 100 nm separated by hundreds of nm were present on the surface, along with larger steps (1-10 μm) separated laterally by tens of μm.

Theoretical Methods

We performed DFT calculations using the VASP code[17, 18] and applied GGA[19] and LDA[20] to obtain an estimate of the fundamental reliability of our results. To accurately represent the atomic cores we use the projector augmented wave technique (PAW).[21] Electronic wave functions are represented by plane waves up to 400 eV, with tests up to 520 eV. Bulk calculations were performed in the rhombohedral, 106-atom, primitive cell, and the cubic, 424-atom, conventional cell. *K*-space sampling is sufficient with the Γ-point only as tests with up to 4 special *k*-points show. In all calculations atomic positions were relaxed with residual forces below 3 meV/Å. The typical procedure used to obtain the bulk modulus and elastic constants is to calculate a range of energies as a function of applied strain (or lattice constant), which are then fit to a Birch-Murnaghan[22] or similar equation of state.[23] This approach is unreliable here, because the total energy as a function of strain is not smooth enough, especially within 1% of the equilibrium lattice constant. To eliminate these numerical issues, we derive the bulk modulus (B_0) and elastic constants (C_{11}, C_{12}, and C_{44}) from the change of the directly calculated stress tensor at a single, small strain of 0.5%.

Results

A. DFT Calculations

Our LDA results are fairly close to those of Zhou et al.[14] and Samanta et al.[13] (see Table 4.1). This confirms the small value for the shear modulus C_{44}, which indicates a near instability of the IRMOF-1 structure. As usual, GGA predicts a larger lattice constant, resulting in mostly softer elastic constants. The exception is C_{44}, which is double that predicted by LDA. Table 4.1 also provides the LDA-GGA averages with a confidence interval based on the LDA-GGA difference and the numerical uncertainty. We obtain the Young's modulus *E* and Poisson's ratio ν from Equations (1) and (2) for cubic single crystals:

$$E = \frac{(C_{11} + 2C_{12})(C_{11} - C_{12})}{C_{11} + C_{12}} \qquad (1)$$

$$\nu = \frac{C_{12}}{(C_{11} + C_{12})} \qquad (2)$$

These equations yield 21.6 ± 0.3 GPa for *E* and 0.28 ± 0.01 for ν based on the average C_{11} and C_{12} values in Table 4.1. The modulus in a given orientation can be determined from[24]

$$\frac{1}{E} = S_{11} - 2\left(\left(S_{11} - S_{12}\right) - \frac{1}{2}S_{44}\right)\left(l^2m^2 + m^2n^2 + l^2n^2\right) \qquad (3)$$

where S is the compliance matrix (the inverse matrix described by the stiffness matrix in 4.1), and l,m,n are the direction cosines between the face of interest and the axis. For this material, we expect a range of moduli in different directions from 21.6 GPa in (100) to 7.5 GPa in (111).

TABLE 4.1. Summary of DFT predictions of IRMOF-1 elastic constants.

Source	**DFT**	**core**	**a$_{lat}$** Å	**density** g/cm^3	B_0 GPa	C_{11} GPa	C_{12} GPa	C_{44} GPa	E GPa	ν
This work	GGA	PAW	26.04	0.580	16.3	27.8	10.6	3.6	21.9	0.28
This work	LDA	PAW	25.59	0.611	17.6	28.5	12.1	1.7	21.3	0.30
This work	Average	PAW	25.8±.6	0.60±.03	17.0±.6	28.2±.4	11.4±.8	2.7±1	21.6	0.29
Mattesini 06	LDA	norm cons.	25.89	0.589	17.0	21.5	14.8	7.5	9.4	0.41
Samanta 06	LDA	PAW	25.64	0.607	18.5	29.2	13.1	1.4	21.1	0.31
Zhou 06	LDA	USP	25.58	0.611	18.2	29.4	12.6	1.2	21.9	0.30

Nanoindentation measurements

The residual impressions from the quasi-static indentations to contact depths of 200 nm are on the order of the size of the small terraces on the habit plane. The modulus and hardness as a function of depth obtained from the CSM measurements, shown in Fig. 2, go to larger contact depths and therefore sample many steps. The hardness and modulus values at depths less than 500 nm could be due to surface roughness effects that lead to inaccuracies in measurements,[25] while the values at greater depths are characteristic of this IRMOF-1 structure. Similar data have been collected from the quasi-static tests. The initial change in modulus and hardness in the quasi-static tests occurs over the first 100 nm of depth. When relatively flat areas are selected the modulus and hardness are essentially constant beyond 100 nm. The modulus measured by the quasi-static test shows a slightly higher value than that of the CSM tests, as shown in Fig. 3.

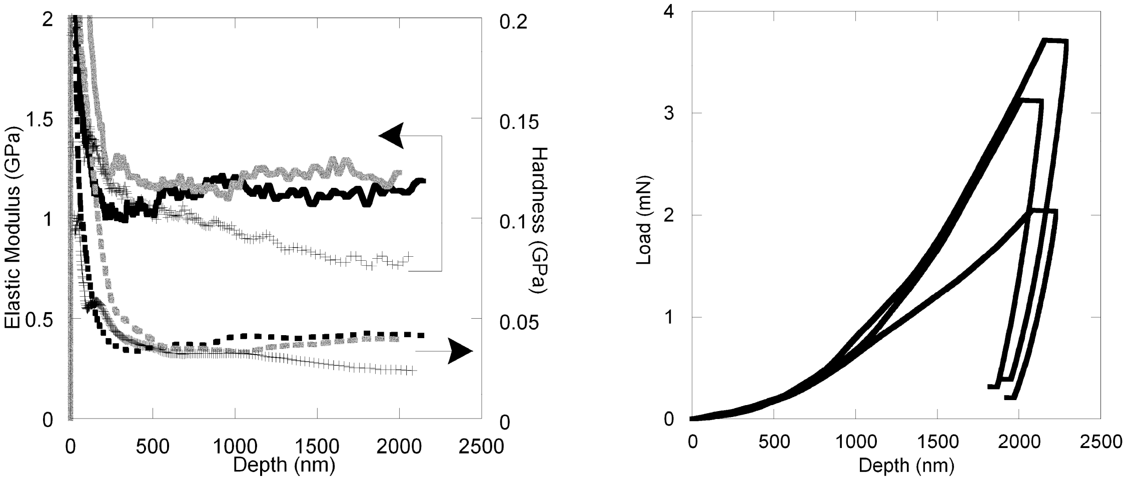

Fig. 4.2. Indentation of IRMOF-1 single crystals using continuous stiffness method (CSM) showing (top) load-displacement relation for three indents and (bottom) the elastic modulus (solid lines) and hardness (dotted lines) relations for the indents.

The mean reduced modulus obtained from 32 CSM tests in a crystal within one hour of mounting is 2.7 ± 1.0 GPa. The reduced modulus, E_b (shown in Fig. 3) is defined as

$$\frac{1}{E_r} = \frac{1-\nu_i^{\,2}}{E_i} + \frac{1-\nu_s^{\,2}}{E_s} \tag{4}$$

where E and ν are the Young's modulus and Poisson's ratio, respectively, and the subscripts i and s refer to indenter and sample respectively.

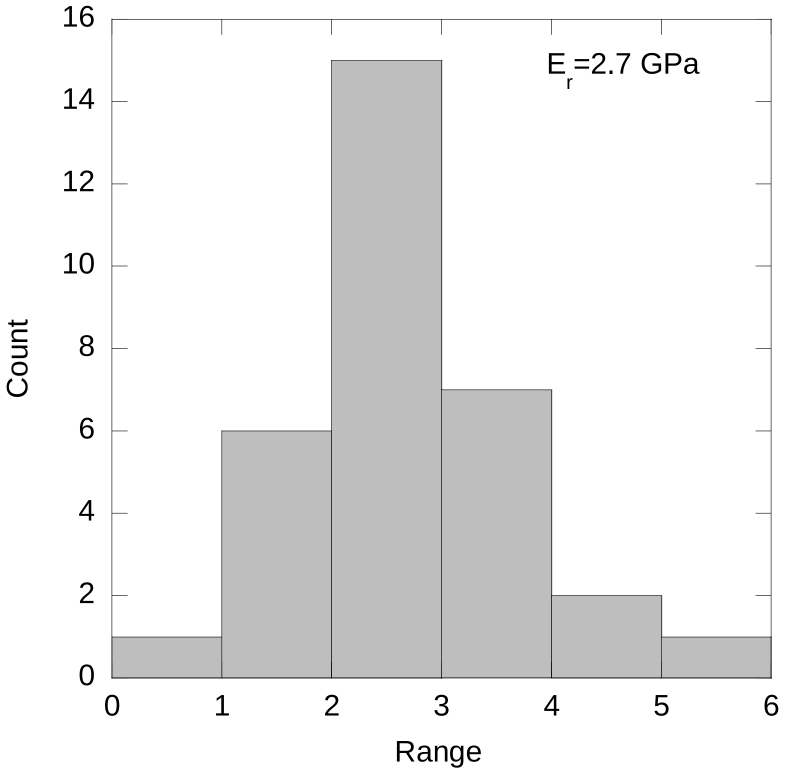

Fig. 4.3. Histogram of reduced elastic modulus of 32 quasistatic indentations in IRMOF-1 at depths between 150 and 500 nm using the Hysitron Triboscope. Both the modulus and hardness exhibit a normal distribution in values over this range of sampling volumes

For the conventional (quasi-static) indentation technique, diamond is selected for the indenter tip with E_i = 1149 GPa and v_i = 0.07. If one assumes our theoretical Poisson's ratio v_s of IRMOF-1 of 0.28, the Young's modulus E_s obtained from the quasi-static measurements is 2.5±1.0 GPa. The choice of v_s is not critical here. A change in v_s of 10% leads to at most 3% change in E_s. The average hardness from the quasi static measurements is 58 MPa, with a standard deviation of 26 MPa. This is 20% higher than the values measured by CSM. Typical quasi-static indentation tests are shown in Fig. 4.4, with two notable features. First, there is significant creep at the maximum load; this is also evident in the CSM tests. Second, there is adhesion between the tip and sample upon complete unloading, which manifests as a "pull off load" of approximately 6 μN in this particular experiment. Scanning probe imaging was carried out after typical indentations (Fig. 4.1) and revealed no fracture around these indentations, suggesting that the measured properties reported in this paper are not influenced by indentation-induced fracture. This is a unique observation, indicating that these materials deform under contact loading plastically, either by plastic flow or densification, rather than microscopic fracture. Plastic deformation is present at applied loads of 17 μN (which corresponds to an applied pressure of approximately 20 MPa) from the shallowest indentations performed in this study.

The mean reduced modulus obtained from 32 CSM tests in a crystal within one hour of mounting is 2.7 ± 1.0 GPa. The reduced modulus, E_b (shown in Fig. 4.3) is defined as

$$\frac{1}{E_r} = \frac{1-\nu_i^2}{E_i} + \frac{1-\nu_s^2}{E_s} \tag{4}$$

where E and ν are the Young's modulus and Poisson's ratio, respectively, and the subscripts i and s refer to indenter and sample respectively.

For the conventional (quasi-static) indentation technique, diamond is selected for the indenter tip with E_i = 1149 GPa and ν_i = 0.07. If one assumes our theoretical Poisson's ratio ν_s of IRMOF-1 of 0.28, the Young's modulus E_s obtained from the quasi-static measurements is 2.5±1.0 GPa. The choice of ν_s is not critical here. A change in ν_s of 10% leads to at most 3% change in E_s. The average hardness from the quasi static measurements is 58 MPa, with a standard deviation of 26 MPa. This is 20% higher than the values measured by CSM. Typical quasi-static indentation tests are shown in Fig. 4.4, with two notable features. First, there is significant creep at the maximum load; this is also evident in the CSM tests. Second, there is adhesion between the tip and sample upon complete unloading, which manifests as a "pull off load" of approximately 6 μN in this particular experiment. Scanning probe imaging was carried out after typical indentations (Fig. 4.1) and revealed no fracture around these indentations, suggesting that the measured properties reported in this paper are not influenced by indentation-induced fracture. This is a unique observation, indicating that these materials deform under contact loading plastically, either by plastic flow or densification, rather than microscopic fracture. Plastic deformation is present at applied loads of 17 μN (which corresponds to an applied pressure of approximately 20 MPa) from the shallowest indentations performed in this study.

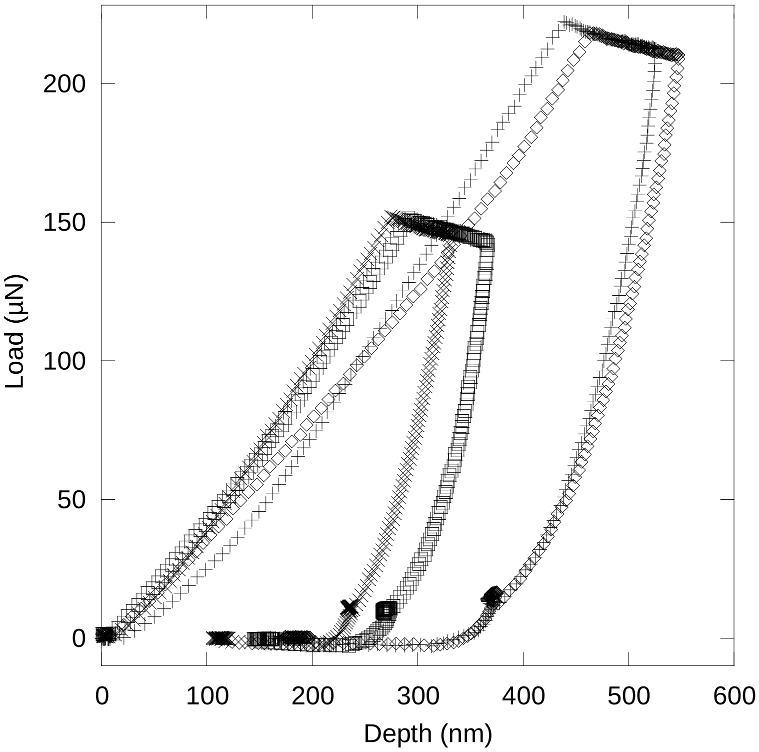

4.4. Typical quasi-static indentations of IRMOF-1 showing significant creep during a hold at maximum load and tip-sample adhesion (approximately 6 μN) upon retraction of the tip

Discussion

The Young's modulus obtained from the CSM nanoindentation measurements (2.7±1.0 GPa) is in significant disagreement with the average value of 21.6±0.3 GPa from DFT. However, as the IRMOF-1 is highly anisotropic in its elastic response, this must be accounted for when interpreting the experimental data. Based on the work of Vlassak and Nix,[26] it is possible to account for the elastic anisotropy using a correction factor to the indentation modulus. The anisotropy factor (E_{100}/E_{111}) is 2.88 for this material, and using the procedures described in Ref. 26 the correction factor to the modulus would be 0.34, such that the measured modulus is likely 2.94 times lower than the modulus in the (100) direction. With this correction factor, the estimated modulus from the indentation measurements is 7.9 GPa for (100) IRMOF-1. Therefore, the measured modulus is approximately one third of the calculated value.

Three aspects of the mechanical testing of the IRMOF-1 samples and the observed depth dependence of material properties may partially account for this difference: 1) surface roughness in the as-prepared samples; 2) air exposure during measurement; and 3) plastic deformation impacting elastic properties. As the IRMOF-1 crystals were tested in the as-grown condition, faceting and terraces on the growth surface are unavoidable. This leads to a surface roughness effect on the measured properties from contact, which can be minimized by selecting regions of surfaces that are free of macroscopic structural features such as pits. The facets themselves are sloped and not completely perpendicular to the indentation direction. These imperfections lead to scatter and systematic deviations in measured modulus and hardness. CSM measurements at optically selected regions can avoid the macroscopic (tens of μm) surface defects. The scanning probe methods avoid defects at the 0.1 μm level. Surface roughness leads to underestimation of modulus and hardness when using area functions that are calibrated from nominally flat materials. Thus, the results presented here may underestimate the actual values. An estimate can be made by comparing CSM measurements at rougher and quasi-static measurements at flatter regions. The flatter regions lead to about 20% higher hardness and 100% higher modulus values. Based on these tests we estimate that the modulus measured on a perfectly flat crystal would be at most 5 GPa higher than the estimated value of 7.9 GPa, which does not fully account for the difference between the DFT calculations and the measured value.

A second issue is that the IRMOF-1 crystals do alter their behavior with time during testing. Upon removal from chloroform the samples are optically clear. The chloroform evaporates over the span of a minute, with the crystals remaining optically clear. However, after approximately 1 hour of exposure to ambient atmosphere and mechanical testing the samples become opaque, with a whitish color. This transition occurs gradually. Two repeat measurements using quasi-static indentation made after 4 hours and after 6 days of exposure to atmosphere exhibit an elastic modulus decrease of approximately 20% compared with measurements made within one hour on the same specimen. If interactions between the atmosphere and the crystal are responsible for these changes in opacity, they may also impact the mechanical properties. Water vapor is known to degrade IRMOFs.[27, 28] Similarly, if there is residual solvent or other substances within the MOF pores that only slowly evaporate, this could impact mechanical properties. The modulus appears to decrease slowly with time, so it is possible that some of the difference between the DFT calculations and measured elastic modulus is due to the difficulty of determining the properties of these materials in a pristine condition. However, for the limited measurement times used here (four hours) the elastic properties are relatively constant after exposure to ambient conditions. In addition, crystals stored by two methods (in chloroform and evacuated and backfilled with nitrogen, as described in the Experimental Methods section) are found to give similar results, suggesting that the presence of residual solvent in the lattice does not affect the elastic properties.

The third, and probably most significant effect, is the inherent assumption in nanoindentation testing that the elastic properties are the same upon loading and unloading. Extracting properties from nanoindentation data traditionally relies upon the assumption that the loading behavior is both elastic and plastic, while the unloading behavior is commonly assumed to be a result of elastic deformation. At our lowest load indentations in this material (17 μN), there was permanent deformation after testing. Because of the extensive open structure in these crystals, the structure after permanent deformation may not be identical to the initial structure. An analogy would be the deformation of a buckled structure. It is well known that macroscopic beam structures that have buckled are more compliant than their initial state. Similarly, recent nanoindentation testing of vertically aligned carbon nanotube turf structures[29, 30] has shown that a buckled nanostructure can be orders of magnitude more compliant than in tension and in fact continue to exhibit a lower effective modulus upon continued compressive loading. The possible similarities with the IRMOF-1 structure suggest that the discrepancies between the theory and experiment could be a result of the inability to probe only elastic deformation in these structures, and that their deformation behavior is likely significantly different than that of other nanoporous materials such as gold, which exhibit an increase in modulus with densification.[31, 32] The hardness of the crystals was low enough that we were unable to separate any purely elastic load–displacement curves during nanoindentation. To reach lower strains, the conventional method in indentation is to increase the included contact angle of the indenter. For example, using a large spherical tip at low penetration depths will provide an extremely low effective strain.[33] However, due to the surface roughness of these materials, increasing the indenter tip radius is not a viable option, as the surface roughness will then dominate the initial contact behavior. The possible change in structure responsible for the permanent deformation could be viewed similarly to a phase transition in solids, where the unloading portion of the indentation is altered by the phase transformation under the indentation region.[36] Further work on characterizing this local structure could be enlightening, but is beyond the scope of the current study.

In general, the DFT methods used here perform well with regard to predicting the elastic and vibrational properties of solids and molecules. We are unaware of any significant failures, certainly not close to the factor 3 at issue here. DFT has been applied to surfaces and open structures, as well as novel materials such as nanocarbon structures.[34] Elastic properties are also usually well described, including materials at very high pressures within the earth's mantle,[35] and often scale with the lattice constant. Thus, the fact that our calculations correctly predict the IRMOF-1 lattice constant is significant and we therefore ascribe differences between theory and experiments primarily to the three experimental issues: surface roughness, atmospheric interactions, and plastic deformations.

Conclusions

The elastic and plastic response of the novel metal organic framework IRMOF-1 has been measured via nanoindentation and the results compared to elastic constants predicted by DFT. The Young’s modulus measured via CSM nanoindentation, approximately 2.7 GPa, is about an order of magnitude lower than that predicted by DFT. After accounting for the anisotropic elastic behavior, the measured value is still a factor of three lower than the predicted values. Surface roughness, which prevents measurements at small indentation from staying within the elastic limit of the IRMOF-1 crystal, is a factor in lowering the measured moduli. The sensitivity of these materials to atmospheric conditions may also be partially responsible for the differences between these values. Surprisingly, plasticity without fracture is observed during contact loading of these materials even at small (< 100nm) indentation amplitudes. This may be the most significant contribution to the lowering of the measured moduli and indicates that the differences between experimental and theoretical behavior cannot be ascribed to fracture processes in these macroscopically brittle materials. These results suggest that post-yield elastic properties, applied stresses, and subsequent deformation will need to be considerations for applications involving these materials and they will likely require inert atmospheres and low applied stresses to maintain their structural integrity.

References

[1] S. L. James, Chem. Soc. Rev. **32**, 276 (2003).

[2] M. Eddaoudi, J. Kim, N. Rosi, D. Vodak, J. Wachter, M. O'Keefe, and O. M. Yaghi, Science **295**, 469 (2002).

[3] G. Ferey, Chem. Mater. **13**, 3084 (2001).

[4] J. L. C. Rowsell and O. M. Yaghi, Angew. Chem. Int. Ed. **44**, 4670 (2005).

[5] R. Q. Snurr, J. T. Hupp, and S. T. Nguyen, AIChE J. **50**, 1090 (2004).

[6] S. Hermes, M.-K. Schroter, R. Schmid, L. Khodeir, M. Muhler, A. Tissler, R. W. Fischer, and R. A. Fischer, Angew. Chem. Int. Ed. **44**, 6237 (2005).

[7] P. Mahata, G. Madras, and S. Natarajan, J. Phys. Chem. B **110**, 13759 (2006).

[8] C.-D. Wu, A. Hu, L. Zhang, and W. Lin, J. Amer. Chem. Soc. **127**, 8940 (2005).

[9] P. Horcajada, C. Serre, M. Vallet-Regi, M. Sebban, F. Taulelle, and G. Ferey, Angew. Chem. Int. Ed. **45**, 5974 (2006).

[10] C. A. Bauer, T. V. Timofeeva, T. B. Settersten, B. D. Patterson, V. H. Liu, B. A. Simmons, and M. D. Allendorf, J. Amer. Chem. Soc. **129**, 7136 (2007).

[11] Z. Ni, J. P. Jerrell, K. R. Cadwallader, and R. I. Masel, *Anal. Chem.* in press. (2007).

[12] M. Mattesini, J. M. Soler, and F. Yndurain, Phys. Rev. B **73**, 094111 (2006).

[13] A. Samanta, T. Furuta, and J. Li, J. Chem. Phys. **125**, 084714 (2006).

[14] W. Zhou and T. Yildirim, Phys. Rev. B **74**, 180301 (2006).

[15] T. Yildirim and M. R. Hartman, Phys. Rev. Lett. **95**, 215504 (2005).

[16] W. C. Oliver and G. M. Pharr, J. Mat. Res. **19**, 3 (2004).

[17] G. Kresse and J. Furthmuller, Comput. Mat. Sci. **6**, 15 (1996).

[18] G. Kresse and J. Furthmuller, Phys. Rev. B **54**, 11169 (1996).

[19] Y. Wang and J. P. Perdew, Phys. Rev. B **44**, 13298 (1991).

[20] J. P. Perdew and A. Zunger, Phys. Rev. B **23**, 5048 (1981).

[21] P. R. B. P. E. Blochl, Phys. Rev. B **50**, 17953 (1994).

[22] F. D. Murnaghan, Proc. Nat. Acad. Sci. **30**, 244 (1944).

[23] P. Sodelerlind, O. Eriksson, J. M. Wills, and A. M. Boring, Phys. Rev. B **48**, 5844 (1993).

[24] G. E. Dieter, *Mechanical Metallurgy* (McGraw Hill, New York, 1986).

[25] M. S. Bobji and S. K. Biswas, J. Mat. Res. **14**, 2259 (1999).

[26] J. Vlassak and W. D. Nix, J. Mech. Phys. Sol. **42**, 1223 (1994).

[27] J. A. Greathouse and M. D. Allendorf, J. Amer. Chem. Soc. **128**, 10678 (2006).

[28] L. Huang, H. Wang, J. Chen, Z. Wang, J. Sun, D. Zhao, and Y. Yan, Micropor. Mesopor. Mat. **58**, 105 (2003).

[29] C. M. McCarter, R. F. Richards, S. Mesarovic, C. D. Richards, D. F. Bahr, D. McClain, and J. Jiao, J. Mater. Sci. **41**, 7872 (2006).

[30] S. D. Mesarovic, C. M. McCarter, D. F. Bahr, H. Radhakrishnan, R. F. Richards, C. D. Richards, D. McClain, and J. Jiao, Scripta Mater. **56**, 157 (2007).

[31] A. M. Hodge, J. Biener, J. R. Hayes, P. M. Bythrow, C. A. Volkert, and A. V. Hamza, Acta Mater. **55**, 1343 (2007).

[32] C. A. Volkert, E. T. Lilleodden, D. Kramer, and J. Weissmüller, Appl. Phys. Lett. **89**, 061920 (2006).

[33] D. Tabor, *The Hardness of Metals* (Oxford, Oxford, 1951).

[34] J. Bernholc, D. Brenner, M. B. Nardelli, V. Meunier, and C. Roland, An. Rev. Mat. Res. **32**, 347 (2002).

[35] B. B. Karki, L. Stixrude, and R. M. Wentzcovitch, Rev. Geophys. **39**, 507 (2001).

[36] V. Domnich, Y. Gogotsi, and S. Dub, Appl. Phys. Lett. **76**, 2214 (2000).

5. Force field modeling[4]

Force field description

Nonbonded parameters for the BDC linker atoms were adapted from the CVFF force field[1] with slight modifications. CVFF is a general purpose force field used primarily for organic molecules. Its transferability to a range of organic compounds makes it attractive for use in a general force field for MOFs. Nonbonded potential energy interactions E_{ij} between atoms i and j separated by a distance r were calculated according to

$$E_{ij} = \frac{q_i q_j}{r} + 4\varepsilon_{ij}\left[\left(\frac{\sigma_{ij}}{r}\right)^{12} - \left(\frac{\sigma_{ij}}{r}\right)^{6}\right] \qquad (1)$$

where $\sigma_{ij} = \sqrt{\sigma_i \sigma_j}$ and $\varepsilon_{ij} = \sqrt{\varepsilon_i \varepsilon_j}$ represent the van der Waals radius and energy well depth for the atomic pair. These parameters are given in Table 5.1. Intramolecular interactions (bond stretch, angle bend, dihedral angle, improper angle) for BDC atoms were also adapted from CVFF[1] with minor changes as summarized in Table 5.2. The force field includes no intramolecular interactions for Zn-O_{cent} and Zn-O_{carb} pairs. Instead, only nonbonded interactions (Equation 1) were used to allow for maximum flexibility on the Zn_4O tetrahedra. Parameters for IRMOF-1 were determined by manual fitting to obtain good agreement with published structural data for pure IRMOF-1 (i.e., without adsorbed guest molecules). Parameters for guest molecules were taken from CVFF[1] without modification and were treated with full flexibility. These parameters were not optimized for bulk liquid properties of these guest molecules. Geometric mixing rules were used to calculate host-guest van der Waals parameters.

---

[4] This section is compiled from the following publications:

Jeffery A. Greathouse, Tiffany L. Kinnibrugh, and Mark D. Allendorf "Adsorption and Separation of Noble Gases by IRMOF-1: Grand Canonical Monte Carlo Simulations," submitted to *Ind. Eng. Chem. Res.* August 2008.

Greathouse, JA; Allendorf, MD "Force field validation for molecular dynamics simulations of IRMOF-1 and other isoreticular zinc carboxylate coordination polymers," *J. Phys. Chem. C.* 112 (2008), 5795-5802.

Jeffery A. Greathouse and Mark D. Allendorf "Reactivity of metal-organic framework-5 with water studied by molecular dynamics simulations," J. Amer. Chem. Soc., 128 (2006), 10678

Table 5.1. Force Field Parameters (atomic charge *q* and Van der Waals parameters σ and ε for Nonbonded Interactions in IRMOF-1 and Guests.

atom type[a]	description	q (e)	σ (Å)	ε (kJ·mol^{-1})
Zn	zinc	1.200	2.3110	0.006
O_{cent}	inorganic oxygen	–1.200	3.0882	3.548
O_{carb}	carboxylate oxygen	–0.600	2.9861	3.548
C_{carb}	carboxylate carbon	0.600	3.6170	0.619
C_{phenyl}	phenyl carbon bonded to C_{carb}	0.000	3.6170	0.619
C_{phenyl}	phenyl carbon bonded to H	–0.100	3.6170	0.619
c3	methyl carbon	–0.300	3.8754	0.163
c2	sp^3 carbon bonded to 2 H atoms (ethanol)	–0.170	3.8754	0.163
c2	sp^3 carbon bonded to 2 H atoms (CH_2Cl_2)	0.252	3.8754	0.163
c2	sp^3 carbon bonded to 2 H atoms (C_6H_{12})	–0.200	3.8754	0.163
c1	sp^3 carbon bonded to 1 H atom ($CHCl_3$)	0.578	3.8754	0.163
c	sp^3 carbon bonded to 0 H atoms (CCl_4)	0.904	3.4745	0.669
oh	hydroxyl oxygen	–0.380	3.1655	0.650
cl	chlorine	–0.226	3.5349	0.289
ho	hydrogen bonded to O	0.350	0.0000	0.000
h	hydrogen bonded to C	0.100	2.4500	0.159

[a] Capitalized atom types refer to IRMOF-1 atoms, while lower case atom types refer to CVFF atom types.

Table 5.2. Intramolecular Force Field Parameters for IRMOF-1 and Guests.

Bond Stretching: $E_{\text{bond}} = k_1(r - r_0)^2$.

bond	k_1 (kJ·mol^{-1}·Å^{-2})	r_0 (Å)
C_{phenyl}–C_{phenyl}	2008.3	1.34
C_{phenyl}–h	1520.5	1.08
C_{phenyl}–C_{carb}	1469.6	1.40
C_{carb}–O_{carb}	2259.4	1.25
c3–c2	1350.2	1.526
h–c3	1425.1	1.105
c2–oh	1606.7	1.420
h–c2	1425.1	1.105
oh–ho	2317.7	1.000

Table 5.2 (cont.). Intramolecular Force Field Parameters for IRMOF-1 and Guests.

Angle Bending: $E_{\mathrm{angle}} = k_2(\theta - \theta_0)^2$.

angle	k_2 (kJ·mol^{-1}·rad^{-2})	θ (°)
C_{phenyl}–C_{phenyl}–C_{phenyl}	376.6	120.0
C_{phenyl}–C_{phenyl}–h	154.8	120.0
C_{phenyl}–C_{phenyl}–C_{carb}	145.1	120.0
C_{phenyl}–C_{carb}–O_{carb}	228.0	113.0
O_{carb}–C_{carb}–O_{carb}	606.7	135.0
h–c3–c2	185.8	110.0
h–c3–h	165.3	106.4
c3–c2–oh	292.9	109.5
h–c2–c3	185.8	110.0
h–c2–oh	238.5	109.5
h–c2–h	165.3	106.4
c2–oh–ho	244.8	106.0
c2-c2-c2	195.0	110.5
c2-c2-h	185.8	110.0

Table 5.2 (cont'd)

Dihedral Angle: $E_{\text{dihedral}} = k_3[1 + d\cos(n\phi)]$.

angle	k_3 (kJ·mol^{-1})	d	n
C_{phenyl}-C_{phenyl} -C_{phenyl} -C_{phenyl}	12.5520	–1	2
C_{phenyl}-C_{phenyl}-C_{phenyl}-C_{carb}	12.5520	–1	2
C_{phenyl}-C_{phenyl}-C_{phenyl}-h	12.5520	–1	2
C_{carb}-C_{phenyl}-C_{phenyl}-h	12.5520	–1	2
h-C_{phenyl}-C_{phenyl}-h	12.5520	–1	2
C_{phenyl}-C_{phenyl}-C_{carb}-O_{carb}	10.4900	–1	2
h-c3-c2-oh	0.6615	1	3
h-c3-c2-h	0.6615	1	3
c3-c2-oh-ho	0.5439	1	3
h-c2-oh-ho	0.5439	1	3
c2-c2-c2-c2	0.6615	1	3
c2-c2-c2-h	0.6615	1	3
h-c2-c2-h	0.6615	1	3

Improper Torsion: $E_{\text{improper}} = k_4[1 + d\cos(n\phi)]$.

angle	k_4 (kJ·mol^{-1})	d	n
C_{phenyl}-C_{phenyl}-C_{phenyl}-h	1.55	–1	2
C_{phenyl}-C_{phenyl}-C_{phenyl}-C_{carb}	41.84	–1	2
C_{phenyl}-C_{carb}-O_{carb}-O_{carb}	41.84	–1	2

Force field validation

Introduction

Metal organic frameworks (MOFs) are a diverse class of coordination polymers in which metal ions are connected to each other through bridging organic "linker" molecules that coordinate to the metal centers.[1,2] Although not microporous by definition, the MOFs attracting the most attention recently have relatively rigid, open-framework structures that allow them to maintain their porosity upon removal of solvent. The isoreticular series of zinc- and copper-based IRMOF (isoreticular metal-organic framework) compounds developed by Yaghi et al.[3] and the MIL compounds developed by Férey et al.[4,5] are of particular interest because of their potential for rational design of nanoporous materials, enabled by the inherent synthetic flexibility of the linker molecule. While the discovery of exceptional gas sorption properties by MOFs has been mostly adventitious, several recent attempts to rationally design their properties for specific applications, such as hydrogen[6-8] or methane[9] storage and CO_2 sequestration,[10] have been reported.

Although a seemingly vast array of possibilities for creating MOFs with specific properties would seem to exist, neither the properties resulting from the choice of a particular linker, nor the ability to synthesize a MOF from it can be considered a certainty. Thus, there is an important role for theoretical methods that can predict properties such as molecular diffusion and adsorption isotherms, enabling the most promising candidates to be identified prior to launching a potentially time-consuming synthetic effort. Atomistic methods, such as molecular dynamics and Monte Carlo techniques, are particularly attractive for this purpose, due to their ability to treat a wide variety of related chemical systems coupled with relatively high computational efficiency for large-scale systems.[11] The prototypical MOF compound in computational studies has been IRMOF-1 (also known as MOF-5), which consists of Zn_4O vertices connected by benzene dicarboxylate (BDC or terphthalate) linkers. To date, a number of studies have been reported, focusing on hydrogen,[12-17] methane,[16,18-20] CO_2,[16,21] hydrocarbons,[16,19,22] and inert gases.[16,23,24]

These previous investigations employed standard force fields to model the interaction between the MOF and molecules within its pores, such as the universal force field,[25] DREIDING force field,[26] and OPLS force field,[27] or by custom optimization of Lennard-Jones potentials.[22] In all cases, the atoms within the MOF were not allowed to move during the simulation. It is apparent, however, that MOFs are structurally flexible and can exhibit substantial changes in unit cell parameters upon adsorption or desorption of guest molecules.[28,29] For example, Cussen *et al.* present evidence for dynamic flexibility in a nickel-pyridine MOF that absorbs toluene even though its pore dimensions are too small to admit this molecule.[30] Fixed-atom force fields obviously cannot capture these effects. It also clear that the parameterization of these existing force fields are not always well-suited to the description of MOFs. In some cases allowing the empty framework to relax results in unreasonably short bond distances,[30] while in others diffusion constants are significantly overpredicted.[31]

One approach to these problems is the "flexible," but still fully bonded, force field developed by Schmid and coworkers,[31,32] who parameterized the MM3 force field to account for interactions with the Zn_4O clusters in IRMOF-1. This model successfully predicts the IRMOF-1 structure and yields vibrational frequencies in reasonable agreement with the predictions of density functional theory

(DFT).[32] It is also encouraging that the benzene self-diffusion constant obtained from MD calculations is within ~30% of the value measured by NMR.[31] More recently, another fully bonded flexible force field for IRMOF-1 was used to calculate phonon thermal conductivity and vibrational power spectra from molecular dynamics simulations.[33]

An additional limitation of fully bonded force fields, however, whether or not the atoms are fixed, is that they cannot be used to probe framework reactivity with respect to either adsorbates or solvent environments. To address this problem, as well as the need for structural flexibility, we recently reported a non-bonded force field for IRMOF-1 that reproduces the crystal structure of this compound.[34] Molecular dynamics (MD) simulations of the interaction of water with IRMOF-1 predict framework collapse above a critical water concentration, a result that is in qualitative agreement with experiment. Following our nonbonded approach, Dubbeldam *et al.*[35] used a combination of DREIDING[26] and CVFF[36] force fields for simulations of several Zn-based IRMOFs. Our force field model for IRMOF-1 was calibrated by comparison with experimental data as well as ab initio calculations of ZnO and correctly predicts the structure of IRMOF-1. Additionally, as we show below, our model correctly predicts the vibrational motion of ZnO_4 tetrahedra and 180° rotations of phenyl groups in IRMOF-1.

In this section, we present a detailed description and validation of this force field, including MD simulations of the temperature, pressure, and guest-molecule dependencies of the IRMOF-1 lattice parameter, comparisons with reported periodic DFT calculations of the framework total energy as a function of lattice size, vibrational frequencies obtained from atomic power spectra, and benzene diffusion at low loading. We also describe grand canonical Monte Carlo predictions of adsorption isotherms for several gases. The good agreement with the results of both experiments and first-principles theory establishes this model as the foundation for a generalized force field for zinc-carboxylate IRMOFs.

References

(1) James, S. L. *Chem. Soc. Rev.* **2003**, *32*, 276.
(2) Kitagawa, S.; Kitaura, R.; Noro, S. *Angew. Chem.* **2004**, *43*, 2334.
(3) Rowsell, J. L. C.; Yaghi, O. M. *Microporous and Mesoporous Materials* **2004**, *73*, 3.
(4) Férey, G.; Mellot-Draznieks, C.; Serre, C.; Millange, F.; Dutour, J.; Surble, S.; Margiolak, I. *Science* **2005**, *3093*, 2040.
(5) Surblé, S.; Serre, C.; Mellot-Draznieks, C.; Millange, F.; Férey, G. *Chem. Comm.* **2006**, 284.
(6) Rowsell, J. L. C.; Yaghi, O. M. *Angew. Chem.* **2005**, *44*, 4670.
(7) Dinca, M.; Han, W. S.; Liu, Y.; Dailly, A.; Brown, C. M.; Long, J. R. *Angewandte Chemie-International Edition* **2007**, *46*, 1419.
(8) Forster, P. M.; Eckert, J.; Heiken, B. D.; Parise, J. B.; Yoon, J. W.; Jhung, S. H.; Chang, J. S.; Cheetham, A. K. *Journal of the American Chemical Society* **2006**, *128*, 16846.
(9) Eddaoudi, M.; Kim, J.; Rosi, N.; Vodak, D.; Wachter, J.; O'Keefe, M.; Yaghi, O. M. *Science* **2002**, *295*, 469.
(10) Chen, B. L.; Ma, S. Q.; Zapata, F.; Fronczek, F. R.; Lobkovsky, E. B.; Zhou, H. C. *Inorg. Chem.* **2007**, *46*, 1233.
(11) Dubbeldam, D.; Snurr, R. Q. *Molecular Simulation* **2007**, *33*, 305.
(12) Garberoglio, G.; Skoulidas, A. I.; Johnson, J. K. *J. Phys. Chem. B* **2005**, *109*, 13094.
(13) Mueller, T.; Ceder, G. *J. Phys. Chem. B* **2005**, *109*, 17974.
(14) Mulder, F. M.; Dingemans, T. J.; Wagemaker, M.; Kearley, G. J. *Chem. Phys.* **2005**, *317*, 113.

(15) Sagara, T.; Klassen, J.; Ganz, E. *J. Chem. Phys.* **2004**, *121*, 12543.

(16) Skoulidas, A. I.; Sholl, D. S. *J. Phys. Chem. B* **2005**, *109*, 15760.

(17) Yang, Q.; Zhong, C. *J. Phys. Chem. B* **2005**, *109*, 11862.

(18) Düren, T.; Sarkisov, L.; Yaghi, O. M.; Snurr, R. Q. *Langmuir* **2004**, *20*, 2683.

(19) Düren, T.; Snurr, R. Q. *J. Phys. Chem. B* **2004**, *108*, 15703.

(20) Wang, S. *En. Fuels* **2007**, *21*, 953.

(21) Ramsahye, N. A.; Maurin, G.; Bourrelly, S.; Llewellyn, P.; Loiseau, T.; Ferey, G. *Physical Chemistry Chemical Physics* **2007**, *9*, 1059.

(22) Jiang, J. W.; Sandler, S. I. *Langmuir* **2006**, *22*, 5702.

(23) Krungleviciute, V.; Lask, K.; Heroux, L.; Migone, A. D.; Lee, J. Y.; Li, J.; Skoulidas, A. *Langmuir* **2007**, *23*, 3106.

(24) Skoulidas, A. I. *J. Amer. Chem. Soc.* **2004**, *126*, 1356.

(25) Rappe, A. K.; Casewit, C. J.; Colwell, K. S.; Goddard, W. A.; Skiff, W. M. *J. Amer. Chem. Soc.* **1992**, *114*, 10024.

(26) Mayo, S. L.; Olafson, B. D.; Goddard, W. A. *J. Phys. Chem.* **1990**, *94*, 8897.

(27) Jorgensen, W. L.; Maxwell, D. S.; Tirado-Rives, J. *J. Am. Chem. Soc.* **1996**, *118*, 11225.

(28) Fletcher, A. J.; Thomas, K. M.; Rosseinsky, M. J. *J. Sol. State Chem.* **178**, *178*, 2491.

(29) Uemura, K.; Matsuda, R.; Kitagawa, S. *J. Sol. State Chem.* **2005**, *178*, 2420.

(30) Cussen, E. J.; Claridge, J. B.; Rosseinsky, M. J.; Kepert, C. J. *J. Amer. Chem. Soc.* **2002**, *124*, 9574.

(31) Amirjalayer, S.; Tafipolsky, M.; Schmid, R. *Angewandte Chemie-International Edition* **2007**, *46*, 463.

(32) Tafipolsky, M.; Amirjalayer, S.; Schmid, R. *Journal of Computational Chemistry* **2007**, *28*, 1169.

(33) Huang, B. L.; McGaughey, A. J. H.; Kaviany, M. *International Journal of Heat and Mass Transfer* **2007**, *50*, 393.

(34) Greathouse, J. A.; Allendorf, M. D. *Journal of the American Chemical Society* **2006**, *128*, 10678.

(35) Dubbeldam, D.; Walton, K. S.; Ellis, D. E.; Snurr, R. Q. *Angewandte Chemie International Edition* **2007**, *46*, 4496.

(36) Dauber-Osguthorpe, P.; Roberts, V. A.; Osguthorpe, D. J.; Wolff, J.; Genest, M.; Hagler, A. T. *Proteins: Structure, Function, and Genetics* **1988**, *4*, 31.

Structural Validation and Mechanical Properties

MD simulations show that our non-bonded force field accurately predicts the IRMOF-1 structure as a function of temperature, in addition to achieving the observed room-temperature unit-cell dimensions. In particular, the unusual feature of negative thermal expansion is accurately reproduced (Fig. 5.1). As temperature is increased above 200 K, the simulated lattice parameter decreases. A linear regression indicates that the lattice parameter would be 25.74 Å at 0 K, in agreement with the DFT result of 26.09 Å.[2] Although the simulated lattice parameters are slightly lower (~ 0.2 Å) than the experimental values for evacuated IRMOF-1, the trend of negative thermal expansion is in good agreement with both experiment and other simulations.[3] Using linear regression to calculate lattice parameter values at 30 K and 293 K, we find an increase in unit cell volume of 1.0 %, in exact agreement with XRD results that show the same percentage increase in unit cell volume (≈ 200 $Å^3$ or 0.1 Å in lattice parameter) over the same temperature range.[4] Dubbeldam *et al.*[3] also reported similar agreement with experiment using their flexible force field. They also derived thermal-expansion coefficients from their simulations, concluding that IRMOFs outperform other contracting materials.

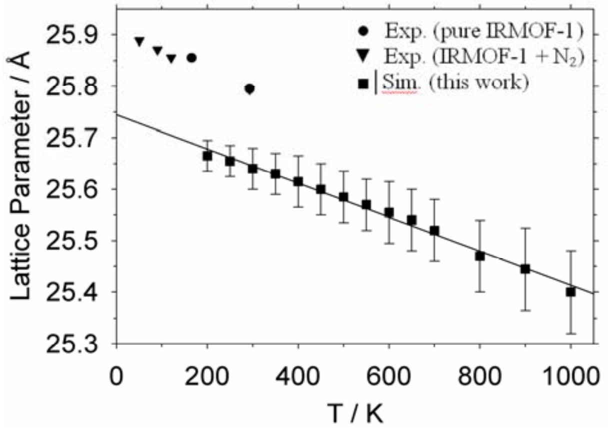

Figure 5.1. Temperature dependence of the simulated lattice parameter compared with experimental data.[4,5] Error bars indicate uncertainties in the simulated lattice parameters. The solid line represents a linear regression through the simulation results.

Predicted pressure-volume and energy-volume relationships are in good agreement with DFT calculations. These dependencies were examined by performing constant-volume MD simulations at 300 K, and force field energy minimizations which, like the DFT calculations, correspond to 0 K . In Figure 5.2 we show that the minimum in potential energy at 300 K is achieved when the lattice parameter is between 25.70 Å − 25.75 Å, but this value increases to 26.05 Å using energy minimization (0 K). These lattice parameters fall within the range of energy-minimized DFT values (25.58 Å – 26.04 Å),[6] and they agree with experimental XRD values.[7,8] The effect of negative thermal expansion is apparent in Figure 5.2, and also noteworthy is the effect of thermal motion on the energy profile (width and minimum-energy lattice parameter) at 300 K. This suggests a change in mechanical properties between 0 K and 300 K, which we explore below. The *PV* relationships predicted by our force field are compared with DFT results[6] in Figure 5.3. At 300 K, the lattice parameter (and volume) vary linearly with pressure over the range 25.6 Å – 26.0 Å. Further reductions in lattice parameter below 25.4 Å do not result in a continued increase in pressure, although the DFT and energy minimization results are linear at positive and negative pressures. At these reduced volumes (lattice parameter < 25.6 Å), the MD simulations predict a disordered structure and eventual collapse of the framework. To our knowledge, the stability of IRMOF-1 at these high pressures has not been investigated experimentally, but DFT calculations predict a low shear modulus which indicates that IRMOF-1 is close to structural instability.[6] The calculated slope from MD simulation at 300 K (−1.30 Å·GPa^{-1}) is nearly triple the value obtained from DFT calculations (–0.46 Å·GPa^{-1})[6] or the force field energy minimizations (–0.43 Å·GPa^{-1}). We have already seen that temperature effects control the structure of IRMOF-1, but these results demonstrate that temperature plays an important role in the mechanical properties as well.

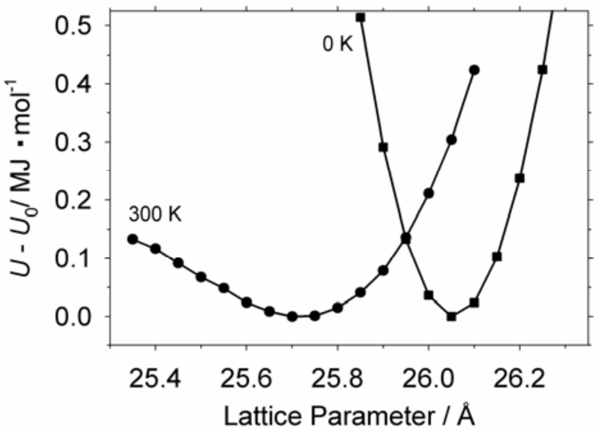

Figure 5.2. Average potential energy (U) relative to the equilibrium potential energy (U_0) versus lattice parameter from a series of *NVT* simulations at 300 K and energy minimizations (0 K).

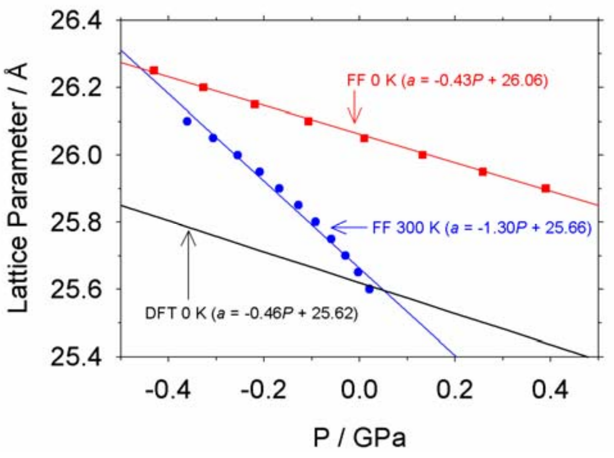

Figure 5.3. Pressure dependence of IRMOF-1 at 0 K and 300 K. Force field (FF) simulations from this work were calculated from a series of *NVT* simulations (300 K) and energy minimizations (0 K). Colored lines represent linear regressions of the FF simulation data, and the black line represents the linear regression from DFT calculations.[6]

The force field simulations enable us to calculate the bulk modulus (B_0) by fitting energy-volume results to an equation of state.[9] The corresponding figures are shown as Supporting Information, and the results are given in Table 5.3. The force field result at 0 K is in good agreement with DFT, which suggests that our nonbonded approach for modeling of IRMOF-1 accurately captures the structural and mechanical properties obtained from more expensive DFT calculations. The force field results at 300 K include thermal effects and represent an averaged structure, which results in a much lower bulk modulus than the 0 K results.

Table 5.3. Comparison of force field (FF) calculations of bulk modulus (B_0) and Young's modulus (E_0) with DFT calculations and nanoindentation experiments.

	Energy Min. (0 K)		**MD Sim. (300 K)**	**Experiment**
	FF (this work)	**DFT[10]**	**FF (this work)**	**(room temp)[10]**
B_0 (GPa)	20.0	16.3	4.0	
E_0 (GPa)	35.5	21.9	14.9	7.4

The large pore volumes of IRMOFs may make it difficult to obtain accurate energy-strain relationships. A more direct comparison with the nanoindentation experiments can be made by calculating the Young's modulus, E_0. Starting with the equilibrium (relaxed state), one lattice parameter is increased in small increments, and the potential energy is determined by *NVT* simulation (300 K) or energy minimization (0 K). The Young's modulus can then be determined as follows:[11]

$$\frac{\Delta U}{V_0} = E_0\left(\frac{1}{2}\varepsilon^2 + \frac{1}{3}A\varepsilon\right) \tag{2}$$

where $\Delta U = U - U_0$ is the difference in potential energy between the loaded (U) and relaxed (U_0) states, $\varepsilon = (l-l_0)/l$ is the load strain determined from the relaxed (l) and strained (l_0) lattice parameter, and A is a fitting parameter. The plot corresponding to Equation 2 is shown as Supporting Information. The force field predicts a higher Young's modulus at 0 K than the DFT result (21.9 GPa).[10] However, at room temperature we obtain E_0 = 14.9 GPa. An experimental value of E_0 (7.4 GPa) obtained from nanoindentation measurements is available for comparison.[10] In analyzing these data, the authors of ref 52 note that the IRMOF-1 crystals do not behave fully elastically, which may partially explain why their measured value is significantly lower than DFT predictions. The MD simulations of the E_0 temperature dependence suggest, however, that the agreement between DFT and experiment may actually be better than previously thought, since E_0 is predicted to decrease substantially at temperatures above 300 K. We conclude that our nonbonded, flexible force field approach successfully predicts the mechanical properties of IRMOF-1 based on the available theoretical and experimental results.

Energetic validation

We examined the vibrational motion of IRMOF-1 at 300 K as a stringent validation of the force field. Recently published experimental spectra of IRMOF-1[12-14] and analogous inorganic complexes provide a basis for comparison[15,16] In addition, there are two recently published spectra obtained from force field simulations.[17,18] Unlike our nonbonded approach, however, these force fields include bonded terms between all atoms, including Zn, O_{cent}, and O_{carb}.

We concentrate on the Zn-O interactions (200 cm^{-1} – 1000 cm^{-1}) as these are controlled only by nonbonded interactions. Vibrations associated with the BDC phenyl ring are primarily governed by the bond-stretch and angle-bend portions of the CVFF force field, which are used essentially unaltered in our force field. To obtain vibrational information from MD simulations we computed power spectra for Zn, O_{cent}, O_{carb}, and C_{carb} atoms, as shown in Figure 5.4 (top); frequencies are compared with computational and experimental results in Table 5.4. Peaks determined from a normal mode analysis[2,18] can usually be associated with specific vibrational modes, such as a symmetric Zn-O_{cent} stretch. This is not possible with power spectra, but vibrational modes can be tentatively assigned by examining the contributions from specific atom types.

Spectroscopic peaks between 530 cm^{-1} and 560 cm^{-1} are typically used to identify ZnO_4 vibrations,[15,16] and for IRMOF-1 the 534 cm^{-1} band in the infrared spectrum has been assigned to the Zn-O stretching vibration.[14] Our power spectra exhibit peaks in this region at 500 cm^{-1}, 550 cm^{-1}, and 575 cm^{-1} that involve Zn, O_{cent}, and O_{carb} atoms. Additional Zn- O_{cent} modes are found between 185 cm^{-1} and 280 cm^{-1}, in agreement with bonded force field methods.[18] Similar modes are observed experimentally near 340 cm^{-1} for a Zn-acetate complex.[15] At higher frequencies, several peaks are seen for O_{carb} and C_{carb} between 720 cm^{-1} and 815 cm^{-1} that involve Zn and O_{cent} atoms, but to a much smaller extent. These modes likely correspond to carboxylate bending, with minor involvement of the inorganic Zn and O_{cent} atoms. Infrared and Raman peaks in this region have been assigned to O-C-O scissoring motions and other modes.[19,20] We take this agreement to be strong confirming evidence that the non-bonded approach captures essential aspects of the forces governing MOF structure.

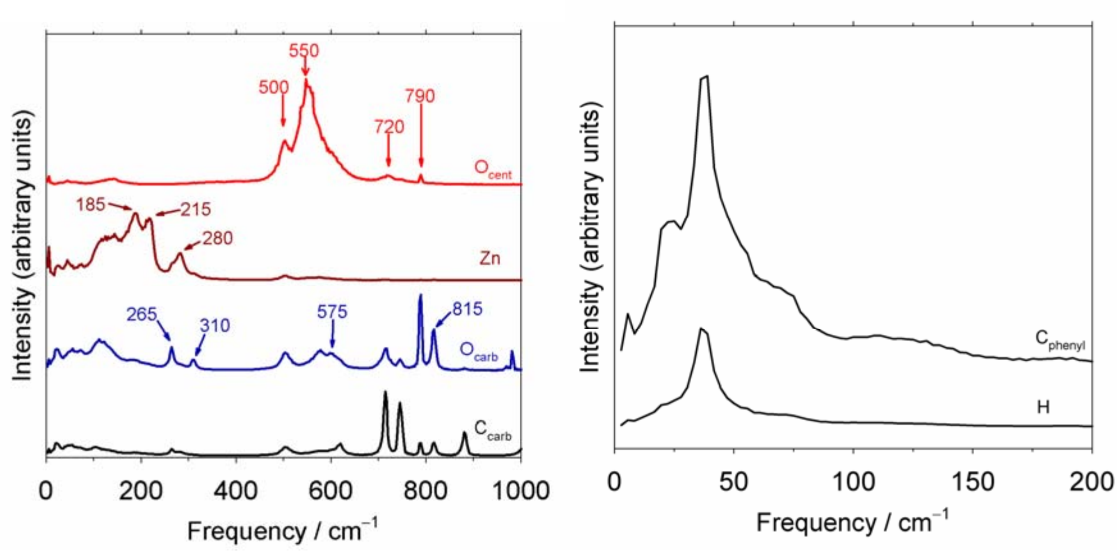

Figure 5.4. IRMOF-1 atomic power spectra for atom types Zn, O_{cent}, and carboxylate atoms (top), and for H and C_{phenyl} showing the internal rotation of the C_6H_4 unit (bottom).

Table 5.4. Comparison of calculated vibrational frequencies (in cm^{-1}) for IRMOF-1.

Mode	This Work	Bonded FF[18]	Bonded FF[17]	DFT[2]	Exp.[14,21]
C_6H_4 torsion	40		40		
Zn-O$_{cent}$ symmetric	185, 215, 280	200, 213		136	
Zn-O$_{cent}$, asymmetric	510, 550-560	516-530	664	512	534
Zn-O$_{carb}$	500, 575-600	572, 576	552	579, 606	
Carboxylate	720, 790, 815		759, 972	749, 830	750, 825

In addition to these vibrations, a strong band near 40 cm^{-1} is seen (Figure 5.4) that involves phenyl C and H atoms. We assign this band to the internal (torsional) rotation of the phenyl ring. This result agrees with a DFT/B3LYP normal mode analysis, in which the frequency of this motion was predicted to occur between 60 cm^{-1} and 80 cm^{-1}.[18] The temperature dependence of atomic motion within the framework predicted by the MD simulations is also consistent with recent NMR studies, which detect torsional "flips" of aromatic rings in IRMOF-1.[22] At 300 K, almost no such motion is seen, but at 400 K almost all phenyl rings exhibit this behavior. Although we did not quantify the torsional behavior by extracting an activation barrier, our simulations exhibit similar phenomena, as shown in an animation of MD results (Supporting Information). Another DFT calculation suggests that an energy barrier of approximately 51.8 kJ·mol^{-1} exists for the 90° rotation of the linker.[6] Recent quasielastic neutron scattering measurements of IRMOF-1 at 4 K show no evidence of any free rotation of the BDC linker,[6] in agreement with the low-temperature deuterium NMR data.[22] However, above room temperature, deuterium NMR shows evidence of phenyl rings undergoing 180° flips.[22] At 223 K and 298 K, the NMR signal represents a superposition of mostly static and a small fraction of "flipping" phenyl rings. At 373 K, however, all phenyl rings appear to undergo the flipping motion. At lower temperatures, the fraction of phenyl rings undergoing this motion appears to be related to the synthetic method. The fast precipitation method characteristic of the low-surface-area phase (MOCP-L) is thought to contain impurities that result in increased C_6H_4 torsional motion compared with IRMOF-1.[22]

Structural changes with adsorbed species

As discussed in the Introduction, the dimensions of MOF unit cells can change significantly upon adsorption of guest molecules. Using our flexible force field, MD simulations can be used to quantify any changes in unit cell structure and free volume upon adsorption, and agreement with experimental measurements of such changes constitutes a further validation of force field performance. Gravimetric data for hydrocarbons and chloromethanes adsorbed within IRMOF-1 are available for comparison with our MD simulations (Table 5.5).[7] As a starting point for MD simulations, we used the number of adsorbate molecules contained in completely filled IRMOF-1 pores obtained from the liquid sorption data given in ref 43. Values for free volume and the fraction of the pore volume occupied by guests were computed directly from the average lattice parameters (*NPT* simulations at 300 K, standard deviations less than 0.03 Å), while the Dubinin-Raduskhvich equation was used to estimate these values from the gravimetric data.[7] Unfortunately, experimental lattice parameters were not reported for the adsorbed hydrocarbon and chloromethane systems. In addition to the hydrophobic guests commonly used in IRMOF-1 adsorption experiments, we also include ethanol, since it is a hydrophilic guest capable of forming hydrogen bonds between guests and the framework.

Table 5.5. Simulation Results for Guest Adsorption.

			Simulation			Experiment[7]	
Guest	guest/ unit cell	guest mass %	lattice parameter (Å)	free volume $(cm^3 \cdot g^{-1})^a$	guest volume $\%^b$	free volume $(cm^3 \cdot g^{-1})^a$	guest volume $\%^b$
None			25.64				
CH_3CH_2OH	95	41.5	25.56	0.90	55.2		
CH_2Cl_2	88	54.8	25.70	0.91	55.1	0.93	55
$CHCl_3$	71	57.9	25.69	0.93	56.0	0.94	55
CCl_4	59	59.6	25.70	0.92	55.7	0.94	55
C_6H_{12}	51	41.1	25.77	0.90	53.5	0.92	54

[a] Calculated as the volume of guest (assuming bulk liquid density) divided by the unit cell mass of pure IRMOF-1.

[b] Calculated as the ratio of guest volume (assuming bulk liquid density) to total volume.

As seen in Table 5.5, in all cases the guest molecules occupy approximately 53.5 – 56.0 % of the total volume, in good agreement with experiment.[7] There are five pores within the IRMOF-1 unit cell, so the predicted pore occupancy ranges from 10 molecules in the case of hexane to 19 molecules in the case of ethanol. Interatomic distances computed from radial distribution functions (Table 5.6) indicate that, with the exception of hexane, guest molecules appear to be somewhat more tightly packed in the bulk liquid than in the IRMOF-1 pores. To make this comparison, we simulated the bulk liquids in the *NVT* ensemble, using their experimental density at 1.0 atm and 300 K. The results indicate that C-C distances are approximately 3% greater in the IRMOF-1 pore than in the bulk for the chlorinated species and ethanol, while the distances are unchanged for hexane. Cl-Cl distances are also larger in the MOF than in the bulk for the polar compounds CH_2Cl_2 and $CHCl_3$, but are unchanged in the case of non-polar CCl_4. O-O distances in ethanol are also essentially unchanged from the bulk liquid. We conclude that the local guest structure within the pores is essentially identical to the bulk phase for these compounds.

These results concerning the local guest structure are consistent with the predicted changes in unit cell dimensions upon adsorption, which are small. In the case of the chlorinated species and hexane, a slight increase in cell volume is predicted (0.7 – 1.5%). In contrast, ethanol, which is both more polar and capable of hydrogen bonding with O_{carb} atoms of IRMOF-1, there is a small contraction (–0.9 %). This result is consistent with the interaction water with in IRMOF-1.

Benzene is omitted from Tables 5.5 and 5.6 because MD simulations involving this molecule (63 C_6H_6 per unit cell) result in a severely distorted framework. Given that our results for other guests agree with experiment, simulations of IRMOF-1 pores completely filled with benzene may require an adjustment of the MOF-C_6H_6 force field parameters. Noting that a modified version of our force field greatly reduces the attractive potential of the O_{carb} atom,[3] it is possible that such an approach would yield better results for benzene adsorption.

Table 5.6. Intermolecular Distances for Guest Molecules from Radial Distribution Functions.

	C-C		Cl-Cl		O-O	
Guest	IRMOF-1	Bulk	IRMOF-1	Bulk	IRMOF-1	Bulk
CH_3CH_2OH	4.65	4.53			3.03	3.02
CH_2Cl_2	5.13	5.00	3.95	3.79		
$CHCl_3$	5.38	5.22	3.83	3.68		
CCl_4	5.82	5.63	3.68	3.69		
C_6H_{12}	2.99	2.98				

Benzene diffusion at low loading

As a final test of our force field approach, we compared simulated self-diffusion coefficients (D_{self}) for adsorbed benzene with both the flexible force field of Tafipolsky *et al.*[23] and experimental NMR results.[24] A series of *NVT* simulations were performed at temperatures of 250 K, 300 K, 350 K, and 400 K, using a low benzene loading of 10 molecules / unit cell (11 wt %) to match the experimental system. Results are displayed in Figure 5.5 as Arrhenius plots. Three experimental values of D_{self} were reported. The upper and lower blue points in Fig. 5.5 represent short-time "intracrystalline" diffusion coefficients (3.8×10^{-10} $m^2 \cdot s^{-1}$ and 1.9×10^{-9} $m^2 \cdot s^{-1}$, average of two reported values in each case), while the middle blue point represents the arithmetic mean of these two values for D_{self} (1.4×10^{-9} $m^2 \cdot s^{-1}$).[24] For purposes of comparison with our results, the intracrystalline value is the most appropriate one.

The D_{self} value determined from the MD simulation differs from the experiment by a factor of about 8. However, the computed activation energy for diffusion of 14.3 $kJ \cdot mol^{-1}$ is in excellent agreement with the value of 14.0 $kJ \cdot mol^{-1}$ predicted by Amirjalayer *et al* (black line) using the MM3-based flexible force field.[23] Keeping the framework atoms fixed at their crystallographic coordinates[7] results in lower values of D_{self} (green line) and a significantly lower activation energy of 9.8 $kJ \cdot mol^{-1}$, highlighting the importance of a flexible force field when modeling transport of larger hydrocarbon guests. A similar effect is seen in simulations of methane diffusion in zeolites, but is less prominent for larger alkane guests.[25] At the higher guest loadings in those simulations, guest-guest interactions are expected to dominate diffusional motion, so the effect of framework flexibility should be reduced.[25]

The difference in benzene D_{self} values between the two flexible force field simulations, combined with the difficulty in simulating a system with much higher benzene loading (see above) indicate that the general-purpose CVFF force field parameters for organic guest molecules are not sufficient for MOF-(aromatic guest) simulations. Rather, guest parameters that produce good bulk properties should be considered for simulations at high loading. It should also be noted that the benzene D_{self} values from another CVFF-based flexible force field[3] are also in good agreement with the MM3-based results, which suggests again that the nonbonded parameters for MOF atoms, particularly O_{carb} atoms, need to be re-parameterized from the CVFF or metal oxide values.

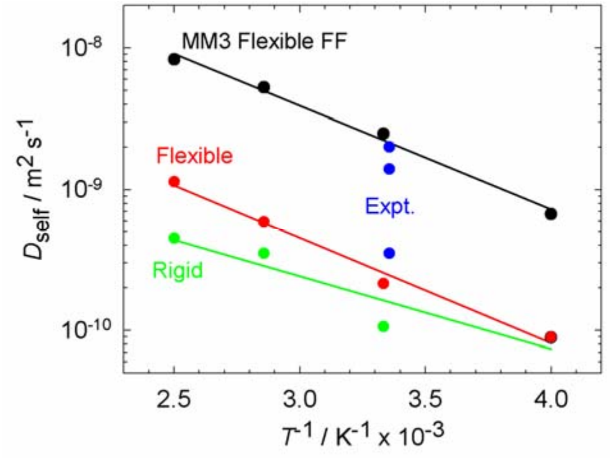

Figure 5.5. Comparison of benzene diffusion coefficients from simulations and experiment. Red and green circles are simulation results from this work for flexible and rigid frameworks, respectively. Black circles are simulation results from a flexible MM3-based forcefield.[23] Blue circles are experimental data points for intracrystalline diffusion coefficients (upper and lower points) and effective diffusion coefficient (middle).[24] Solid lines represent linear regressions from each simulation data set.

GCMC calculation

The original nonbonded parameters were recently modified by Dubbeldam et al. to reproduce CO_2 and CH_4 adsorption isotherms.[3] The initial atom positions for the framework are taken from the experimental crystal structure at 213 K.[7] We note that the reported structure contained guest solvent molecules, resulting in a lattice parameter (25.669 Å) that is slightly smaller than that found for the evacuated framework (25.885 Å) at 169 K.[7] Unlike the implementation we used for molecular dynamics simulations, in which the linker molecules are fully flexible (bond, angle, torsion), here we use a semi-flexible approach where the BDC linkers are treated as rigid structures. Test simulations in which linker flexibility was included by a torsional pivot move gave similar results to the semi-flexible force field.

The noble gases and methane molecules are described as spherically symmetric, uncharged Lennard-Jones particles, and the intermolecular interactions are modeled only with van der Waals potential parameters. A rigid three site model, with the H-H bond length fixed at 0.74 Å, is used for H_2.[26] A Lennard-Jones core is placed at the center of mass of the molecule with a point charge magnitude $-2q$ and point charge magnitude of q at the positions of the two protons. All revised interatomic potential parameters are given in Table 5.7.

Table 5.7. Force Field Parameters for Nonbonded Interactions According to Equation 1.

	species[a]	description	ε / k_B (K)[b]	σ (Å)	q (e)
IRMOF-1	Zn	zinc	0.42	2.700	1.275
	O_{cent}	inorganic oxygen	700.00	2.980	–1.500
	O_{carb}	carboxylate oxygen	70.50	3.110	–0.600
	C_{carb}	carboxylate carbon	47.00	3.740	0.475
	C_{phenyl}	phenyl carbon bonded to C_{carb}	47.86	3.470	0.125
	C_{phenyl}	phenyl carbon bonded to H	47.86	3.470	–0.150
	H	hydrogen	7.65	2.850	0.150
adsorbate	H_2	centre-of-mass	36.70	2.958	–0.936
		hydrogen	0.00	0.000	0.468
	CH_4		148.00	3.730	0.000
	Xe		216.85	4.100	0.000
	Kr		163.99	3.827	0.000
	Ar		119.80	3.400	0.000
	He		10.90	2.640	0.000

[a] IRMOF-1 and adsorbate parameters were taken from the literature: IRMOF-1,[3] H_2,[26] CH_4,[27] Xe,[28] Kr,[28] Ar,[29] and He.[29]

[b] k_B represents the Boltzmann constant.

The Grand canonical Monte Carlo (GCMC) code Towhee[30] was used at fixed temperature T, volume V, and adsorbate chemical potential μ to simulate gas adsorption. A Monte Carlo move consists of one of the following: translation of a molecule, rotation of a molecule, insertion of a new guest molecule, or deletion of an existing guest molecule. Rotation moves are not necessary for spherical particles. For simulations at room temperature, a total of 8 million MC moves are used for the simulations, and the last 5 million moves are used for averaging and analysis. A total of 28 million MC moves are used for the simulations of Ar adsorption at 78 K, and the last 10 million moves are used for averaging and analysis. Results are obtained by a block averaging technique, with each block representing 1/20 of the production period. Insertion and deletion statistics are monitored to ensure microscopic reversibility, and the standard deviations of the adsorbate densities are within ± 3.0 % of the average.

The simulation box consists of one unit cell (space group *Fm*3*m*, lattice parameter 25.699 Å), with 424 atoms. Larger box dimensions (2 x 2 x 2 unit cell repeats) have previously been shown to give similar results as a single unit cell.[3] The real space cut off for the nonbonded potential energy is 11.0 Å, and the long range electrostatic interactions are calculated by the Ewald summation[31] with a precision of 1.0 x 10^{-4}. The Towhee code requires adsorbate chemical potentials rather than feed gas fugacity as input, so we performed "empty box" GCMC simulations (i.e., a box without the MOF unit cell) to establish appropriate chemical potentials for the target pressures.[32] Rather than applying an unrelated equation of state to correlate these two quantities, the same force field parameters used in the adsorption simulations are used to accurately determine the feed gas pressure. The standard deviations of the pressure and densities for the empty box simulations are approximately 1 %. For each value of μ, the simulated pressure was compared to the corresponding ideal gas pressure.[31] The two pressures did not deviate until at least 10 bar, suggesting reasonable accuracy at low pressures for spherical and polyatomic guest particles.

Excess adsorption, N_{ex}, is described as the amount of adsorbate in excess of bulk fluid at the system temperature and pressure in the available void volume. Simulations measure the absolute amount adsorbed, N_{abs}, therefore excess adsorption is calculated by[33]

$$N_{\mathrm{ex}} = N_{\mathrm{abs}} - V_{\mathrm{g}}\rho_{\mathrm{g}} \qquad (2)$$

where ρ_g is the bulk gas density determined by the "empty box" GCMC simulations mentioned previously. The void volume, V_g , is calculated from GCMC simulations of He adsorption and found to be 0.75 of the unit cell volume for IRMOF-1.

Upon adsorption or desorption, the enthalpy change of the adsorbate from the bulk phase to the adsorbed phase is described by the isosteric heat of adsorption, Q_{st}. For systems with low guest loading and feed gas pressure, Q_{st} can be calculated from the thermal energy RT and the average potential energy per molecule, U, using the ideal gas approximation[34]

$$Q_{st} = RT - U \qquad (3)$$

Investigation of noble gas selectivity by IRMOF-1 was carried out by GCMC simulations for Xe/Ar and Xe/Kr mixtures at 300 K at total pressures of 1 and 10 bar. The Xe selectivity, S_{Xe}, was calculated from the ratios of gas mole fractions in the feed gas phase (y) and the adsorbed phase (x). For Xe/Kr mixtures, S_{Xe} becomes[35]

$$s_{\mathrm{Xe}} = \frac{x_{\mathrm{Xe}} y_{\mathrm{Kr}}}{x_{\mathrm{Kr}} y_{\mathrm{Xe}}} \qquad (4)$$

Framework flexibility effects are essential in predicting IRMOF properties such as framework stability, guest diffusion, and mechanical properties. Our primary aim in this work is to determine the effect of such flexibility on adsorption properties, and we use the H_2 adsorption results to further validate the force field parameters. Figure 1 shows that very similar H_2 adsorption isotherms at 298 K result when either the rigid framework or semi-flexible framework approaches are used. The three-site model for H_2 includes atomic charges to enhance interactions with framework atoms. At very high feed gas pressure, framework flexibility results in a slight decrease in loading. Also in Figure 5.6, our results show a slight underprediction compared to the simulations of Garberoglio et al.,[36] who used parameters directly from the Universal Force Field for framework atoms.[37] In that work, H_2 was modeled using a charge-neutral single van der Waals site,[38] which showed better agreement with experiment than the three-site H_2 model[39] at 78 K. We present results at room temperature only, so quantum effects between H_2 molecules can be ignored.

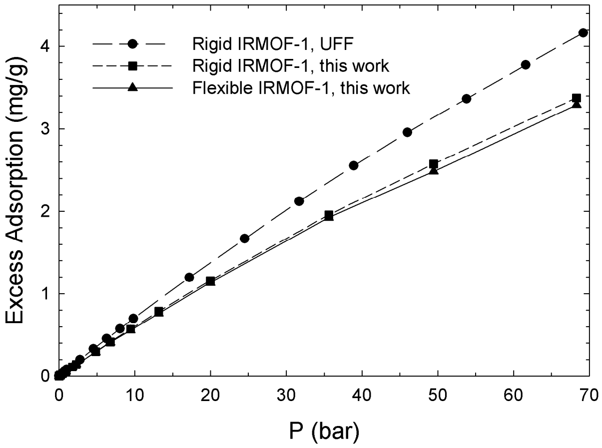

Figure 5.6. H_2 adsorption isotherm for IRMOF-1 at 298 K. Results from this work are compared with previous simulation results using a rigid framework with parameters from the Universal Force Field (UFF).[36]

Excess H_2 loadings are compared with previous simulation and experimental results in Table 5.8. Our results are centered between the experimental results of Panella et al.[40] and Dailly et al.,[41] while the simulation results of Garberoglio et al.[36] are in better agreement with the results of Dailly et al. Unfortunately, the difference in experimental procedures, combined with the well-known problem of consistent synthesis of high surface area IRMOF-1 crystals for adsorption experiments,[42,43] prevents us from drawing definitive conclusions concerning the accuracy of the simulation results. The isosteric heat of adsorption at 298 K was found to be 4.5 kJ·mol^{-1}, which is comparable to other GCMC simulation values reported at both 77 K and 298 K.[36,44] Good agreement is also found with the H_2 binding energy to IRMOF-1 obtained from quantum calculations (4.16 kJ·mol^{-1}).[45] The agreement is also excellent with experimental values at 78 K[40] and 298 K[41] (both 3.8 kJ·mol^{-1}).

Table5.8. Comparison of Excess H_2 Adsorption (mg·g^{-1}) in IRMOF-1 at 298 K.

	simulation		**experiment**	
P / bar	**this work**	**ref 69**	**ref 73**	**ref 74**
20	1.1	1.4	1.0	1.4
35	1.9	2.3	1.6	2.5
50	2.5	3.2	2.2	3.8
65	3.2	3.9	2.8	4.5

The remainder of our results concern the adsorption capacity and separation capabilities of IRMOF-1 with respect to noble gases. Figure 5.7 compares the effect of framework flexibility on the simulated Ar isotherms at 78 K and 298 K. For Ar adsorption at both temperatures, both framework approximations result in an Ar loading of approximately 2125 mg/g, which is significantly higher than the experimental value of ≈1500 mg/g.[7] As has been pointed out in several papers, however, defects from the synthesis procedures often result in an underestimation of the accessible volume,[46,47] so the measured excess adsorption would be too low.

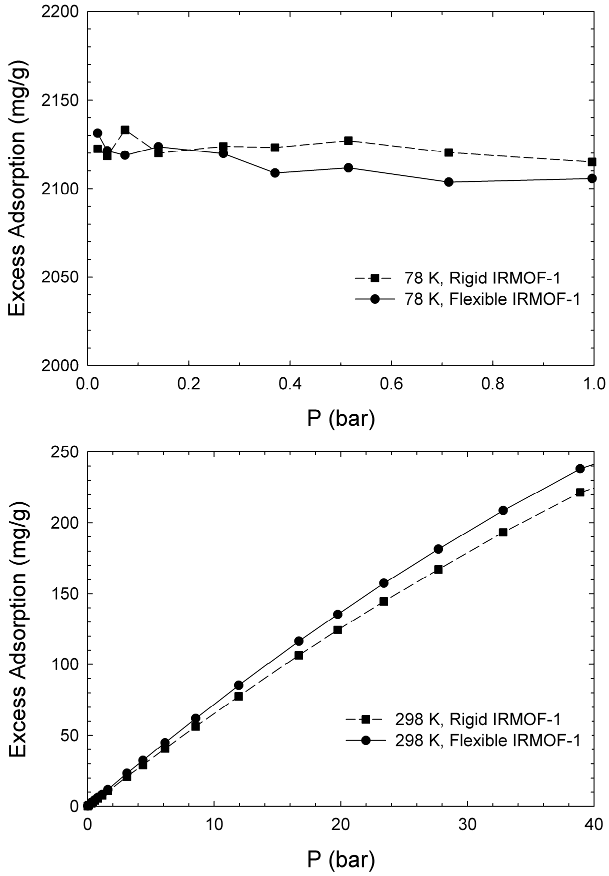

Figure 5.7. Argon adsorption isotherms for IRMOF-1 at 78 K (top) and 298 K (bottom).

Practical applications of noble gas adsorption and separation by IRMOFs require results near room temperature. Although we have seen little difference between rigid and flexible frameworks for small molecule adsorption, the computational cost of including framework moves is small. We therefore include framework moves for the remainder of our results. In Figure 5.8 we compare our simulated Xe adsorption isotherm for IRMOF-1 with experimental data collected at 292 K. There is good agreement at low pressure, but at higher pressures the simulation underpredicts the experimental Xe loading. The results for H_2 adsorption shown in Table 5.8 indicate that adsorption simulations can either over- or underpredict experimental results. However, the very good agreement at low Xe loading is a strong validation of our approach. A snapshot from the production simulation (Figure 5.9) indicates that there is no preferred binding site for Xe atoms at room temperature. This is different behavior than predicted for light gases at 30 K, in which the zinc-oxygen clusters are the preferred binding sites, but is consistent with the predictions for room temperature.[46] However, Figure 5.9 is consistent with ^{129}Xe NMR spectra at room temperature, indicating that Xe atoms occupy all possible adsorption sites within the IRMOF-1 pore.[48] The force field parameters used in this study were optimized by fitting to experimental CO_2 adsorption data and validated by comparison with CH_4 adsorption data, both obtained at room temperature.[3] We are confident that this potential parameterization for IRMOF-1 successfully captures binding sites for both electrostatic and van der Waals interactions.

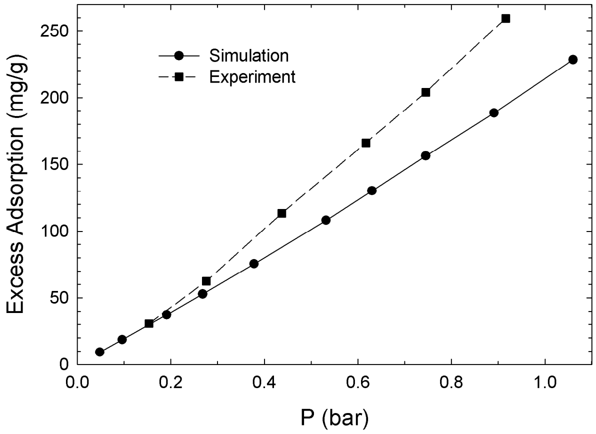

Figure 5.8. Xe adsorption isotherms for IRMOF-1 at 292 K, comparing simulation and experiment.[49]

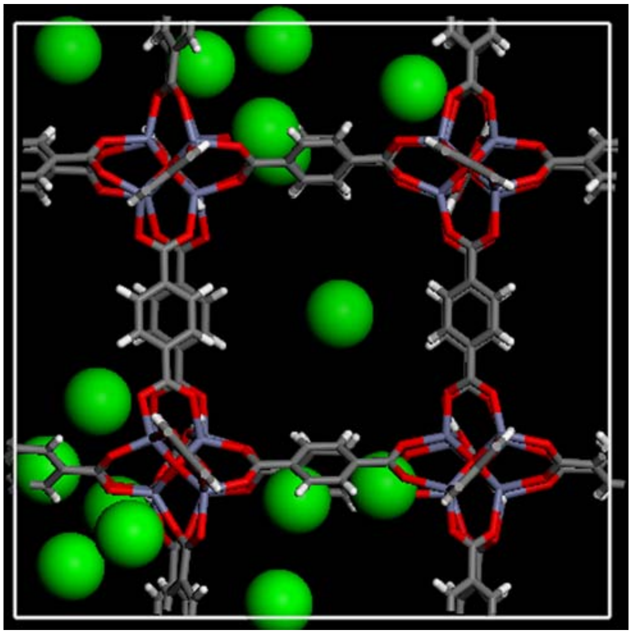

Figure 5.9. Snapshot showing Xe adsorbed by IRMOF-1 at 292 K (Zn blue, O red, C gray, H white, Xe green).

The ability of IRMOF-1 to store noble gases at much higher densities than the corresponding “empty containers” has been demonstrated experimentally.[50] Corresponding GCMC simulation results are presented in Figure 5.10 for comparison. The agreement between the empty container compression curves (red lines in Figure 5.10) and the experimental results is excellent, suggesting that the van der Waals parameters correctly describe the gas-gas interactions for compressed Ar, Kr, and Xe. The simulated inflation curves (blue lines in Figure 5) show qualitatively that significant additional amounts of each gas can be stored in the same container filled with IRMOF-1. As usual, the simulation results overpredict the adsorption isotherms, but for this specific comparison two comments are in order. First, the simulations involve perfectly crystalline IRMOF-1, while the "*in situ* activated MOF sample" used experimentally[50] almost certainly contained defects that would have reduced the surface area. Second, the simulated container has the dimensions of exactly one unit cell of IRMOF-1, while the experimental container could not have been completely filled with IRMOF-1 and therefore contained some empty space.

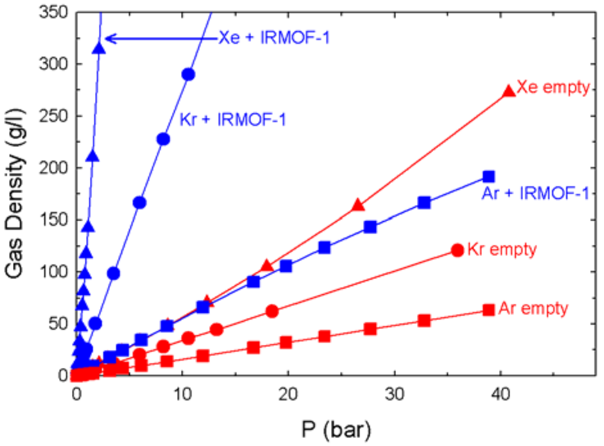

Figure 5.10. Simulated compression curves for noble gases in empty containers (red), compared with inflation curves (blue) in the presence of IRMOF-1. The blue curves represent total gas adsorption , not excess adsorption, for comparison with experimental results.[50]

Having validated the flexible force field for IRMOF-1 with adsorption isotherms of pure noble gases, we aim to use the simulations as a predictive tool in noble gas separations. A copper MOF has been shown to preferentially adsorb Xe in a Xe/Kr mixture, which leads to efficient separation.[50] According to Figure 5.11, IRMOF-1 also shows a preferential adsorption for Xe over the smaller noble gases Kr and Ar. The selectivity for Xe, and the pressure dependence of S_{Xe}, is greatly enhanced when Xe is mixed with smaller atoms (Ar) compared with larger atoms (Kr). However, even smaller selectivities seen in the Xe/Kr mixtures (2.5-3.0) lead to an effective separation of the gases. When $y_{\mathrm{Xe}} = 0.1$ (10% of the feed gas is Xe, 90% is Kr), the adsorbed phase consists of 38% Xe and 62% Kr.

The optimization of MOFs for gas separation must involve an examination of the atomic properties of both feed gas and substrate, as well as their intermolecular interactions. For IRMOF-1, the separation of Xe/Kr and Xe/Ar mixtures shows a dependence on feed gas properties. Figure 5.12 compares the Xe selectivity in equimolar Xe/Kr and Xe/Ar mixtures at total feed pressures of 1 bar and 10 bar. The comparison is made using the van der Waals well depth ε, but a similar trend is seen if the van der Waals diameter σ is used. Xe selectivity is larger in the Xe/Ar mixture because the ratio of $\varepsilon_{\mathrm{Xe}}/\varepsilon_{\mathrm{Ar}}$ is larger than $\varepsilon_{\mathrm{Xe}}/\varepsilon_{\mathrm{Kr}}$.

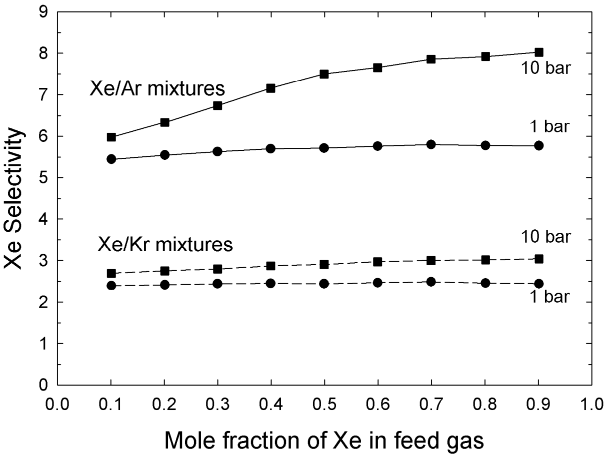

Figure 5.11. Effect of feed gas composition on Xe selectivity for Xe/Ar mixtures (solid lines) and Xe/Kr mixtures (dashed lines) at 300 K and total feed pressures of 1.0 bar and 10.0 bar.

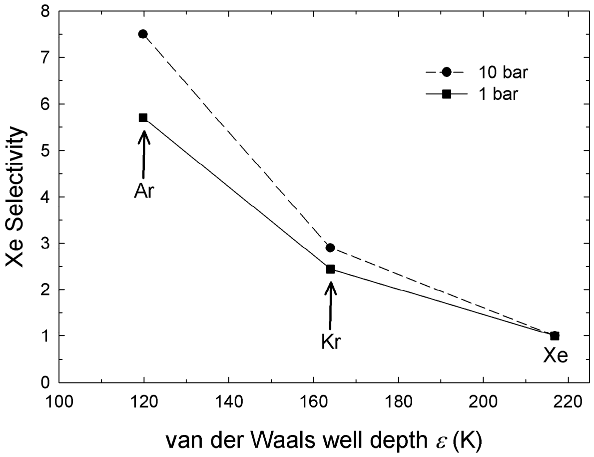

Figure 5.12. Effect of feed gas attractive potential on Xe selectivity at 300 K and pressures of 1 bar and 10 bar, for equimolar feed gas mixtures of Xe/Ar and Xe/Kr. The attractive potential energies for Ar, Kr, and Xe are indicated.

Reaction of IRMOF-1 with water

Understanding the interaction with water is of particular importance since the MOF crystal morphology is affected by exposure to water during synthesis or after evacuation.[51] In addition, zinc-based MOFs are water sensitive, losing their high surface area after prolonged exposure to humid air.[21] Recent molecular simulations of IRMOF-1 focus on their gas sorption capacity.[34,36,52,53] The framework itself is usually treated as a rigid body, and general force fields are used for MOF-adsorbate interactions. Such treatments cannot reproduce structural changes that occur upon absorption of guest molecules or be used to probe chemical reactions with the MOF. To our knowledge, no MOF-specific intramolecular parameters have been reported. Our hypothesis is that the interaction energy between Zn ions and water O atoms is similar to that between Zn ions and MOF O atoms. Water molecules could easily penetrate the pores and disrupt the framework. A possible mechanism might be (ignoring associated hydrolysis reactions):

$$(Zn_4O)(BDC)_3 + 4H_2O \rightarrow [(Zn_4O)(H_2O)_4(BDC)_2]^{2+} + BDC^{2-}$$

where BDC refers to the benzene dicarboxylate ion. Because Zn ions would interact with water molecules only through nonbonded (electrostatic and van der Waals) interactions, our methodology requires the use of only nonbonded force field parameters between Zn ions and MOF O atom

.

Constant-pressure molecular dynamics simulations were performed at 300 K on both pure IRMOF-1 and IRMOF-1 with up to 10 % water (by mass). Our approach combines a general force field (CVFF)[1] for the BDC linker with parameters optimized for the mineral zincite (ZnO). Simulated lattice parameters for zincite (a = 3.27 ± 0.01 Å, c = 5.24 ± 0.01 Å) are in good agreement with experiment (a = 3.26 Å, c = 5.21 Å).[54] Simulation of an isolated Zn ion in pure water resulted in a tetrahedral solvation shell (data) not shown), which is consistent with concentrated Zn solutions.[55]

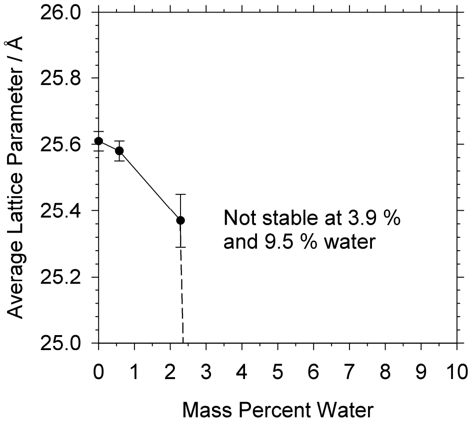

Figure 5.13. Simulated lattice parameter as a function of water content. The dashed line indicates the trend toward a much smaller lattice parameter (≈20 Å) at higher water content.

The lattice parameter of pure IRMOF-1 produced by our force field is 25.61 ± 0.01 Å, which is in good agreement with the range of reported X-ray diffraction values (25.67 Å – 25.89 Å).[4,7,8] Average bond and angle values also compare well with experiment,[56] although errors in nonbonded angles involving Zn are somewhat higher than those in the bonded BDC linker. These errors could be minimized by including bonding parameters (bond stretch and angle bend) between Zn and neighboring O atoms, which would require quantum chemical calculations. The good agreement with pure IRMOF-1 supports the combination of CVFF parameters for organic species with nonbonded parameters for ZnO. A more general force field with these additional bond and angle parameters and their application to other Zn-based MOFs are subjects of future work.

The result of added water on the simulated IRMOF-1 lattice parameter is shown in Figure 5.13. At low water content, the IRMOF-1 structure is maintained despite a decrease in lattice parameter to 25.37 Å (2.3 % water). At higher water contents of 3.9% and 9.5%, the IRMOF-1 structure collapsed within 200 ps to a high density state. Equilibrium was never obtained, but lattice parameters of ≈20 Å were observed. Our results are consistent with the experimental results of Huang *et al.*, which show a transformation in the IRMOF-1 XRD pattern and a decrease in surface area from ≈900 $m^2 \cdot g^{-1}$ to 45 $m^2 \cdot g^{-1}$ upon exposure to water.[21] The role of water in the disruption of the IRMOF-1 structure becomes evident by monitoring the coordination of Zn ions to neighboring O atoms. In pure IRMOF-1, each Zn ion is coordinated by one inorganic O atom (O1) and three BDC O atoms (O2). Both of these coordination numbers decrease with added water, as seen in Figure 5.14. Each Zn ion retains tetrahedral coordination, with water O atoms taking positions in the first shell. With classical

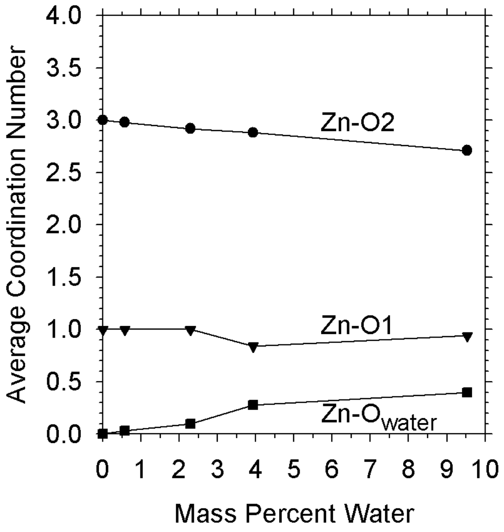

Figure 5.14. Changes in Zn coordination with increasing water. Zn retains tetrahedral coordination, but the relative amounts of BDC O (O2), inorganic O (O1) decrease as they are replaced by water O atoms (O_{water}).

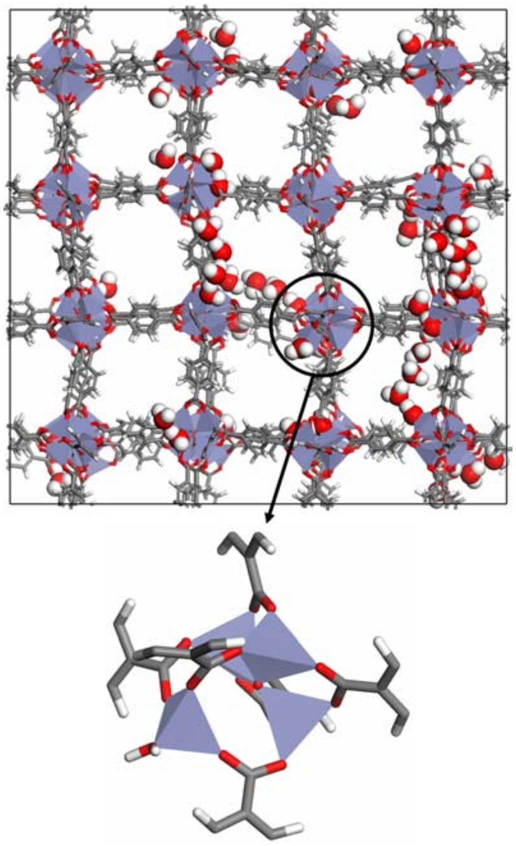

Figure 5.15. Disruption of the IRMOF-1 structure at 2.3 % water (top). The color scheme is Zn (purple), O (red), C (gray), and H (white), with ZnO4 tetrahedra represented as polygons. Also shown is a Zn_4O center in which an inorganic O atom has been replaced by a water O atom (bottom).

molecular dynamics simulations such as these, it is not possible to accurately model the protonation state of the aqueous BDC anion. Completely deprotonated BDC O atoms such as those seen in our collapsed structure would only occur in very basic solution. However, we believe that the simulations predict the initial mechanistic steps involved when a water molecule attacks a IRMOF-1 pore. As a water O atom approaches a ZnO_4 tetrahedron, either of the Zn-O1 or Zn-O2 first-shell interactions can be broken. Figure 5.14 shows that both O1 and O2 coordination have decreased by approximately 10% when the water content is 9.5%.

Our simulations indicate that water molecules interact with IRMOF-1 in three ways: 1) direct attack on a ZnO_4 tetrahedron in which a water O atom replaces one of the coordinating MOF O atoms (O1 or O2); 2) hydrogen bonding between a water H atom and O2; and 3) a hydrogen-bonded network of water molecules tethered (hydrogen-bonded) to one or more ZnO_4 tetrahedra. All three scenarios occur in the simulation system with 2.3 % water in IRMOF-1 (Figure 5.15). Even though IRMOF-1 is stable at this low water content, distortions in the framework structure occur. The structure shown in Figure 5.15 could be analogous to the hydrolyzed form of IRMOF-1 (a = 25.05 Å, c = 27.00 Å) described elsewhere.[21] An example of the first and apparently most destructive mode of interaction can be seen in the Figure 5.15 inset. In this case, the inorganic O atom (O1) becomes triply coordinated after a water molecule has taken up position in a ZnO_4 tetrahedron. The Zn ion is still coordinated by three BDC O atoms (O2), but without the anchoring O1 atom all three BDC ligands have increased freedom of rotation. As the water content increases, water molecules continue to attack ZnO_4 tetrahedra, and the framework eventually collapses. Upon removal of water from the 0.6 % and 2.3 % systems, the original IRMOF-1 structure is recovered after constant-pressure simulation. The water adsorption process thus appears to be reversible at low water content, in agreement with experiment.[21]

The stability of IRMOF-1 (and other MOF compounds) in water has received little attention in the literature,[21] perhaps because they can be prepared and characterized in other solvents.[4,7,8] However, the technological applications of MOFs would be greatly increased if new water-resistant frameworks were developed. Our simulation techniques provide insight into the mechanism of IRMOF-1 dissociation that is initiated by contact with water. The relatively weak interaction between Zn ions and O atoms in IRMOF-1 allows for attack by water molecules. Thus, a potential solution would be to tailor the metal-linker interactions so that they are stronger than possible metal-water interactions.

References

1. Dauber-Osguthorpe, P.; Roberts, V. A.; Osguthorpe, D. J.; Wolff, J.; Genest, M.; Hagler, A. T. *Proteins: Struct., Funct., Genet.* **1988**, *4*, 31.
2. Civalleri, B.; Napoli, F.; Noel, Y.; Roetti, C.; Dovesi, R. *CrystEngComm* **2006**, *8*, 364.
3. Dubbeldam, D.; Walton, K. S.; Ellis, D. E.; Snurr, R. Q. *Angew. Chem. Int. Ed.* **2007**, *46*, 4496.
4. Rowsell, J. L. C.; Spencer, E., C.; Eckert, J.; Howard, J. A. K.; Yaghi, O. M. *Science* **2005**, *309*, 1350.
5. Eddaoudi, M.; Moler, D. B.; Li, H.; Chen, B.; Reineke, T. M.; O'Keeffe, M.; Yaghi, O. M. *Acc. Chem. Res.* **2001**, *34*, 319.
6. Zhou, W.; Yildirim, T. *Phys. Rev. B* **2006**, *74*.
7. Li, H.; Eddaoudi, M.; O'Keeffe, M.; Yaghi, O. M. *Nature* **1999**, *402*, 276.
8. Eddaoudi, M.; Kim, J.; Rosi, N.; Vodak, D.; Wachter, J.; O'Keefe, M.; Yaghi, O. M. *Science* **2002**, *295*, 469.
9. Valencia, F.; Romero, A. H.; Hernandez, E.; Terrones, M.; Terrones, H. *New J. Phys.* **2003**, *5*, 123.
10. Bahr, D. F.; Reid, J. A.; Mook, W. M.; Bauer, C. A.; Stumpf, R.; Skulan, A. J.; Moody, N. R.; Simmons, B. A.; Shindel, M. M.; Allendorf, M. D. *Phys. Rev. B* **2007**, *76*, 184106.
11. Diao, J.; Gall, K.; Dunn, M. L. *J. Mech. Phys. Solids* **2004**, *52*, 1935.
12. Bordiga, S.; Lamberti, C.; Ricchiardi, G.; Regli, L.; Bonino, F.; Damin, A.; Lillerud, K. P.; Bjorgen, M.; Zecchina, A. *Chem. Comm.* **2004**, 2300.
13. Bordiga, S.; Vitillo, J. G.; Ricchiardi, G.; Regli, L.; Cocina, D.; Zecchina, A.; Arstad, B.; Bjorgen, M.; Hafizovic, J.; Lillerud, K. P. *J. Phys. Chem. B* **2005**, *109*, 18237.
14. Hermes, S.; Schroder, F.; Amirjalayer, S.; Schmid, R.; Fischer, R. A. *J. Mater. Chem.* **2006**, *16*, 2464.
15. Johnson, M. K.; Powell, D. B.; Cannon, R. D. *Spectrochim. Acta A* **1982**, *38*, 125.
16. Berkesi, O.; Andor, J. A.; Jayasooriya, U. A.; Cannon, R. D. *Spectrochim. Acta A* **1992**, *48*, 147.
17. Huang, B. L.; McGaughey, A. J. H.; Kaviany, M. *Int. J. Heat Mass Transfer* **2007**, *50*, 393.
18. Tafipolsky, M.; Amirjalayer, S.; Schmid, R. *J. Comp. Chem.* **2007**, *28*, 1169.
19. Green, J. H. S.; Kynaston, W.; Lindsey, A. S. *Spectrochim. Acta* **1961**, *17*, 486.
20. Spinner, E. *J. Chem. Soc. B* **1967**, 874.
21. Huang, L. M.; Wang, H. T.; Chen, J. X.; Wang, Z. B.; Sun, J. Y.; Zhao, D. Y.; Yan, Y. S. *Microporous Mesoporous Mater.* **2003**, *58*, 105.
22. Gonzalez, J.; Devi, R. N.; Tunstall, D. P.; Cox, P. A.; Wright, P. A. *Micropor. Mesopor. Mater.* **2005**, *84*, 97.
23. Amirjalayer, S.; Tafipolsky, M.; Schmid, R. *Angew. Chem. Int. Edit.* **2007**, *46*, 463.
24. Stallmach, F.; Groger, S.; Kunzel, V.; Karger, J.; Yaghi, O. M.; Hesse, M.; Muller, U. *Angew. Chem. Int. Edit.* **2006**, *45*, 2123.
25. Leroy, F.; Rousseau, B.; Fuchs, A. H. *Phys. Chem. Chem. Phys.* **2004**, *6*, 775.
26. Darkrim, F.; Levesque, D. *J. Chem. Phys.* **1998**, *109*, 4981.
27. Goodbody, S. J.; Watanabe, K.; Macgowan, D.; Walton, J.; Quirke, N. *Journal of the Chemical Society-Faraday Transactions* **1991**, *87*, 1951.
28. Hirschfelder, J. O.; Curtiss, C. F.; Bird, R. B. *Molecular Theory of Gases and Liquids*; Wiley: New York, 1965.
29. Maitland, G. C.; Rigby, M.; Smith, E. B.; Wakeham, W. A. *Intermolecular Forces: Their Origin and Determination*; Clarendon Press: Oxford, U.K., 1981.
30. http://towhee.sourceforge.net.
31. Frenkel, D.; Smit, B. *Understanding Molecular Simulation: From Algorithms to Applications*, 2nd ed.; Academic Press: San Diego, 2002.
32. Nicholson, T. M.; Bhatia, S. K. *Adsorption Science & Technology* **2007**, *25*, 607.

33. Myers, A. L.; Monson, P. A. *Langmuir* **2002**, *18*, 10261.
34. Duren, T.; Snurr, R. Q. *J. Phys. Chem. B* **2004**, *108*, 15703.
35. Heuchel, M.; Snurr, R. Q.; Buss, E. *Langmuir* **1997**, *13*, 6795.
36. Garberoglio, G.; Skoulidas, A. I.; Johnson, J. K. *J. Phys. Chem. B* **2005**, *109*, 13094.
37. Rappe, A. K.; Casewit, C. J.; Colwell, K. S.; Goddard, W. A.; Skiff, W. M. *J. Am. Chem. Soc.* **1992**, *114*, 10024.
38. Buch, V. *J. Chem. Phys.* **1994**, *100*, 7610.
39. Darkrim, F.; Vermesse, J.; Malbrunot, P.; Levesque, D. *J. Chem. Phys.* **1999**, *110*, 4020.
40. Panella, B.; Hirscher, M.; Putter, H.; Muller, U. *Adv. Funct. Mater.* **2006**, *16*, 520.
41. Dailly, A.; Vajo, J. J.; Ahn, C. C. *J. Phys. Chem. B* **2006**, *110*, 1099.
42. Hafizovic, J.; Bjorgen, M.; Olsbye, U.; Dietzel, P. D. C.; Bordiga, S.; Prestipino, C.; Lamberti, C.; Lillerud, K. P. *J. Am. Chem. Soc.* **2007**, *129*, 3612.
43. Tsao, C. S.; Yu, M. S.; Chung, T. Y.; Wu, H. C.; Wang, C. Y.; Chang, K. S.; Chent, H. L. *J. Am. Chem. Soc.* **2007**, *129*, 15997.
44. Frost, H.; Duren, T.; Snurr, R. Q. *J. Phys. Chem. B* **2006**, *110*, 9565.
45. Sagara, T.; Klassen, J.; Ortony, J.; Ganz, E. *J. Chem. Phys.* **2005**, *123*, 014701.
46. Dubbeldam, D.; Frost, H.; Walton, K. S.; Snurr, R. Q. *Fluid Phase Equilib.* **2007**, *261*, 152.
47. Surble, S.; Millange, F.; Serre, C.; Duren, T.; Latroche, M.; Bourrelly, S.; Llewellyn, P. L.; Ferey, G. *J. Am. Chem. Soc.* **2006**, *128*, 14889.
48. Ooms, K. J.; Wasylishen, R. E. *Microporous Mesoporous Mater.* **2007**, *103*, 341.
49. Pawsey, S.; Moudrakovski, I.; Ripmeester, J.; Wang, L. Q.; Exarhos, G. J.; Rowsell, J. L. C.; Yaghi, O. M. *J. Phys. Chem. C* **2007**, *111*, 6060.
50. Mueller, U.; Schubert, M.; Teich, F.; Puetter, H.; Schierle-Arndt, K.; Pastre, J. *J. Mater. Chem.* **2006**, *16*, 626.
51. Burrows, A. D.; Cassar, K.; Friend, R. M. W.; Mahon, M. F.; Rigby, S. P.; Warren, J. E. *Cryst. Eng. Comm.* **2005**, *7*, 548.
52. Sagara, T.; Klassen, J.; Ganz, E. *J. Chem. Phys.* **2004**, *121*, 12543.
53. Skoulidas, A. I.; Sholl, D. S. *J. Phys. Chem. B* **2005**, *109*, 15760.
54. Albertsson, J.; Abrahams, S. C.; Kvick, A. *Acta Crystallogr. B* **1989**, *45*, 34.
55. Ohtaki, H.; Radnai, T. *Chem. Rev.* **1993**, *93*, 1157.
56. Methods, S. I.-. Supporting Information.

6. Growth of MOFs on Surfaces

Several applications of MOFs can benefit from their growth on solid supports such as surfaces and nano or microparticles. Sensing, catalysis, and optics which incorporate MOFs in particular could see myriad uses for supported materials. Unfortunately unlike many other functional materials such as semiconductors and organic polymers, the current synthetic procedures required for the formation of most MOFs are prohibitive of uniform surface attachment in patterned or thin film form. To date, very few reports exist dealing with the surface-bound growth of MOFs.[10-15] The goal of this task was to gain the skills needed to effectively grow and reproduce dense films of MOF materials on surfaces in order to expand the current scope of materials which can be manipulated in this fashion. To that end, we first began by repeating much of the cited work with IRMOF-1 and HKUST-1 surface growth.

Work with IRMOF-1 commenced with experiments on gold surfaces functionalized with carboxylate-terminated thiol SAMs. For this growth, a sol-gel method was employed in which the MOF was first nucleated under standard growth conditions, then the nuclei were allowed to deposit and bind to the SAM@Au surface and grow into a dense polycrystalline film. For this type of growth, IRMOF-1 was first nucleated using a 4:1 $Zn(NO_3)_2 \cdot 6H_2O$ to terephthalic acid ratio in diethylformamide solution heated with a profile of 16 hours at 95 °C followed by 105 °C for 4 hours. The mother liquor was then removed from the oven, where a portion was transferred to a separate smaller flask in a fume hood and cooled to room temperature for 2 hrs. A SAM-coated wafer was then introduced and the film was allowed to grow overnight. The SAM coating was achieved by immersing a Au@Ti@Si wafer in a 10 mM solution of either 11-mercaptoundecanoic acid or 16-mercaptohexadecanoic acid in slightly acidic ethanol for 16-24 hours. IRMOF-1 films grown in this fashion generated a thick layer of interlocked polycrystallites of an average size ~25 microns.

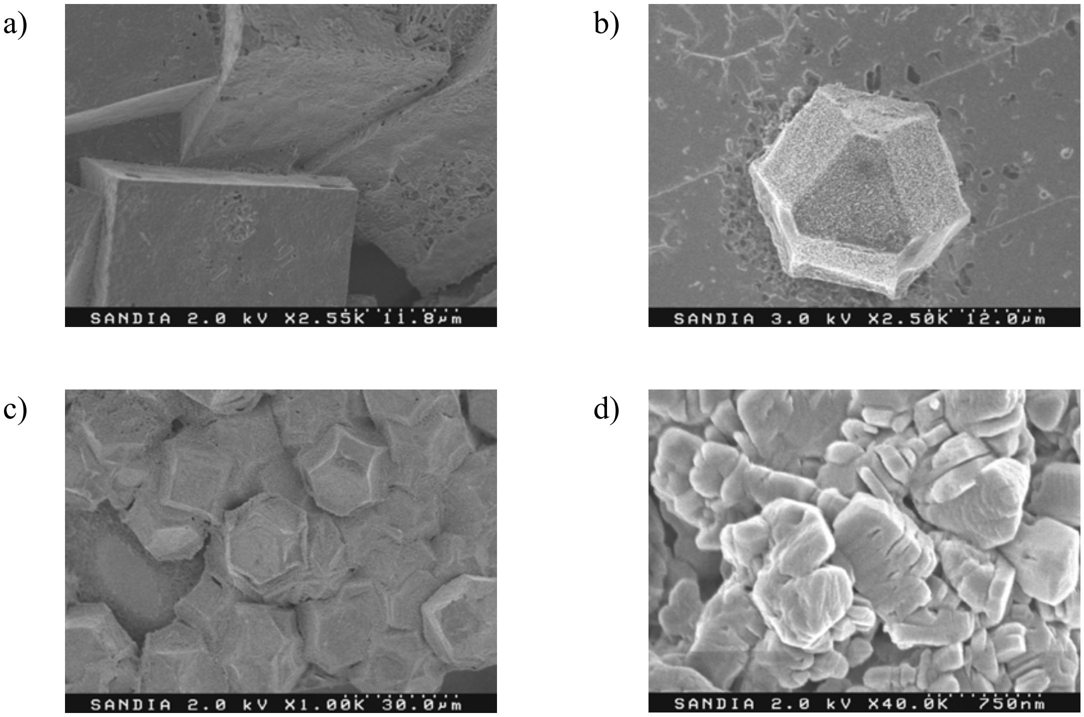

Figure 6.1: Images of different IRMOF-1 morphologies obtained by the sol-gel growth method. a) Cubic crystals are the most desirable, yet hardest to obtain; b) the truncated cubes were much more prevalent; c) often a mixture between the cubic and truncated forms was obtained; and d) if the film was exposed to atmosphere for a long period of time, the crystals showed degradation.

The images shown in Figure 6.1, illustrate both the different morphologies obtained and the inconsistencies of this growth method. We can obtain both cubic and truncated cubes, and usually achieved a mixture of the two. However, if the substrates are exposed to air for several hours, degradation due to water adsorption can be seen. It was also difficult to generate uniform films and smaller crystal sizes. Experiments were performed using filtration of the mother liquor prior to substrate in order to limit the initial size of the MOF nuclei. However, this often resulted not in smaller crystal features, but rather less dense coverage. Experiments with differing growth times, gave similar results with coverage density being the major sacrifice as opposed to feature size. Though IRMOF-1 is a popular material due to its high surface area and permanent porosity upon solvent removal, it is not an ideal substance for surface growth applications due to the complicated nature of the Zn-building unit and water sensitivity.

The material HKUST-1 has many of the desirable qualities of IRMOF-1, such as permanent porosity and high surface area, yet it is easier to handle due to its atmospheric robustness and simple $Cu(OAc)_2$-like paddlewheel building unit. In addition, it is an attractive material for chemical sensing, as evacuation of the terminally coordinated waters of the octahedral Cu-centers leaves open metal coordination sites in the MOF. Two recent reports of different methods of HKUST-1 surface growth were investigated. The first method is a colloidal procedure similar to the IRMOF-1 growth described above.[15] The MOF is nucleated from a 3:2 mixture of $Cu(NO_3)_2{\cdot}3H_2O$ and trimesic acid in 1:1 ethanol to water at 90 °C for 24 hours. The mother liquor is then cooled to room temperature in an ice/water bath for 10 minutes and filtered through a 0.2 μm membrane, and an appropriate substrate is immersed in a face down fashion for 3-5 days. Two different surfaces were used for these experiments. The carboxylate-terminated SAMs on gold were used as previously described. In addition, silicon substrates with a thin layer of ALD deposited alumina, which has a high surface concentration of hydroxyl termini, were also attempted. Both substrates gave similar growth with thick but spotty layers of octahedral crystals. Poweder x-ray diffraction data collected on the SAM@Au substrates showed the highly oriented growth expected from the literature.[15]

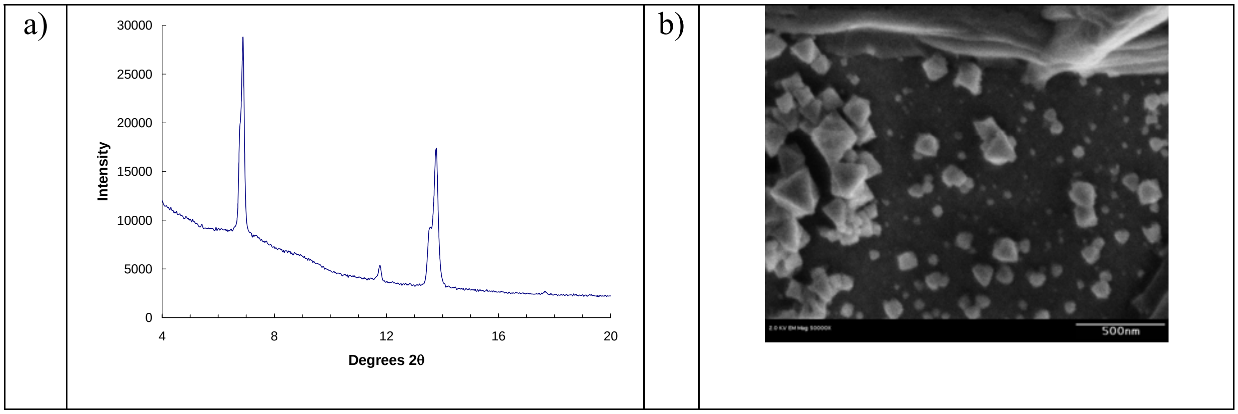

Figure 6.2: a) Powder X-ray diffraction pattern of HKUST-1 grown on a COOH-SAM@Au substrate *via* the single step *in situ* growth method. As expected, the pattern indicates the highly oriented growth. b) SEM of HKUST-1 grown on a SAM@Au showing the characteristic octahedral crystal morphology.

As can be seen in Figure 6.2, though growth is achieved by this method, the coverage is not uniform. The second growth method for HKUST-1 mentioned above is a step-by-step growth in which the nucleation occurs in a much more controlled fashion.[11] The substrate is immersed iteratively in ethanolic solutions of $Cu(OAc)_2$ and trimesic acid respectively with thorough washing between each immersion. Again, growth was achieved on both SAM@Au and ALD-alumina substrates, and again there was a large distribution of crystal size. However, as seen in Figure 6.3, there is a dense coverage of small crystallites over the entirety of the surface. The larger crystals appear to be less tightly bound as evidenced by a lack of specific growth orientation as seen in the previous method.

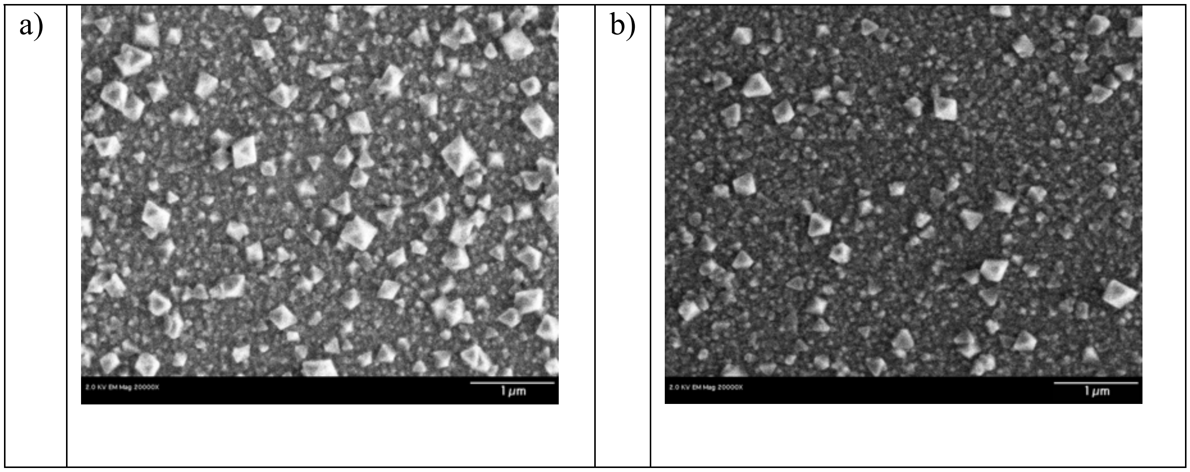

Figure 6.3: SEM images of HKUST-1 layers grown by a step-by-step procedure on a) COOH-SAM@Au and b) ALD-alumina substrates. Both show a dense layer of >100nm features with disoriented spotty coverage of larger crystals.

The dense layer is roughly 100 nm thick (based on cross sectional SEM), which is too thin for pXRD determination. To obtain a chemical determination of the identity of the material on these substrates a new method for the generation of surface enhanced Raman scattering (SERS) was devised. A thin layer of silver (5-10 Å) was evaporated onto the as synthesized HKUST-1 films. By comparison to unenhanced Raman scattering of bulk HKUST-1 and the weak signal from the pre-silver treated substrate, the chemical identity of the film was confirmed to be HKUST-1. This is the first use of SERS spectroscopy for the determination of MOF chemistries.

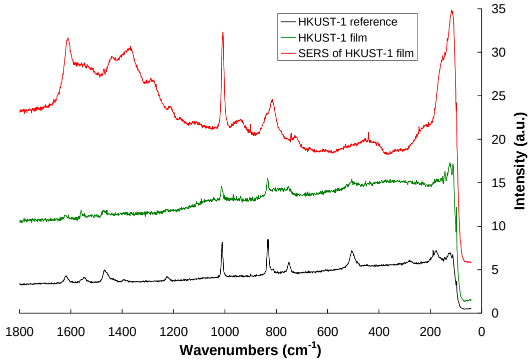

Figure 6.4: Comparison of the Raman spectra of bulk HKUST-1 (black), step-by-step surface grown HKUST-1 (green), and the SERS enhanced film (red).

Initial experiments on the surface growth of other materials have been attempted. In particular, the MOF-508 family of materials would be highly attractive as thin films for a variety of applications. For instance, infiltration of surface bound MOF-508 with a lanthanoid as described above would give immobilized red and green emissive materials for either light emitting devices or portable sensors. Our first experiments followed a hybrid growth method described in the growth of a different MOF by Kubo and coworkers.[14] Since MOF-508 is a three component MOF, step-by-step growth as described for HKUST-1 would be difficult, yet the growth rate of this material once nucleation has occurred is much faster than either HKUST-1 or IRMOF-1 so a colloidal growth method is also not feasible. The method thus chosen is a hybrid between the two. The substrates are subjected to several cycles of *in situ* growth from a solution of fresh starting materials. In the first growth cycle, a small number of crystals are adhered to the substrate surface. These initial crystals then act as seed crystals in the subsequent growth cycles. Figure 6.5 shows a comparison of the Raman spectra of bulk MOF-508 and a film after 6 growth cycles indicating that MOF-508 has deposited on the surface.

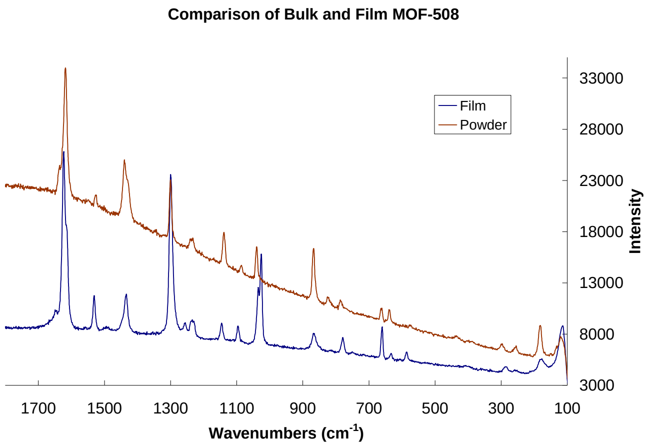

Figure 6.5: Comparison of the Raman spectra of bulk MOF-508 (brown) and a MOF-508 thin film (blue).

References:

1. M. Eddaoudi, J. Kim, N. Rosi, D. Vodak, J. Wachter, M. O'Keeffe and O. M. Yaghi, *Science*, 2002, **295**, 469-472.
2. S. S. Y. Chui, S. M. F. Lo, J. P. H. Charmant, A. G. Orpen and I. D. Williams, *Science(Washington, D. C.)*, 1999, **283**, 1148-1150.
3. B. Chen, C. Liang, J. Yang, D. S. Contreras, Y. L. Clancy, E. B. Lobkovsky, O. M. Yaghi and S. Dai, *Angew Chem Int Ed Engl*, 2006, **45**, 1390-1393.
4. B. Q. Ma, K. L. Mulfort and J. T. Hupp, *Angew. Chem., Int. Ed*, 2004, **43**, 2684.
5. M. Müller, S. Hermes, K. Kähler, M. W. E. van den Berg, M. Muhler and R. A. Fischer, *Chem. Mater*, 2008, **20**, 4576-4587.
6. F. Schröder, D. Esken, M. Cokoja, M. W. E. van den Berg, O. I. Lebedev, G. Van Tendeloo, B. Walaszek, G. Buntkowsky, H. H. Limbach, B. Chaudret and R. A. Fischer, *J. Am. Chem. Soc*, 2008, **130**, 6119-6130.
7. S. Hermes, M. Schroter, R. Schmid, L. Khodeir, M. Muhler, A. Tissler, R. W. Fischer and R. A. Fischer, *Angew. Chem. Int. Ed. Engl.*, 2005, **44**, 6237.
8. S. Hermes, F. Schröder, S. Amirjalayer, R. Schmid and R. A. Fischer, *J. Mater. Chem.*, 2006, **16**, 2464-2472.
9. N. Sabbatini, M. Guardigli and J.-M. Lehn, *Coord. Chem. Rev.*, 1993, **123**, 201-228.
10. D. Zacher, A. Baunemann, S. Hermes and R. A. Fischer, *J. Mater. Chem.*, 2007, **17**, 2785-2792.
11. O. Shekhah, H. Wang, S. Kowarik, F. Schreiber, M. Paulus, M. Tolan, C. Sternemann, F. Evers, D. Zacher and R. A. Fischer, *J. Am. Chem. Soc*, 2007, **129**, 15118-15118.
12. S. Hermes, F. Schroder, R. Chelmowski, C. Woll and R. A. Fischer, *J. Am. Chem. Soc.*, 2005, **127**, 13744-13745.
13. E. Biemmi, A. Darga, N. Stock and T. Bein, *Microporous and Mesoporous Materials*, 2008, **114**, 380-386.
14. M. Kubo, W. Chaikittisilp and T. Okubo, *Chem. Mater.*, 2008, **20**, 2887-2889.
15. E. Biemmi, C. Scherb and T. Bein, *J. Am. Chem. Soc.*, 2007, **129**, 8054-8055.

7. Metal Organic Frameworks as nano templates for Magnesium Hydride

The safe and efficient storage of hydrogen is one of the greatest challenges for its use as an alternative energy source. In order to find a way to store hydrogen economically, safely and environmental friendly with high gravimetric and volumetric density, tremendous effort has been made to store hydrogen in gas, liquid and solid state.[1]

Hydrides are important hydrogen storage materials which have a great potential as on-board sources of pure hydrogen for fuel cells and/or hydrogen combustion engines applied in automobiles. The challenge has been to obtain sufficiently strong bonding to molecular H_2 to achieve the target of 6.0 wt % H_2 near room temperature with pressures ~100 bar.[2]

In particular, Magnesium hydride is cheap and contains 7.7 wt % hydrogen, making it one of the most attractive hydrogen storage materials.[2] However, thermodynamics dictate that hydrogen desorption from bulk magnesium hydride only takes place at or above 300 °C, which is a major impediment for practical application.[3]

During the past two decades research efforts were devoted to modifying the Mg-based system, aiming at increasing the absorption/desorption rates and lowering the desorption temperature. Different approaches were reported, mainly involving alloying Mg with other elements, high energy or reactive ball milling of Mg, or surface modification of Mg. Currently, the reduction of the temperature of hydrogen desorption from solid hydrides to the range compatible with the waste heat of a fuel cell stack (roughly 60–150C range) is an important objective of the magnesium hydride research. A promising approach to address this issue is to reduce the particle size of the magnesium hydride to the nanometer range, resulting in enhanced kinetics without the need of a catalyst.[4]

It has been shown that nanocrystalline MgH_2 formed by intense ball milling leads to more improved properties than conventional polycrystalline MgH_2.[3] But mechanical milling of MgH_2 is limited to particle size down to 300 nm.[5] Apart from mechanical milling, nanocasting method is another effective way reported to prepare microporous and mesoporous materials, for which nanoporous carbon templates, have been used. [6]

The use of a Metal Organic Framework, (MOF-5) as a nanoporous template for preparing nano dimensional magnesium hydride is reported here. MOF-5 [$Zn_4O(bdc)_3$, bdc = benzene-1,4-dicarboxylate] is a highly crystalline microporous coordination polymer. The Zn_4O-cluster represents the central part of this structure (Fig. 7.1). Oxygen atoms are located in the centre of the tetrahedron coordinated by four zinc atoms that are positioned at the tetrahedra vertices. The edges of these tetrahedral are bridged by six carboxylate groups of the organic linker forming an octahedral node. The nodes are linked together with 1,4-phenylene groups of the bdc linker resulting in a three-dimensional cubic network.[7] However, the guest-free MOF-5 framework decomposes in the presence of moisture when the activated sample is exposed to air.[8] So all the manipulations have been carried out using either schlenk lines or nitrogen filled glove box.

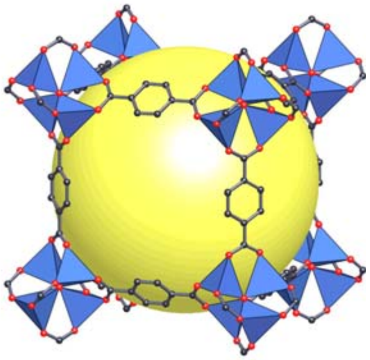

Fig. 7.1. MOF-5 template used in the study.

Recently, chemical vapor infiltration of organometallic compounds in to MOFs was demonstrated to be a highly efficient tool for the preparation of nano sized metals like platinum and palladium.[9] [10] Following this strategy, we used bis(cyclopentadienyl)magnesium $(C_5H_5)_2Mg$ as a precursor for the infiltration of Mg into MOF-5 pores. Experiments were carried out in a Schlenk tube maintained at 60 millitorr and heated at temperatures of 160C for 60 minutes. Color of the MOF-5 changed to dark brown at the end of the cycle indicating successful infiltration. Samples were analyzed for Magnesium using elemental analysis. They found to contain <1 ppm of Mg.

Some difficulties observed during the vapor phase infiltration were,

- The difficulty in consistent reproducibility.
- Air/moisture sensitivity of the Magnesium precursor
- Poor loading of Mg into MOF-5.
- Need for additional steps to reduce Mg to MgH_2 without reducing/decomposing the MOF-5 framework.

In order to overcome the above mentioned difficulties during vapor phase infiltration studies, a solution based synthesis approach was adopted. This was envisioned as an alternative by avoiding the use of highly reactive and air sensitive precursors and possible elimination of Mg reducing steps.

Dialkyl magnesium compounds MgR_2 (R = Et, Bu^n) are known to decompose at 170-210 C forming MgH_2 and correspomding alkane by β- hydrogen abstraction.[11] They are highly moisture sensitive and reactive compounds available as 1M solutions in organic solvents.

In a typical experiment, 200 mg of activated MOF-5 sample was injected with about 3 ml of 1M dibutylmagnesium solution in heptane. The resulting mass was kept for 16 hours under agitation in order to provide for uniform infiltration deep into the pores. The mixture is then heated to 200C for 12 hours to reduce the dibutylmagnesium to MgH_2 under dynamic vacuum. Colorless MOF-5 crystals turned into uniformly colored grey crystals at the end of the experiment. Solid State NMR taken of MOF-5 before and after infiltration is given in Fig.7.2. From NMR spectrum it could be seen that only peaks assigned to MOF-5 and that of MgH_2 indicating that MOF-5 remains intact after the infiltration and that MgH_2 is infiltrated inside the MOF-5 pores.

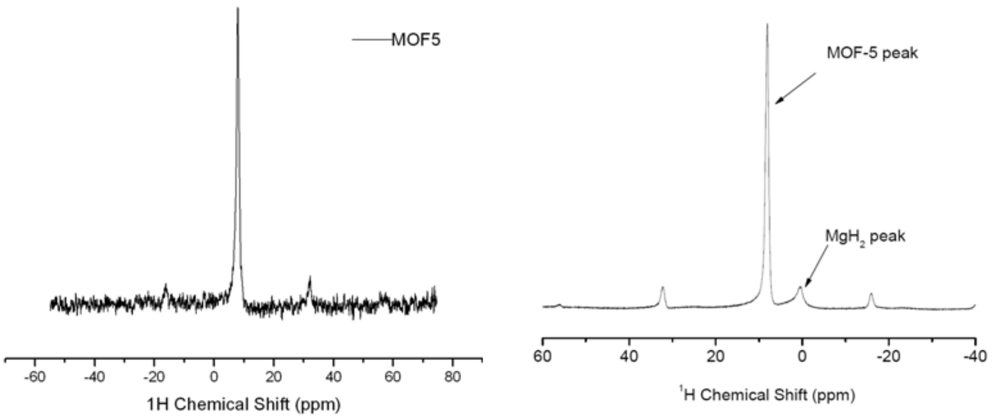

Figure 7.2. Solid state NMR of MOF-5 framework before and after infiltration with MgH_2.

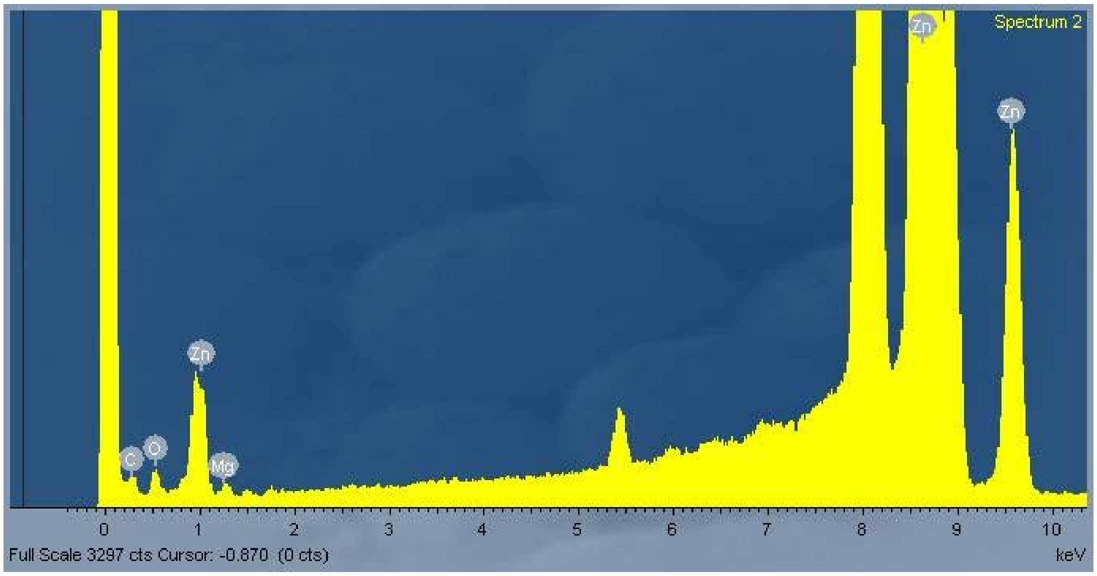

Figure 7.3. Energy Dispersive X-ray spectrum of MOF-5 loaded with MgH_2 and oxidized in order to facilitate the measurement.

Powder XRD patterns were taken before and after the infiltration experiments using mylar capsules. No significant changes in the XRD patterns were observed. But Energy-dispersive X-ray spectroscopy (EDX), showed the presence of Mg in the samples as shown in Figure 7.3.

Elemental analysis on the samples indicated a 4.2 wt.% loading of Mg into MOF-5 pores.

Since MgH_2 is moisture sensitive, the infiltrated samples were oxidized at 200C under flowing oxygen. The oxidized samples were analyzed using TEM. 4-6 nm size particles distributed inside MOF-5 pores were observed, as depicted in Fig. 7.4.

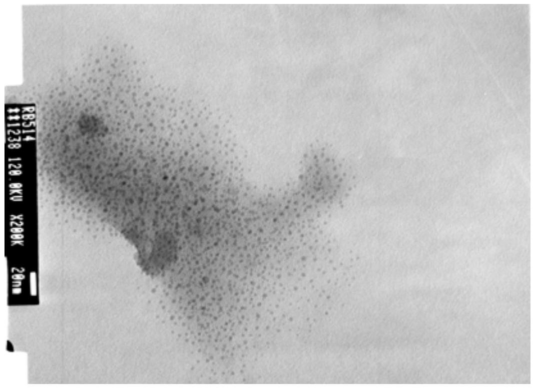

Figure 7.4. MgO nano particle(black dots) formed inside MOF-5 pores.

To analyze the dehydrogenation process qualitatively, samples were subjected to residual gas analysis (RGA). Exhaust gases were analyzed by mass spectrometry as a function of sample temperature. The sample showed the presence of organic impurities from the Mg precursor and water at higher temperatures. Hydrogen was desorbed from the sample at temperatures between 160 and 200C. Figure 5 shows the Pressure Vs Time spectrum at desorption of the sample at 160C.

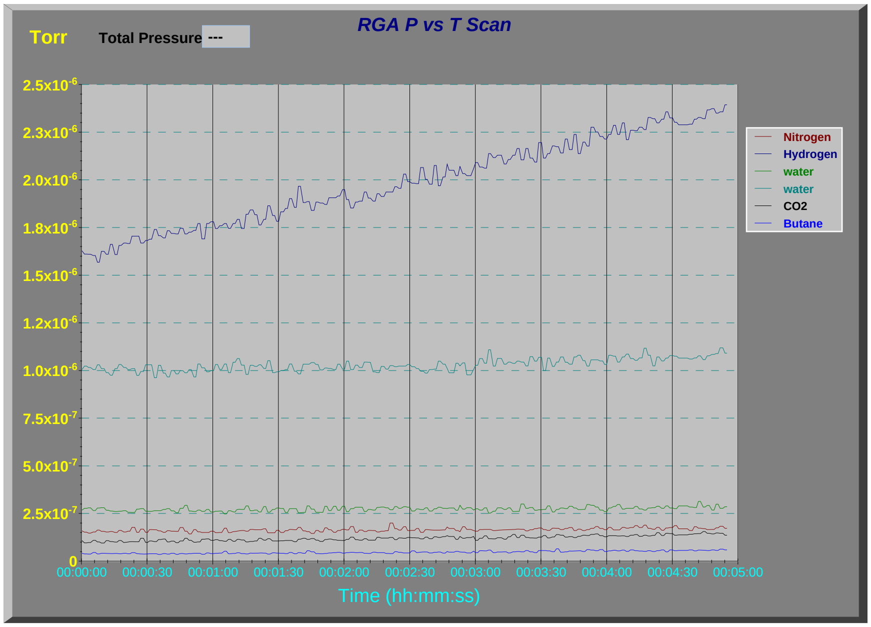

Figure 7.5. Pressure Vs Time spectrum of residual gas analysis showing hydrogen desorption at 160C.

Quantitative analysis to investigate the temperature dependence of hydrogen evolution from the sample were carried out using temperature programmed desorption (TPD) connected to TOF mass spectrometry over the temperature range of 20-400C. Evolution of organic species and water in addition to hydrogen did not allow the measurement of the partial pressure, or rate of evolution of hydrogen from the sample.

Similar experiments were carried out with LiH and $NaAlH_4$ infiltrations into MOF-5 and are at various stages of analyses. Efforts are being made to use robust MOFs which have less moisture sensitivity.

References

(1) Schlapbach, L.; Zuttel, A. *Nature* **2001**, *414*, 353.
(2) Zaluski, L.; Zaluska, A.; Strom-Olsen, J. O. *J. Alloys Compd.* **1997**, *253*, 70.
(3) J. Huot; G. Liang; S. Boily; A. van Neste; R. Schultz *J. Alloys Compd.* **1999**, *293-295*, 495.
(4) Varin, R. A.; Czujko, T.; Wronski, Z. *Nanotechnology* **2006**, *17*, 3856.
(5) Aguey-Zinsou, K.-F.; Ares Fernandez, J. R.; Klassen, T.; Bormann, R. *Int. J. Hydrogen Energy* **2007**, *32*, 2400.
(6) Cornelis P. Balde´; Bart P.C. Hereijgers; Johannes H. Bitter; Jong, K. P. d. *J. Am. Chem. Soc.* **2008**, *130*, 6761.
(7) H. Li; M. Eddaoudi; O'Keeffe, M.; O. M. Yaghi *Nature* **1999**, *402*, 276.
(8) Sabo, M.; Henschel, A.; Froede, H.; Klemmb, E.; Kaskel, S. *J. Mater. Chem.* **2007**, *17*, 3827.
(9) S. Hermes; M. K. Schroter; R. Schmid; L. Khodeir; M. Muhler; A. Tissler; Fischer, R. W.; R. A. Fischer *Angew. Chem., Int. Ed.* **2005**, *44*, 6237.
(10) Kim, H.; Chun, H.; Kim, G. H.; Lee, H. S.; Kim, K. *Chem. Commun.* **2006**, 2759.
(11) Stohmeier, W.; Siefert, F. *Chem. Ber.* **1961**, *94*, 2356.

Publications and Presentations

Journal Publications

1. M. D. Allendorf, C. A. Bauer, R. Bhakta, R. J. T. Houk “Luminescent Metal Organic Frameworks,“ accepted for publication, *Chem. Soc. Rev.* 2008.

2. Christina A. Bauer, Tatiana V. Timofeeva, Tiffany Kinnibrugh, Simon C. Jones, Mark D. Allendorf "The Effect of the Coordinated Metal on Luminescence in Stilbene Metal-Organic Frameworks," submitted to *Inorg. Chem.*, 2008.

3. Mark D. Allendorf, Ronald J. T. Houk, Leanne Andruszkiewicz, A. Alec Talin, Joel Pikarsky, Arnab Choudhury, Kenneth A. Gall, and Peter J. Hesketh “Stress-Induced Chemical Detection Using Flexible Metal-Organic Frameworks,” submitted to *J. Amer. Chem. Soc.* June 2008.

4. Jeffery A. Greathouse, Tiffany L. Kinnibrugh, and Mark D. Allendorf “Adsorption and Separation of Noble Gases by IRMOF-1: Grand Canonical Monte Carlo Simulations,” submitted to *Ind. Eng. Chem. Res.* August 2008.

5. F. P. Doty, C. A. Bauer, A. J. Skulan, P. G. Grant, M. D. Allendorf “Scintillating Metal Organic Frameworks: A New Class of Radiation Detection Materials,” in press, *Adv. Mater.* August 2008.

6. Greathouse, JA; Allendorf, MD “Force field validation for molecular dynamics simulations of IRMOF-1 and other isoreticular zinc carboxylate coordination polymers,” *J. Phys. Chem. C.* 112 (2008), 5795-5802.

7. D. F. Bahr, J. A. Reid, W. M. Mook, C. A. Bauer, R. Stumpf, A. J. Skulan, N. R. Moody, B. A. Simmons, M. M. Shindel, M. D. Allendorf “Mechanical properties of IRMOF-1 metal-organic framework crystals,” *Phys. Rev. B*, 76(2007), 184106.

8. C. Bauer, T. Settersten, B. Patterson, T. Timofeeva, V. Liu, B. Simmons, M. D. Allendorf “Influence of connectivity and porosity on ligand-based luminescense in zinc MOFs,” *J. Amer. Chem. Soc.* 129 (2007), 7136.

9. Jeffery A. Greathouse and Mark D. Allendorf “Reactivity of metal-organic framework-5 with water studied by molecular dynamics simulations,” *J. Amer. Chem. Soc.*, 128 (2006), 10678.

Presentations

1. R. A. Fischer, S. Hermes, F. Schröder, C. Wöll, M. Allendorf, “Metal@mofs: perspectives of metal organic open frameworks as novel host matrices for imbedding functional nanoparticles,” SAMIC Trends in Nanoscience conference, Dec. 4-7, 2005, Bressanone, Italy, invited lecture.

2. F. Schroeder, S. Hermes, A. Baunemann, C. Bauer, A. J. Skulan, B. A. Simmons, M. D. Allendorf, C. Wöll, R. A. Fischer “Thin films of metal organic framework compounds: Design and characterization of new functional surfaces,” poster, Amer. Chem. Soc. Spring Meeting, Atlanta, GA, March 26 – 30, 2006.

3. C. Bauer, F. Schröder, A. J. Skulan, A. A. Talin, R. Anderson, R. A. Fischer, B. A. Simmons, M. D. Allendorf “Electronic and Luminescent Properties of Metal-Organic Frameworks: Toward Gas Sensors,” Amer. Chem. Soc. Spring Meeting, Atlanta, GA, March 26 – 30, 2006.

4. J. A. Greathouse, R. Schmid, M. D. Allendorf “Development of a nNon-bonded forcefield for molecular modeling of metal organic frameworks,” Amer. Chem. Soc. Spring Meeting, Atlanta, GA, March 26 – 30, 2006.

5. A. J. Skulan, C. Bauer, F. Schroeder, S. Hermes, R. A. Fischer, B. A. Simmons, M. D. Allendorf "Hybrid Materials of Metal Organic Frameworks (MOF)," 209th Meeting of The Electrochemical Soc., May 7 – 11, 2006, Denver, CO.

6. J. A. Greathouse and M. D. Allendorf “Molecular dynamics simulations of metal-organic framework-5 and its interactions with water,” presented at Fall meeting of The American Chemical Society, San Francisco, CA, Sept. 10 –14, 2006.

7. Renée Shediac, Elaine Lai, Christina Bauer, Blake A. Simmons, Arnab Choudhury, Peter J. Hesketh , Mark D. Allendorf “Growth of Metal Organic Frameworks onto Microcantilever Substrate Materials,” Fall meeting of The Electrochemical Society, Oct. 29 – 3, 2006, Cancun, Mexico.

8. J. A. Greathouse, M. D. Allendorf “The Interaction of Water with Metal Organic Framework-5 Simulated by Molecular Dynamics Using a New Non-Bonded Forcefield,” Fall AIChE meeting, Nov. 12-17, 2006, San Francisco, CA.

9. Blake Simmons, David Bahr, Mark Allendorf, William Mook, Christina Bauer, Neville Moody “Synthesis, Characterization, and Mechanical Properties of Metal Organic Frameworks,” Fall 2006 MRS meeting, Nov. 26 – 30, 2006, Boston, MA.

10. M. D. Allendorf “Metal Organic Frameworks: Nanoporous Materials for Sensing, Separations, and More,” invited lecture, Oct. 12, 2006, Dept. of Chemical Engineering, University of Colorado, Boulder, CO.

11. M. D. Allendorf “Metal Organic Frameworks: Nanoporous Materials for Sensing, Separations, and More,” Electrochemical Society San Francisco Section meeting, Feb. 13, 2007, Oakland, CA.

12. J. A. Greathouse, M. D. Allendorf “Validation of a Nonbonded Force Field for Metal-Organic Frameworks,” presented in *Nanoporous Materials: Chemistry and Applications*, symposium held at The Electrochemical Society Spring Meeting, Chicago, IL, May 7 – 11, 2007.

13. N. W. Ockwig, M. D. Allendorf “Cobalt based isoreticular metal-organic frameworks (IRMOFs): A theoretical study on viability and stability,” presented in *Nanoporous Materials: Chemistry and Applications*, symposium held at The Electrochemical Society Spring Meeting, Chicago, IL, May 7 – 11, 2007.

14. F. P. Doty, C. A. Bauer, P. G. Grant, B. A. Simmons, A. J. Skulan, M. D. Allendorf “Novel Particle Detector Materials Based on Zinc-Stilbene Metal Organic Frameworks,” presented in *Nanoporous Materials: Chemistry and Applications*, symposium held at The Electrochemical Society Meeting, Chicago, IL, May 7 – 9, 2007.

15. F. P. Doty, C. A. Bauer, P. G. Grant, B. A. Simmons, A. J. Skulan, M. D. Allendorf “Radioluminescence and radiation effects in metal organic framework materials,” IEEE Conference “Penetrating Radiation Systems and Applications VIII”, Aug. 26-30, 2007, San Diego, CA.

16. Mark D. Allendorf, Jeffery A. Greathouse, Tiffany L. Kinnibrugh, Force Field Validation for Molecular Simulations of IRMOF-1 and Other Isoreticular Zinc Carboxylate Coordination Polymers,” CECAM conference, Lyon, France July 15 – 18, 2007.

17. Jeffery A. Greathouse, Tiffany L. Kinnibrugh, F. P. Doty, and Mark D. Allendorf, “Molecular Modeling of Gas Adsorption in Scintillating Metal-Organic Frameworks,” Fall MRS meeting, Boston, MA, Nov. 26 – 30, 2007.

18. F. P. Doty, C. A. Bauer, A. J. Skulan, P. G. Grant, B. A. Simmons, and M. D. Allendorf “Scintillation Materials based on Metal Organic Frameworks,” Fall MRS meeting, Boston, MA, Nov. 26 – 30, 2007.

19. Christina Bauer, Tatiana V. Timofeeva, Tiffany Kinnebrugh, Patrick Doty, Blake A. Simmons, Mark D. Allendorf “Tuning Linker-Based Luminescence in Metal-Organic Frameworks,” spring meeting of The American Chemical Society, New Orleans, LA April 6 – 10, 2008.

20. J. A. Greathouse, T. L. Kinnibrugh, M. D. Allendorf “Molecular simulation of gas adsorption in IRMOF-1 using a flexible force field,” spring meeting of The American Chemical Society, New Orleans, LA April 6 – 10, 2008.

21. F. P. Doty, C. A. Bauer, M. D. Allendorf “Radiation Detection Materials based on Metal Organic Frameworks,” spring meeting of The American Chemical Society, New Orleans, LA April 6 – 10, 2008.

22. M.D. Allendorf “Metal Organic Frameworks: Novel Nanoporous Materials for Sensing Applications,” invited seminar, Dept. of Electrical Engineering and Computer Science, University of California, Berkeley, April 18, 2008.